Analysis of the Interface Properties of Multi-Material 3D Printed Structures

Shauvik Pahari

A THESIS SUBMITTED TO THE FACULTY OF GRADUATE STUDIES IN PARTIAL FULFILLMENT OF THE REQUIREMENTS FOR THE DEGREE OF MASTER OF APPLIED SCIENCE

DEPARTMENT OF MECHANICAL ENGINEERING

LASSONDE SCHOOL OF ENGINEERING

YORK UNIVERSITY

TORONTO, ONTARIO, CANADA

August 2024

Abstract

Multi-material 3D printed (MM3DP) samples offer enhanced mechanical performance with the added benefit of being customizable for specific applications. However, MM3DP structures have weak adhesion at the boundary interface. So, the interface characteristics in those structures are a critical factor in determining the strength of the structures and predicting failure. Digital image correlation (DIC) is a full-field strain measurement technique ideal for evaluating the non-uniform load response in anisotropic materials due to their heterogeneous composition. This thesis demonstrates the fabrication of MM3DP samples using two distinctly different printing methods. The multi-material samples were extensively compared with the homogenous samples of the same base material with a shear test to assess their mechanical performance. Strain variations on the samples were analyzed and post-processed with DIC software as different material combinations were explored. Additionally, statistical analysis was performed to validate the results and assess the feasibility of the methodology.

Acknowledgements

I would like to express my deepest gratitude to my supervisor, Dr. Garrett Melenka, for providing me the opportunity to conduct research in his group and for his unwavering support throughout my master's program. His guidance, mentorship, and encouragement have been instrumental in my academic and personal growth. I am particularly grateful for his patience, understanding, and willingness to always go the extra mile to help me succeed. I am also grateful for his support in allowing me to pursue an internship and collaborate with professionals to expand my skills. I would also like to thank Dr, Reza Rizvi for his invaluable suggestions and feedback throughout my research journey.

I extend my heartfelt thanks to my past and present lab mates – Aya, Menna, Ali, Calvin, Thomas, Ayshan, Abhinav, Alex, Tristan, Gurnek, and Trung. Their friendship, collaboration, and support have created a positive and inclusive research environment. I am especially grateful for their willingness to share their knowledge and expertise. It has been an absolute pleasure working alongside such talented and supportive colleagues. Their camaraderie and friendship have made my time in the lab both productive and enjoyable. I will cherish the memories that we have made together. I would also like to thank my colleagues in my department at York University, particularly Sara, Angela, Behrad and Usman, for their support and encouragement. I am grateful to my colleagues at the University of Freiburg for their support and guidance during my internship. Their expertise and mentorship have significantly contributed to my learning and professional development.

I would like to express my sincere gratitude to Yvonne Yim, our graduate program coordinator, for her exceptional support and assistance throughout my time at York University. Her dedication,

professionalism, and always helpful demeanor have made a significant difference in my academic journey. I am also grateful to the lab technicians and other program coordinators for their constant support in ensuring a productive research environment.

Finally, I would like to thank my parents for their unwavering love, support, and encouragement throughout my academic journey. Their belief in me has been a constant source of motivation and inspiration.

Table of Contents

List of Figures

List of Tables

List of Abbreviations

ABS	Acrylonitrile Butadiene Styrene
AM	Additive Manufacturing
ANOVA	Analysis of Variance
ASTM	American Society for Testing and Materials
CAD	Computer-aided Design
CAGR	Compound Annual Growth
CCD	Charge-Coupled Device
CEA	Carboxyethyl Acrylate
CFRP	Carbon Fiber Reinforced Plastics
CMOS	Complementary Metal-Oxide Semiconductor
DIC	Digital Image Correlation
DLP	Digital Light Processing
DMAP	4-Dimethylaminopyridine
DMD	Digital Micromirror Device
DNA	Deoxyribonucleic Acid
DUDMA	Diurethane Dimethacrylate
FAA	Federal Aviation Administration
FDM	Fused Deposition Modeling
FFF	Fused Filament Fabrication
FRP	Fiber-reinforced Plastic
IA	Isobornyl Acrylate

ISO	International Organization for Standardization
ME	Material Extrusion
MJ	Material Jetting
MM	Multi-material
MMU	Multi-material Unit
MM3DP	Multi-material 3D Printing
NFL	National Football League
PBF	Powder Bed Fusion
PEG	Polyethylene Glycol
PEGDMA	Polyethylene Glycol Dimethacrylate
PET	Polyethylene Terephthalate
PETC	Polyethylene Terephthalate Glycol with carbon fibers
PETG	Polyethylene Terephthalate Glycol
PLA	Polylactic Acid
ROI	Region of Interest
SLA	Stereolithography
SLM	Selective Laser Melting
SOG	Sudan Orange G
TGA	Thermogravimetric Analysis
TPO	Thermoplastic Polyolefins
TPU	Thermoplastic Polyurethane
UV	Ultraviolet
VHD	Valvular Heart Disease

VPP	Vat Photopolymerization

Chapter 1 Introduction

1.1 Motivation

Additive manufacturing (AM), commonly known as 3D printing (3DP) is used to manufacture prototypes, models, or functional components from a three-dimensional Computer Aided Design (3D CAD) file. The 3D objects are produced by directly adding the materials layer-by-layer until the final structure is formed [1]. The main focus of this printing method was to produce prototypes or representative parts before a commercial part was produced since its invention in 1984 [2]. 3D printing enables parts to be produced with complex geometries, reduced time, minimal material wastage, and lower energy consumption, which were not achievable with conventional manufacturing techniques [3–6]. These advantages, along with the constant advancement in printer design and materials, have contributed to a market size of $ 4.56 billion in the U.S.[7]. 3DP has seen widespread applications in form and fit component, automobile, aerospace, material modelling, teaching aids, medical implants, prostheses, jewelry, and microdevices [8–21]. Surveys have shown the success of the adoption of this technology, as seen in Figure 1-1(b), where industrial 3D printers have the majority of the market share. Figure 1-1(a) illustrates the ten-year forecast of the additive manufacturing market size, estimated to grow at a Compound Annual Growth Rate (CAGR) of 20.51% to reach around USD 29.49 billion by 2033. North America currently holds the largest market share at 36.14%. The CAGR represents the average annual growth of the market size over this period.

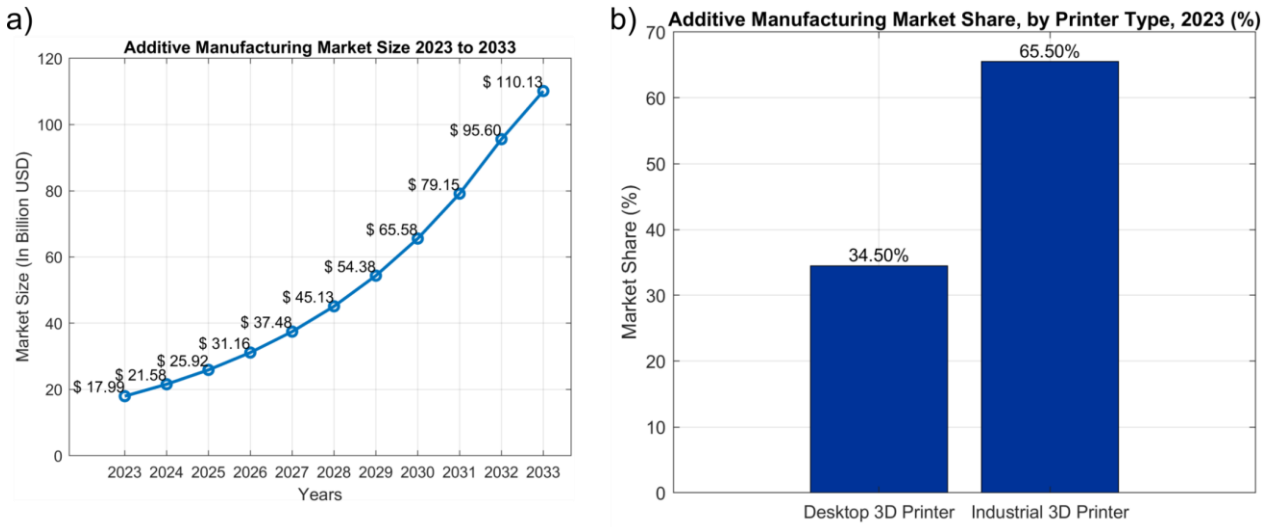

Figure 1-1: (a) Additive manufacturing market size forecast between 2023-2033; (b) Additive manufacturing market share between desktop 3D printers and industrial printers [7]**.**

Researchers are currently working on multi-material 3DP techniques to fabricate multi-material parts. A multi-material component is generally defined as a solid object composed of two or more materials distributed continuously or discontinuously randomly. Multi-material 3D printing (MM3DP) structures allow the design of complex geometries with tunable properties, resulting in parts with mechanical properties specifically tailored to the application. For example, the Eco Bracket by Diehl Aviation, composed of 3D-printed carbon fiber elements and thermoplastic composites, is 50% lighter and costs 50% less than traditional aluminum brackets [22].

The primary challenge with MM3DP is the weak adhesion among the heterogeneous polymers at the boundary interface. Studies have indicated that the interface formed between the heterogeneous materials at their geometrical boundary is considered a crucial element in multi-material 3D-printed components [23]. So, it is important to characterize the interface at the geometrical boundary of multi-material parts and evaluate the adhesion performance between the different materials.

Due to the complexity of the material composition in a multi-material structure, the materials experience heterogeneous deformation. Non-invasive methods like Digital Image Correlation (DIC) are ideal for evaluating such deformations. Samples are speckled before a load is applied. Cameras capture images at a high frame rate as the sample undergoes deformation, and the images are then correlated to track the speckles to extract the strain field. This technique has proved its efficacy in measuring non-uniform deformations in complex structures like composites [24–26]. Additionally, it can be compared to finite element analysis (FEA) and be used for model validations.

1.2 Thesis Objective

The main objective of this thesis is to analyze the interface characteristics of multi-material 3D printed structures and compare them with homogenous base material counterparts. Two different printing methods – Fused Filament Fabrication (FFF) and Digital Light Processing (DLP) were used in two studies to evaluate the adhesion characteristics of multi-material structures. Failure modes were observed after the samples failed to determine the quality of adhesion between the materials. The first requirement to achieve this objective is to analyze the axial and shear strain variations along the samples particularly at the boundary interface at the overlap region. Digital Image Correlation (DIC) was used to capture a large number of images as the samples were put under shear loading to evaluate the strains at different parts of the samples. Samples are speckled before loading into the universal testing machine. The DIC software then tracks these speckles, correlating all the images as the sample undergoes deformation. The results will provide detailed strain measurements, failure modes, and manufacturing consistency of the samples as different combinations of materials are explored.

1.3 Thesis Outline

The thesis consists of five chapters. Chapter 2 discusses the fundamental topics discussed in the thesis and provides a review of the previous studies related to multi-material 3D printed structures and Digital Image Correlation. The gaps in the literature have been summarized and discussed in this chapter which provides motivation for the next chapters.

Chapter 3 discusses the analysis of interface characteristics of FFF-printed multi-material structures. Shear and axial strains on single-lap joint samples of various material combinations, including homogenous and heterogeneous samples, were measured under a shear loading test using 2D DIC. The methodology demonstrated in the study showed the feasibility of FFF printing to fabricate multi-material structures with enhanced mechanical performance. The study described in Chapter 3 has been submitted to a peer-reviewed journal - "Composites Structures" under the title "*Analysis of interface properties of multi-material fused filament fabrication (FFF) printed polymer composite structures*" and is currently with the editor.

A different approach to multi-material 3D printing was explored with DLP printing. The methodology and results of this study are described in detail in Chapter 4. In this study, shear tests were performed on the DLP-printed single-lap joints to analyze shear strains and axial strains under loading conditions. 2D DIC was used to analyze the strain variations on the sample at different loads and to characterize the interface characteristics of the lap joint samples. The study shows promising results, highlighting the potential applications of this technology in the fabrication of soft robotics, microfluidic chips, and artificial tissues. It will be submitted to a peer review journal – "Additive Manufacturing," under the title of "*Analysis of the interface properties of multi-material digital light processing (DLP) printed polymer structures"*.

Chapter 5 summarizes all the results and findings from the two studies conducted in Chapters 3 and 4. It also provides some recommendations from the author to improve the methodology based on the experience and knowledge gained during the investigations. The final section also suggests some areas that could be explored in the future based on these studies.

1.4 References

[1] M.R. Khosravani, T. Reinicke, 3D-printed sensors: Current progress and future challenges, Sens. Actuator A Phys 305 (2020) 111916. https://doi.org/10.1016/j.sna.2020.111916.

[2] C.W. Hull, Apparatus for production of three dimensional objects by stereolithography., 1984.

[3] J. Jiang, X. Xu, J. Stringer, Optimization of process planning for reducing material waste in extrusion based additive manufacturing, ROBOT CIM-INT MANUF 59 (2019) 317–325. https://doi.org/10.1016/j.rcim.2019.05.007.

[4] M. Hisham, M. Shebeeb C, D. C, L. Jacob, H. Butt, Additive manufacturing of carbon nanocomposites for structural applications, J. Mater. Res. Technol 28 (2024) 4674–4693. https://doi.org/10.1016/j.jmrt.2024.01.049.

[5] M.R. Khosravani, T. Reinicke, On the environmental impacts of 3D printing technology, Appl. Mater. Today 20 (2020) 100689. https://doi.org/10.1016/j.apmt.2020.100689.

[6] D.G. Bekas, Y. Hou, Y. Liu, A. Panesar, 3D printing to enable multifunctionality in polymer-based composites: A review, Compos. B. Eng. 179 (2019) 107540. https://doi.org/10.1016/j.compositesb.2019.107540.

[7] Additive Manufacturing Market Size, Share, and Trends 2024 to 2033, Precedence Research, 2024. https://www.precedenceresearch.com/additive-manufacturing-market.

[8] E.C. Santos, M. Shiomi, K. Osakada, T. Laoui, Rapid manufacturing of metal components by laser forming, International Journal of Machine Tools and Manufacture 46 (2006) 1459–1468. https://doi.org/10.1016/j.ijmachtools.2005.09.005.

[9] S.S. Gill, M. Kaplas, Efficacy of powder-based three-dimensional printing (3DP) technologies for rapid casting of light alloys, Int J Adv Manuf Technol 52 (2011) 53–64. https://doi.org/10.1007/s00170-010-2716-1.

[10] S.H. Masood, W.Q. Song, Development of new metal/polymer materials for rapid tooling using Fused deposition modelling, Mater. Des 25 (2004) 587–594. https://doi.org/10.1016/j.matdes.2004.02.009.

[11] D.E. Cooper, M. Stanford, K.A. Kibble, G.J. Gibbons, Additive Manufacturing for product improvement at Red Bull Technology, Materials & Design 41 (2012) 226–230. https://doi.org/10.1016/j.matdes.2012.05.017.

[12] V.K. Vashishtha, R. Makade, N. Mehla, Advancement of rapid prototyping in aerospace industry -A review, International Journal of Engineering Science and Technology 3 (2011).

[13] A. Bandyopadhyay, B.V. Krishna, W. Xue, S. Bose, Application of Laser Engineered Net Shaping (LENS) to manufacture porous and functionally graded structures for load bearing implants, J Mater Sci: Mater Med 20 (2009) 29–34. https://doi.org/10.1007/s10856-008-3478-2.

[14] N. Oxman, E. Tsai, M. Firstenberg, Digital anisotropy: A variable elasticity rapid prototyping platform, Virtual Phys Prototyp 7 (2012) 261–274. https://doi.org/10.1080/17452759.2012.731369.

[15] P.K. Jain, P.M. Pandey, P.V.M. Rao, Tailoring material properties in layered manufacturing, Mater. Des 31 (2010) 3490–3498. https://doi.org/10.1016/j.matdes.2010.02.029.

[16] F.E. Wiria, J.Y.M. Shyan, P.N. Lim, F.G.C. Wen, J.F. Yeo, T. Cao, Printing of Titanium implant prototype, Mater. Des 31 (2010) S101–S105. https://doi.org/10.1016/j.matdes.2009.12.050.

[17] W. Wang, X. Shang, Functionally gradient material laser rapid prototyping technique, Tinshhua Sci. Technol. 14 (2009) 192–199. https://doi.org/10.1016/S1007-0214(09)70091-4.

[18] L.S. Bertol, W.K. Júnior, F.P.D. Silva, C. Aumund-Kopp, Medical design: Direct metal laser sintering of Ti–6Al–4V, Mater. Des 31 (2010) 3982–3988. https://doi.org/10.1016/j.matdes.2010.02.050.

[19] L. Ciocca, R. Scotti, CAD-CAM generated ear cast by means of a laser scanner and rapid prototyping machine, J Prosthet Dent 92 (2004) 591–595. https://doi.org/10.1016/j.prosdent.2004.08.021.

[20] S.H. Choi, H.H. Cheung, W.K. Zhu, A multi-material virtual prototyping system for biomedical applications, in: 2009 IEEE International Conference on Virtual Environments, Human-Computer Interfaces and Measurements Systems, IEEE, Hong Kong, China, 2009: pp. 73–78. https://doi.org/10.1109/VECIMS.2009.5068869.

[21] A. Bonyár, H. Sántha, B. Ring, M. Varga, J. Gábor Kovács, G. Harsányi, 3D Rapid Prototyping Technology (RPT) as a powerful tool in microfluidic development, Procedia Eng 5 (2010) 291–294. https://doi.org/10.1016/j.proeng.2010.09.105.

[22] P. Keane, 3D Printed Eco Bracket Lightens Aircraft and Lowers Costs, 3D Printing (2024). https://3dprinting.com/news/3d-printed-eco-bracket-lightens-aircraft-and-lowers-costs/ (accessed July 25, 2024).

[23] D. Espalin, J. Alberto Ramirez, F. Medina, R. Wicker, Multi-material, multi-technology FDM: exploring build process variations:, Rapid Prototyping Journal 20 (2014) 236–244. https://doi.org/10.1108/RPJ-12-2012-0112.

[24] J. Qiu, M.K. Idris, G. Grau, G.W. Melenka, Fabrication of electroluminescent carbon fiber composite for damage visualization, Manuf. Lett 24 (2020) 56–60. https://doi.org/10.1016/j.mfglet.2020.03.010.

[25] A. Goyal, G.W. Melenka, Investigation of carbon-aramid hybrid braided composites using digital volume correlation, Compos. Struct 321 (2023) 117207. https://doi.org/10.1016/j.compstruct.2023.117207.

[26] C. Unlusoy, G.W. Melenka, Flexural testing of cellulose fiber braided composites using three dimensional digital image correlation, Compos. Struct 230 (2019) 111538. https://doi.org/10.1016/j.compstruct.2019.111538.

Chapter 2 Literature Review

2.1 Introduction

The objective of this thesis is to analyze the characteristics of multi-material 3D-printed (MM3DP) single-lap joints using digital image correlation (DIC). This chapter discusses the fundamental topics relevant to this thesis and reviews a number of key literature sources in this area. Subsequent sections introduce 3D printing, analysis of adhesive strength, and digital image correlation. The chapter concludes by identifying the literature gaps and demonstrating how this study addresses those gaps.

3D printing is considered a transformative technology with the potential to disrupt the manufacturing industry by replacing traditional processes. It offers several advantages over conventional manufacturing processes, including the ability to produce complex geometries with minimal material wastage and energy consumption, all at a lower cost. The first section of this chapter introduces 3D printing and the advancements that have led to the development of multi-material 3D printed structures. It also covers the various methods for manufacturing multi-material structures and their applications.

The next section introduces an analysis of adhesion strength between materials and explores the different methods generally used. It also discusses an extensive review of various literatures on analyzing adhesion strength.

The next section introduces DIC. The fundamental principles of DIC and the different image-processing techniques have been discussed extensively. Following a comprehensive review of

various literature, the highlights and benefits of DIC are discussed, emphasizing its superiority over traditional strain measurement techniques.

2.2 3D Printing

2.2.1 Fundamentals of 3D Printing

Additive manufacturing, commonly known as 3D printing, started in the early 1980s with the advent of stereolithography, a technique that used a laser to selectively cure photopolymers [1]. In 1992, Stratasys introduced another manufacturing technique called fused deposition modelling (FDM) [2]. A thermoplastic filament is heated to its melting temperature and extruded through a nozzle to deposit on a surface and subsequently on the different horizontal layers as predefined in a digital model. Later, as 3D printing technology advanced, other techniques were developed. 3D printing offers numerous advantages, including the ability to produce complex geometries, reduce costs and lead times, enable greater customization, and minimize material wastage [3]. These benefits have led to its adoption in various manufacturing sectors, such as aerospace [4–6], robotics [7–9], automotive [10], energy [11,12], food [13–15], medical [16–19], and chemical industries [20–22]. Research and studies by academia and industries have significantly expanded the material pool for 3D printing. It is now possible to directly fabricate parts from metals [23–26], ceramics [27–30], glass [31–33], and polymers [34–37]. This process has been very useful in producing prototypes and has been very popular with both industries and hobbyists.

Standards from International Organization for Standardization (ISO) and the American Society for Testing and Materials (ASTM) have classified the different 3D printing processes into seven categories: binder jetting, directed energy deposition, material jetting, powder bed fusion, sheet

lamination, material extrusion, and vat photopolymerization [38]. A summary of all the various 3D printing methods has been provided in Table 2-1.

Table 2-1: Summary of different 3d printing methods

Methods	**Commercial models**	**Material**	**Benefits**	**Drawbacks**	**Resolution**	**Popular brands for printers**
Binder jetting	*3DP: 3D printing *ExOne	Metals: Stainless steel Polymers: ABS, PA Ceramics: Glass	*Faster *No melting	*Low mechanical properties *Post processing required	13-16 µm	HP, Markforged, Desktop Metal
Direct energy deposition	*LENS: Laser engineered net shaping *SDL: Selective Deposition Lamination	Metals: Cobalt, Nickel, Titanium	*No support structures *Enabling modification of grain structure	*High initial investment	250 µm	Optomec, DMG Mori, AddUp

Material Jetting	*NPJ: Nano-particle jetting *DOD-Drop-on demand	Polypropylene, HDPE< PS, PMMA	*High accuracy *Multi-material printing	*Post processing required *Proprietary materials	5-200 µm	Stratasys, 3D Systems, DP Polar
Powder bed fusion	*DMLS: Direct metal laser sintering *SLM: Selective laser melting *SLS: Selective laser sintering	*SHS: Nylon DMLS. *SLM: Stainless steel, titanium, aluminum *SLS: Nylon, PEEK	*Wide material range *Minimal support structures required	*Weak structural properties *Long print time	80-250 µm	Stratasys, Prima Additive
Sheet lamination	*LOM: Laminated object manufacture *SDL: Selective	Paper, plastic, and sheet metals	*Inexpensive *Relatively fast	*Limited material use *Post processing	0.1 mm	BCN3D Technologies

	deposition lamination			may be required		
Material extrusion	*FFF: Fused Filament Fabrication *FDM: Fused Deposition Modelling	*Polymers: ABS, PLA, PETG, TPU, PC	*Inexpensive *Ease of use	*Nozzle design issue *Less accurate	50-200 µm	Prusa Research, Bambu Lab, Creality, Stratasys
Vat photo-polymerization	*SLA: Stereolithography *DLP: Digital Light Processing	*Photopolymers	*Good finish *Relatively fast	*Expensive *Post processing required	10 µm	Prusa Research, Elegoo, Formlabs

2.2.2 Multi-Material 3D Printing

Traditional 3D printing methods are limited in the production of prototypes due to lower mechanical performance than conventional manufactured parts. So, efforts have been made to fabricate functional materials using this technology. The materials should be able to be specified and designed in specific locations to successfully fabricate functional materials. Recent developments in 3d printing have allowed functional materials to be fabricated using multiple materials in one object with customized performance characteristics. This has enabled the tailoring of the properties of the components, such as thermal, mechanical, and optical properties [39,40].

Several industries, such as aerospace, automotive, biomedical, and electronics [41], have already integrated multi-material 3D printing as they look forward to Industry 4.0 and focus on lean manufacturing. For example, NASA reduced the number of manufacturing steps for a fuel injector from 163 to just 2 by using 3D printing [42].

Studies have investigated different 3D printing techniques, such as material extrusion, material jetting, direct ink writing, vat photopolymerization, and direct energy deposition to produce MM3DP parts. The next section introduces those different techniques and their potential application areas.

2.2.2.1 Different Processes for Multi-Material Additive Manufacturing

2.2.2.1.1 Material Extrusion

Material extrusion (ME) is one of the most commonly used 3D printing techniques that extrude a material feedstock through a single nozzle or multiple nozzles, enabling the fabrication of an object with multiple materials [43]. It is capable of printing with a wide range of materials, including thermoplastics [44], metal-filled thermoplastics, composites [45], flexible elastomers [46], and blended multi-material powder-based feedstock [47,48]. The feedstock is melted inside the extruder and deposited onto a build plate layer-by-layer, as illustrated in Figure 2-1. Single hot-end printers use a modifier like the multi-material unit (MMU) in Prusa printers (Prusa Research, Czech Republic) to switch the filaments in the middle of the print. Printers with multiple hot ends, which are relatively expensive, preload filament into their extruders that then extrude the different filaments independently on the print bed. For successful functional prints, the different feedstock materials used in multi-material (MM) printing must have good adhesion properties.

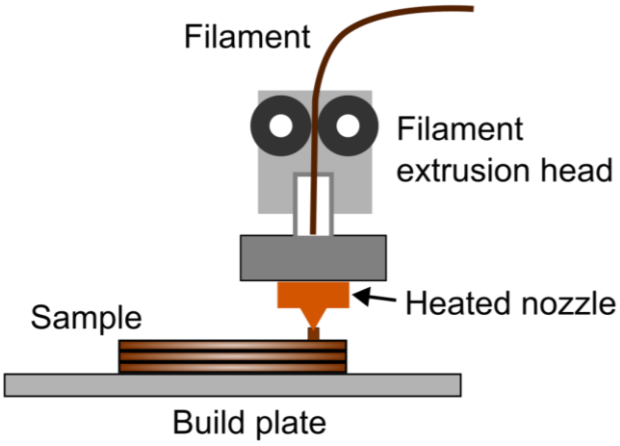

Figure 2-1: Schematic representation of FFF printing

Yin et al. [46] demonstrated the significance of optimum processing parameters for an adequate interfacial bonding between thermoplastic polyurethane (TPU) and acrylonitrile butadiene styrene (ABS) bi-material structures. The theoretical model was in good agreement with the experimental results and predicted the interfacial bonding strength based on thermally driven diffusion of multi-material filaments.

Ribeiro et al. [49] compared different interface mechanisms with homogenous PLA and heterogeneous PLA-TPU dovetail shape samples. One set of samples was designed for microscopic interfaces with a U-shape interface, while the other was designed for a macroscopic interface with a mechanical interlocking mechanism. Even though better mechanical performance was observed in samples with macroscopic interface designs, the interface adhesion was weak. The heterogeneous samples were significantly weaker than the homogenous samples as the multi-material samples delaminated at the interface.

Lopes et al. [50] compared three different samples: single material sample with a single extruder, single material sample with a dual extruder in a zebra crossing structure, and a multi-material

sample with two materials in a zebra crossing pattern with dual extruder. PLA, TPU and PET filaments were used as feedstock material. The results demonstrate the weak zones at the geometrical boundary interface in the multi-material samples due to a lack of chemical affinity. Hence, the multi-material samples were weaker than the single-material samples.

2.2.2.1.2 Powder Bed Fusion

In powder bed fusion (PBF), a layer of metal powder is spread on a substrate with a powder feeding system such as a rolling blade, selectively melting or sintering the area according to the computer-aided design (CAD) files. PBF printers use a laser (L-PBF) or electron beam (E-PBF) as a heat source [23]. The process is repeated for subsequent layers as the later layers are sintered or melted with the previous layers [43] as shown in Figure 2-2.

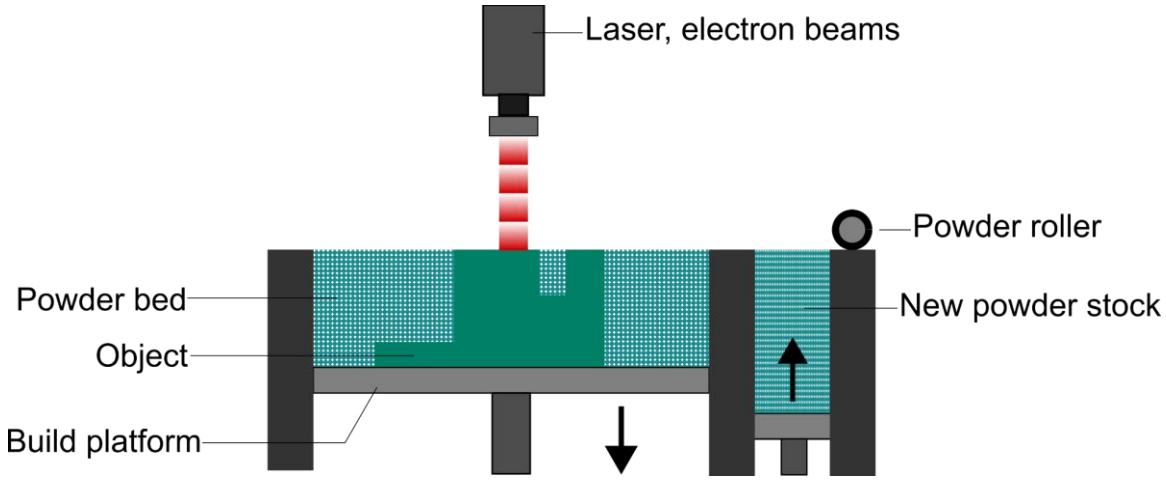

Figure 2-2: Schematic representation of PBF printing

The single powder delivery system limits the use of PBF printers for MM structures. Hence, multi-material samples with PBF are achieved by blending materials in different combinations [51,52].

Wei et al. [53] analyzed the characteristics and mechanical performance of Ti-5Al-2.5Sn/Ti-6Al-4V dual alloy material by SLM. The dog-bone specimens have a defect-free metallurgical bonded interface with almost similar microhardness at the two regions.

Chueh et al. [54] integrated FFF and PBF to analyze the bonding between metal and polymer parts. The study exhibited good adhesion between the metal and polymer with varying low-energy density lasers. 3D-printed mobile phone back cases and implants for controllable drug delivery systems were also successfully printed in this study with PBF to highlight the potential applications of heterogeneous metal/polymer structures.

The studies demonstrate the importance of optimizing process parameters, which allow the previous layers to be remelted and form proper bonds between each layer. Wu et al. [55] exhibited cracks between the different materials due to the varying thermal properties. Studies have shown that using smaller powder sizes with high melting points improves the mechanical performance of multi-material samples [56,57]. This is because the increased surface area results in greater energy absorption.

2.2.2.1.3 Material Jetting

Material jetting (MJ) deposits microdroplets on the build platform layer by layer and is then cured by UV light, as illustrated in Figure 2-3. Due to the nature of the technique, the number of materials that can be used in this process is very limited, as materials need to be viscous enough to form droplets. For the fabrication of multi-material samples, several tiny nozzles are fitted into the print head to print multiple photo-curable materials simultaneously with a high-resolution [58,59].

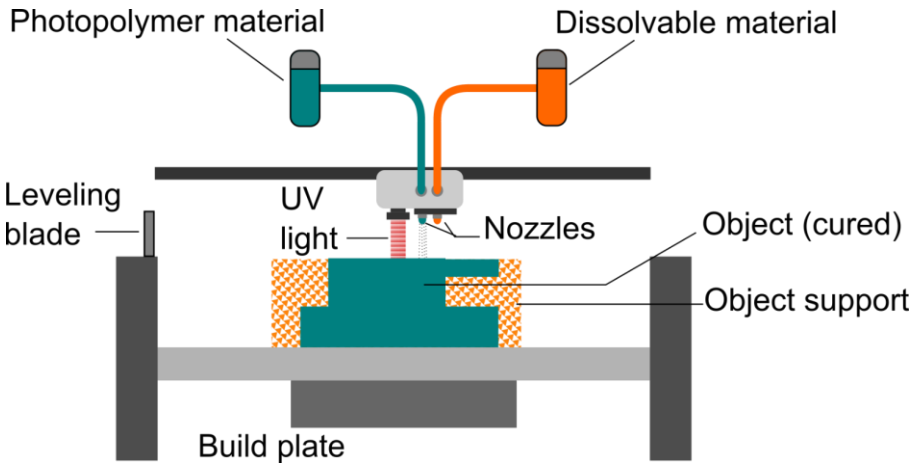

Figure 2-3: Schematic representation of material jetting

Vu et al. [59] used this process to fabricate multi-material fracture specimens with elastomer (TangoBlackPlus) and glassy acrylic (VeroWhitePlus) materials. Fractures were mainly observed at the material interface region. The study also demonstrated that the joint interface can be improved with gradient material interface.

2.2.2.1.4 Vat Photopolymerization

In vat photopolymerization (VPP), UV light is projected on a photopolymer resin, forming cross-links in the polymeric chain to transform the liquid resin into a solid. Figure 2-4 illustrates the working principle of VPP. This process produces parts with high accuracy and surface finish [60].

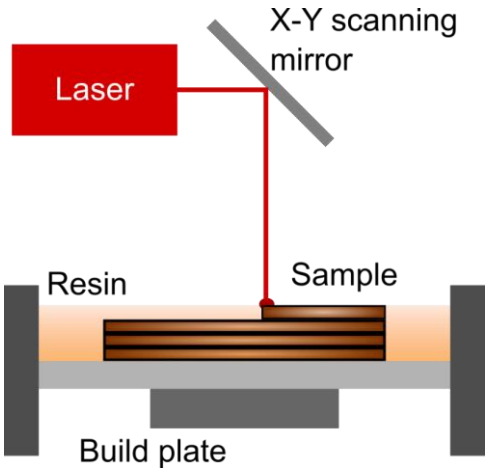

Figure 2-4: Schematic representation of VPP printing

Generally, multiple vats with different resins are used to fabricate MM parts with this process [60,61]. Hwangbo et al. [61] compared the mechanical properties of four different pairs of multi-materials with varying acrylate compositions on one part of the samples. Low functional acrylate with low viscosity exhibited better adhesion at the interface.

VPP has also been used to fabricate micro actuators with two different materials with distinct Young's moduli [60]. Two different vats were used during the fabrication, as they were switched out in the middle of the printing process to enable multi-material prints. Strong interface bonding was observed in the multi-material samples, as the yield strength was higher than that of the soft material. The methodology was also validated by printing a balloon with a self-sealing rigid inlet.

The primary challenge is the longer printing process required, as the vats need to be changed during MM printing.

2.2.2.2 Summary

MM 3D printing has enabled the fabrication of multi-material structures with improved mechanical performance, but it also presents challenges. Studies have been conducted using different processes and methods, primarily where different materials were assigned at various

layers. Analysis shows that most of the multi-material samples exhibited weak adhesion at the interface of the other materials. The adhesion strength can be improved by selecting the proper material combination and a suitable design process. So, further investigations are required to explore better material combinations and characterize the interface at the geometrical boundary of the multi-materials.

2.3 Selection of AM methods for the thesis

Material extrusion and vat photopolymerization are two of the most widely used methods in AM. FFF from ME and DLP from VPP were selected for the two distinct studies in this thesis. These AM methods are fundamentally different and offer unique advantages, as discussed in the previous section.

In FFF, the material is melted and deposited layer by layer, with layers adhering through thermally induced diffusion bonding [62]. In contrast, DLP involves polymerizing liquid resins under UV light, forming cross-links between each layer, resulting in strong chemical bonds. These differences highlight the distinct approaches each method takes in achieving layer adhesion.

The resolution of these two AM methods [43] indicates that the layers can be modified at the macroscopic level for FFF, whereas DLP has the ability to alter the microstructure of each layer. However, studies have shown that both these processes exhibited weak adhesion at the interfacial layer for multi-material prints, as discussed in the previous section.

Therefore, exploring different material combinations for FFF and DLP is crucial for improving the mechanical performance of multi-material prints. Additionally, investigating the interface characteristics of the boundary layers in these multi-material prints is important to understand and

enhance the adhesion between materials, leading to more robust and reliable multi-material components.

2.4 Analysis of Adhesion Strength

Two materials are combined using adhesive joints. These ensure a uniform load distribution, reduced stress concentrations, lighter parts, and lower cost than rivet or welded joints [63]. Various standards from ASTM and ISO are available, which provide a standardized method to analyze the adhesion at the joint [64,65].

ASTM D5868 is one such standard that demonstrates a standard test method for lap shear adhesion for fiber reinforced plastic (FRP) bonding [64]. Two fiber-reinforced parts of 25.4 mm by 101.6 mm with a thickness of 2.5 mm are joined together with an overlap area of 645 mm sq. with a suitable adhesive. Five samples must be prepared at least for the test and cooled at room temperature for a minimum of one hour after applying the adhesive. They are then tested in a universal testing machine (UTM) with an initial grip separation of 75 mm and at least 25.4 mm of the sample held in the test grips. The loading rate is specified to be 13 mm/min.

Hiremath et al. [66] analyzed the effect of printing orientation on the mechanical and shear characteristics of PLA specimens produced using FDM. Shear test was conducted based on ASTM D5868 to evaluate the shear strength of the samples. The 3D-printed single-lap joints with 0° print orientation had the highest shear strength than the samples with other print orientations.

Impregnating different fiber fabrics in the adhesive improved the strength of adhesively bonded single-lap joints [67]. Shear tests on the different single-lap joints showed that the presence of bidirectional carbon fibers in the adhesive exhibited the best performance.

Adhesively bonded Tin-GE single-lap joints were analyzed under different loading rates to evaluate the adhesion between the multi-materials [68]. Lap shear strength exhibited the same trend as the toughness and maximum load as the loading rate was increased. Though both cohesive and adhesive behavior was observed at meagre loading rates, adhesive failure was observed as loading rates increased.

The studies mentioned above highlight the importance of shear tests on single-lap joints in determining the adhesion characteristics at joint interfaces. Different failure modes in adhesively bonded samples, as illustrated in Figure 2-5, can also be characterized by ASTM standard [69]. The standard for classifying failure modes in FRP joints classifies the failure modes into the following categories:

- Adhesive failure – separation of the joint at the adhesive-adherend surface.
- Cohesive failure – separation of the joint within the adhesive
- Thin-layer cohesive failure – separation of the joints very close to the adhesive substrate interface.
- Fiber-tear failure – rupture within the FRP matrix.
- Light-fiber tear failure – rupture within the FRP matrix close to the interface, with a thin layer of FRP matrix on the adhesive.
- Stock break failure – rupture of the FRP matrix outside the adhesive joint region.
- Mixed failure – any combination of two or more failures mentioned above.

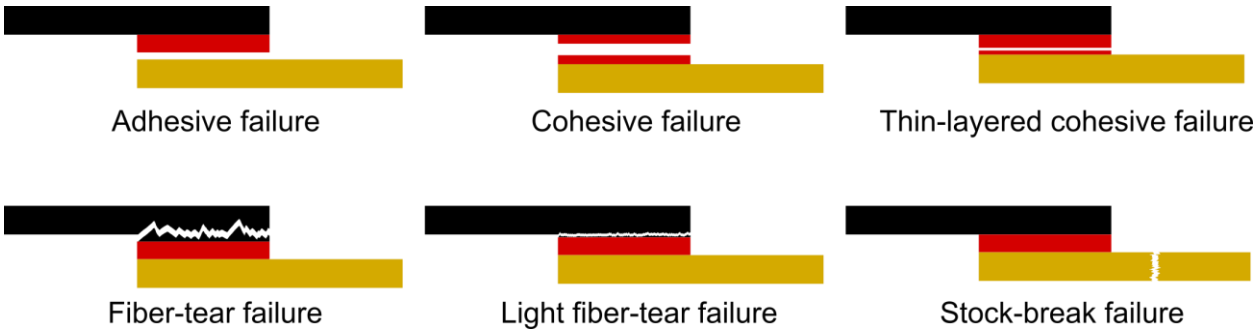

Figure 2-5: Different failure modes according to ASTM D5573

An adhesive failure indicates poor adhesive strength, whereas a stock break failure indicates a good adhesion between the materials.

2.5 Analysis of fiber content in 3D printing filaments

3D printed parts have been reinforced with different fibers in recent studies to improve the mechanical properties of these parts [70–72]. Various reinforcement materials have been incorporated in 3D printing filaments, such as polymer fibrils [73], carbon nanotubes [74], glass fibers [75], and carbon black [76]. Some of the studies have introduced these different fibers in the thermoplastic filament to fabricate parts with better recyclability, increased mechanical performance, and reduced cost [77].

Impregnating 13 % by weight carbon fibers in ABS filament increased the tensile strength of dog bone samples by 200% and modulus by 400% [78]. In the study, ABS pellets were compounded with chopped carbon fibers in a high shear mixer to produce the reinforced filament. Samples were fabricated with continuous carbon fiber winding, demonstrating parts with comparable mechanical performance but lighter and more inexpensive than conventional parts.

Zhong et al. [75] mixed ABS with short glass fibers with a twin extruder to achieve higher strength and hardness than conventional ABS. Samples fabricated with the blended reinforced ABS

exhibited higher tensile strength. The blended filaments also produced good 3D printed parts with the addition of small amounts of plasticizer and compatibilizer.

Tekinalp et al. [79] demonstrated a significant increase in tensile strength and modulus in ABS/carbon fiber FFF samples. A maximum of 115 % increase in tensile strength and 700 % increase in modulus was achieved with 40 % fiber content. Researchers have been unable to fabricate 3D-printed parts with more than 40 % fiber content in the filament as the nozzles would become clogged [35].

As the different fiber content in the filament significantly influences the mechanical properties of the samples, it is essential to determine the fiber content of the FRPs. The fiber content in FRPs is generally evaluated through thermogravimetric analysis (TGA) [80], acid digestion [81], and burn-off [82]. Recent studies have suggested that TGA is a more economical, automated, and accurate method to determine the fiber content in FRPs [83–86].

Moon et al. [80] compared TGA results with standard digestion and ignition loss methods to determine fiber content in carbon fiber-reinforced polymer (CFRP) and glass fiber-reinforced polymers (GFRP). The TGA results were within 1% consistency and in agreement with the standard ignition and digestion methods.

Reliability of TGA technique has also been investigated for graphite/epoxy composites [86]. The measurements of fiber weight percent were consistent within 1% and agreed with the measurements from matrix digestion. The study also highlights the sensitivity of the results to errors in the composite density.

2.6 Optical Measurement Techniques

Heterogeneous or multi-material samples undergo non-uniform deformation under loading conditions. Optical measurement techniques are well-suited to measuring this type of deformation in complex structures such as composites and multi-material 3D-printed structures. The following section discusses digital image correlation (DIC), which is one of the popular optical measurement techniques.

2.6.1 Digital Image Correlation (DIC)

Point-wise strain gauge technique is a prevalent technique for measuring deformation but has limitations [87,88]. The technique is not ideal for materials sensitive to very low stresses or with complex geometries as it is in direct contact with the testing samples. These challenges can be overcome by using non-invasive, full-field optical techniques. Various full-field optical techniques, such as speckle interferometry, moiré interferometry, holography interferometry, grid method, and digital image correlation, have been used in studies to measure deformation in a wide range of materials. DIC is a non-interferometric optical technique that has been widely accepted and used in the measurement of surface deformation [88]. It evaluates full-field displacements and strains by correlating digital images of a speckled sample surface from the initial undeformed stage to the deformed stage. It is an easier technique compared to the other interferometric techniques.

DIC setup consists of a charge-couple device camera (CCD) or a complementary metal-oxide semiconductor camera (CMOS), a computer with a storage device to record the images, and a speckled sample. The speckling pattern on the samples should be random and have sufficient contrast to achieve good DIC results [89]. Often, white or black paint is sprayed with a spray can or airbrush to achieve white or black speckled dots on the samples [88,90]. External light sources,

such as blue light [91], UV light [92] or white light [93], may be required to sufficiently illuminate the samples before recording images.

The captured images are segmented into evenly spaced subset windows, the size of which depends on the speckling density. Subsets are numerically correlated to each successive image from the reference image with the undeformed sample. The pattern in each subset window is approximated using an algorithmic interpolant function. The function then deforms from the reference image based on a subset shape function [89]. This provides the vector direction of the deformations and the strain on the sample. Figure 2-6 illustrates a shear strain distribution on a speckled sample after DIC processing.

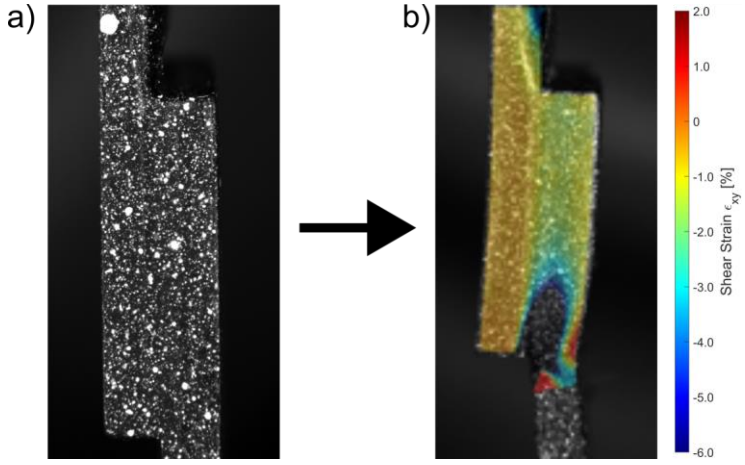

Figure 2-6: Representative images of a speckled sample with strain map. (a) Image of a speckled sample captured with a CCD camera; (b)Shear strain on the sample before failure after DIC processing

DIC measurement can be divided into four different steps – (a) speckling the samples, (b) image calibration, (c) capturing of images during deformation, and (d) post-processing captured images to evaluate various properties [88]. A calibration target with predetermined spacings or a scale can

be used as the reference image for calibration to convert from pixels to physical units (inches, mm).

2.6.2 Two-Dimensional Digital Image Correlation

DIC was initially designed to evaluate only planar deformations on materials [94]. Studies have improved and validated the accuracy of this technique in later years [95,96]. Two-dimensional (2D) DIC generally uses a single camera to capture images as the sample is deformed. Figure 2-7 illustrates an example of a 2D DIC setup.

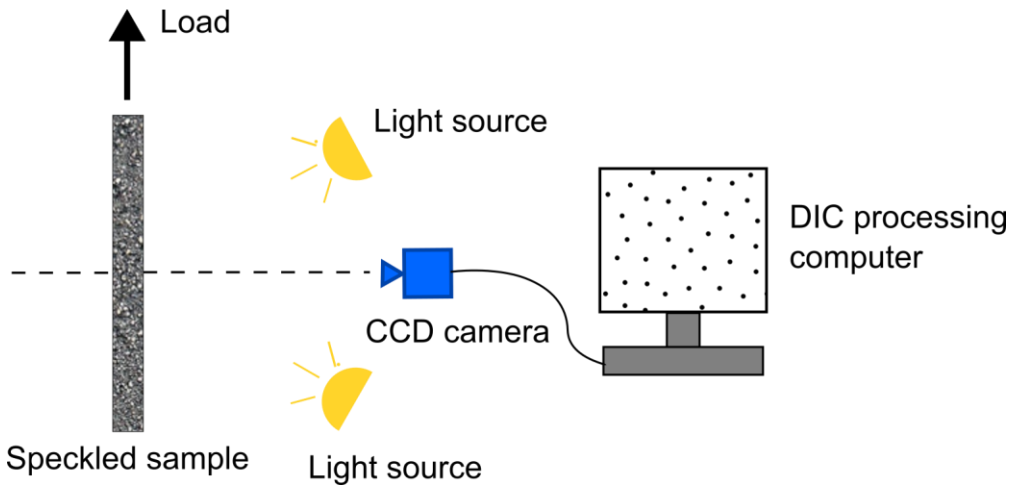

Figure 2-7: Schematic representation of a DIC setup

The limitation of 2D DIC is that it can evaluate only in-plane deformations and cannot determine out-of-plane deformations. 2D DIC can also be integrated with optical microscopy [97–99], laser scanning confocal microscope [100,101], scanning electron microscopy (SEM) [102–104], atomic force microscopy (AFM) [105–107], and scanning tunnelling microscope (STM) [108–110] to measure microscale and nanoscale deformation.

2D DIC was conducted to determine the mechanical behavior of bonded and hybrid bonded-bolted (HBB) under quasi-static tensile loading [111]. The study highlighted the advantages of 2D DIC

over conventional methods, like using a strain gauge to measure deformations. The tensile strain and shear strain distributions were shown in detail to evaluate the strain-concentrated regions, especially the region near the hole in the middle of the bonded joint.

2.6.3 Three-Dimensional Digital Image Correlation

2D DIC setup was modified by adding extra cameras to enable three-dimensional (3D) DIC, which evaluated both in-plane and out-of-plane deformations. 3D DIC requires a minimum of two cameras at a stereo angle for cross-correlation of images and image correlation. In stereo-DIC, the correlation between the reference and the image of deformed samples is correlated with the images from the other camera.

Melenka et al. [93] implemented 3D DIC to evaluate the effect of braiding pattern and braid angle on the strain pattern for tensile and torsional loads. The braid surface height was also assessed with the help of 3D DIC with some post-processing. The results show non-uniform strain patterns due to the braid yarn undulations.

Dondish et al. [112] demonstrated 3D DIC with a single high-speed camera and four planar mirrors. They evaluated the performance of carbon fiber-reinforced polymer laminates in compression after impact with 3D DIC. The study validated the use of a single high-speed camera with setup modifications as feasible, which offers a significant cost reduction compared to having a pair of high-speed cameras.

2.7 Gaps in Literature

Recent studies have investigated the fabrication of multi-materials with 3D printing to improve the mechanical properties of the 3D-printed parts, which can be used as functional materials. The majority of the studies have used inkjet printing and material jetting to investigate the performance

of the multi-material parts [42,113]. Almost every paper has highlighted the importance of analyzing the interface characteristics in MM3DP structures, as weak adhesion would cause delamination at the interface [49,50]. Very limited studies have utilized FFF or DLP printing to fabricate multi-material structures, though these are the most popular methods for conventional 3D printing. Material combinations have to be explored to find suitable combinations that adhere well to each other. These studies have exhibited weaker multi-material parts than its homogenous base material 3D printed samples. Researchers have used filaments impregnated with fibres to improve the mechanical performance of FFF 3D-printed parts [75,77], but no literature has been found on having different reinforced filaments to fabricate an FFF multi-material sample.

Though studies have investigated 3D-printed parts with DIC, no studies were found that utilized DIC to analyze the interface characteristics of FFF and DLP 3D-printed multi-material parts. DIC has been proven very effective for materials with non-uniform deformations, so it is ideal for analyzing the deformations in multi-material 3D-printed samples where the material properties may differ significantly. It tracks the deformation of the samples to generate the strain maps at different loads on the sample, which evaluates localized strains. Potential weak areas on the samples could also be assessed from the strain propagation. More data could be extracted using DIC to analyze the interface characteristics in greater detail for the MM3DP structures.

The literature review concludes that there is much to explore in MM3DP, from selecting the proper combination of materials to the printing process. The lack of data in specific areas highlights the need for an in-depth analysis of interface characteristics in MM3DP structures. This requires a proper printing process with optimum printing parameters.

2.8 Proposed Study

The author suggests that the studies on the analysis of interface characteristics in MM3DP structures demonstrated in the following two chapters address the gaps in the literature. The first study evaluates the interface characteristics of FFF-printed single-lap joints using 2D DIC. Two thermoplastic filaments and a fiber-reinforced filament were used to make different homogenous and multi-material samples. The strength of the multi-material samples was compared to homogenous samples with mechanical testing, and then the results were also compared statistically. DLP-printed single-lap joints were used for the second study, and similar mechanical testing was performed using DIC. Samples fabricated in this study had significantly different properties than the FFF-printed samples. Statistical analysis was also performed on the samples to identify the statistical difference between the samples.

2.9 References

[1] S.S. Crump, Apparatus and method for creating three dimensional objects, 5121329, 1992.

[2] C.W. Hull, Apparatus for production of three-dimensional objects by stereolithography, 4575330, 1986.

[3] J. Li, C. Wu, P.K. Chu, M. Gelinsky, 3D printing of hydrogels: Rational design strategies and emerging biomedical applications, Mater. Sci. Eng. R Rep. 140 (2020) 100543. https://doi.org/10.1016/j.mser.2020.100543.

[4] L.E. Murr, Frontiers of 3D Printing/Additive Manufacturing: from Human Organs to Aircraft Fabrication†, J Mater Sci Technol 32 (2016) 987–995. https://doi.org/10.1016/j.jmst.2016.08.011.

[5] L. Nickels, AM and aerospace: an ideal combination, Metal Powder Report 70 (2015) 300–303. https://doi.org/10.1016/j.mprp.2015.06.005.

[6] S.C. Joshi, A.A. Sheikh, 3D printing in aerospace and its long-term sustainability, Virtual Phys Prototyp 10 (2015) 175–185. https://doi.org/10.1080/17452759.2015.1111519.

[7] M.M. Stanton, C. Trichet-Paredes, S. Sánchez, Applications of three-dimensional (3D) printing for microswimmers and bio-hybrid robotics, Lab Chip 15 (2015) 1634–1637. https://doi.org/10.1039/C5LC90019K.

[8] N.W. Bartlett, M.T. Tolley, J.T.B. Overvelde, J.C. Weaver, B. Mosadegh, K. Bertoldi, G.M. Whitesides, R.J. Wood, A 3D-printed, functionally graded soft robot powered by combustion, Science 349 (2015) 161–165. https://doi.org/10.1126/science.aab0129.

[9] J.Z. Gul, M. Sajid, M.M. Rehman, G.U. Siddiqui, I. Shah, K.-H. Kim, J.-W. Lee, K.H. Choi, 3D printing for soft robotics – a review, Science and Technology of Advanced Materials 19 (2018) 243–262. https://doi.org/10.1080/14686996.2018.1431862.

[10] D.E. Cooper, M. Stanford, K.A. Kibble, G.J. Gibbons, Additive Manufacturing for product improvement at Red Bull Technology, Mater. Des 41 (2012) 226–230. https://doi.org/10.1016/j.matdes.2012.05.017.

[11] F. Zhang, M. Wei, V.V. Viswanathan, B. Swart, Y. Shao, G. Wu, C. Zhou, 3D printing technologies for electrochemical energy storage, Nano Energy 40 (2017) 418–431. https://doi.org/10.1016/j.nanoen.2017.08.037.

[12] A. Ambrosi, M. Pumera, 3D-printing technologies for electrochemical applications, Chem. Soc. Rev. 45 (2016) 2740–2755. https://doi.org/10.1039/C5CS00714C.

[13] F.C. Godoi, S. Prakash, B.R. Bhandari, 3d printing technologies applied for food design: Status and prospects, J Food Eng 179 (2016) 44–54. https://doi.org/10.1016/j.jfoodeng.2016.01.025.

[14] J. Sun, Z. Peng, W. Zhou, J.Y.H. Fuh, G.S. Hong, A. Chiu, A Review on 3D Printing for Customized Food Fabrication, Procedia Manuf 1 (2015) 308–319. https://doi.org/10.1016/j.promfg.2015.09.057.

[15] J. Sun, W. Zhou, D. Huang, J.Y.H. Fuh, G.S. Hong, An Overview of 3D Printing Technologies for Food Fabrication, Food Bioprocess Technol 8 (2015) 1605–1615. https://doi.org/10.1007/s11947-015-1528-6.

[16] M.J. Lerman, J. Lembong, G. Gillen, J.P. Fisher, 3D printing in cell culture systems and medical applications, Appl. Phys. Rev 5 (2018) 041109. https://doi.org/10.1063/1.5046087.

[17] S. Bose, S. Vahabzadeh, A. Bandyopadhyay, Bone tissue engineering using 3D printing, Mater. Today 16 (2013) 496–504. https://doi.org/10.1016/j.mattod.2013.11.017.

[18] M.S. Sulkin, E. Widder, C. Shao, K.M. Holzem, C. Gloschat, S.R. Gutbrod, I.R. Efimov, Three-dimensional printing physiology laboratory technology, Am. J. Physiol. Heart Circ. Physiol 305 (2013) H1569–H1573. https://doi.org/10.1152/ajpheart.00599.2013.

[19] N.A. Sears, D.R. Seshadri, P.S. Dhavalikar, E. Cosgriff-Hernandez, A Review of Three-Dimensional Printing in Tissue Engineering, Tissue Eng Part B Rev 22 (2016) 298–310. https://doi.org/10.1089/ten.teb.2015.0464.

[20] K.I. Galkin, V.P. Ananikov, Alkynes as a versatile platform for construction of chemical molecular complexity and realization of molecular 3D printing, Russ. Chem. Rev. 85 (2016) 226–247. https://doi.org/10.1070/RCR4611.

[21] B. Gross, S.Y. Lockwood, D.M. Spence, Recent Advances in Analytical Chemistry by 3D Printing, Anal. Chem. 89 (2017) 57–70. https://doi.org/10.1021/acs.analchem.6b04344.

[22] R.D. Johnson, Chemical creativity with 3D printing, Nature Chem 4 (2012) 338–339. https://doi.org/10.1038/nchem.1333.

[23] T. DebRoy, H.L. Wei, J.S. Zuback, T. Mukherjee, J.W. Elmer, J.O. Milewski, A.M. Beese, A. Wilson-Heid, A. De, W. Zhang, Additive manufacturing of metallic components – Process, structure and properties, Prog. Mater. Sci 92 (2018) 112–224. https://doi.org/10.1016/j.pmatsci.2017.10.001.

[24] D.D. Gu, W. Meiners, K. Wissenbach, R. Poprawe, Laser additive manufacturing of metallic components: materials, processes and mechanisms, International Materials Reviews 57 (2012) 133–164. https://doi.org/10.1179/1743280411Y.0000000014.

[25] W.E. Frazier, Metal Additive Manufacturing: A Review, J. of Materi Eng and Perform 23 (2014) 1917–1928. https://doi.org/10.1007/s11665-014-0958-z.

[26] D. Herzog, V. Seyda, E. Wycisk, C. Emmelmann, Additive manufacturing of metals, Acta Materialia 117 (2016) 371–392. https://doi.org/10.1016/j.actamat.2016.07.019.

[27] J.W. Halloran, Ceramic Stereolithography: Additive Manufacturing for Ceramics by Photopolymerization, Annu. Rev. Mater. Res. 46 (2016) 19–40. https://doi.org/10.1146/annurev-matsci-070115-031841.

[28] J.A. Lewis, Direct-write assembly of ceramics from colloidal inks, Curr Opin Solid State Mater Sci 6 (2002) 245–250. https://doi.org/10.1016/S1359-0286(02)00031-1.

[29] C. Minas, D. Carnelli, E. Tervoort, A.R. Studart, 3D Printing of Emulsions and Foams into Hierarchical Porous Ceramics, Adv. Mater 28 (2016) 9993–9999. https://doi.org/10.1002/adma.201603390.

[30] Z.C. Eckel, C. Zhou, J.H. Martin, A.J. Jacobsen, W.B. Carter, T.A. Schaedler, Additive manufacturing of polymer-derived ceramics, Science 351 (2016) 58–62. https://doi.org/10.1126/science.aad2688.

[31] F. Kotz, P. Risch, K. Arnold, S. Sevim, J. Puigmartí-Luis, A. Quick, M. Thiel, A. Hrynevich, P.D. Dalton, D. Helmer, B.E. Rapp, Fabrication of arbitrary three-dimensional suspended hollow microstructures in transparent fused silica glass, Nat Commun 10 (2019) 1439. https://doi.org/10.1038/s41467-019-09497-z.

[32] F. Kotz, K. Arnold, W. Bauer, D. Schild, N. Keller, K. Sachsenheimer, T.M. Nargang, C. Richter, D. Helmer, B.E. Rapp, Three-dimensional printing of transparent fused silica glass, Nature 544 (2017) 337–339. https://doi.org/10.1038/nature22061.

[33] G. Marchelli, R. Prabhakar, D. Storti, M. Ganter, The guide to glass 3D printing: developments, methods, diagnostics and results, Rapid Prototyp J 17 (2011) 187–194. https://doi.org/10.1108/13552541111124761.

[34] S.C. Ligon, R. Liska, J. Stampfl, M. Gurr, R. Mülhaupt, Polymers for 3D Printing and Customized Additive Manufacturing, Chem. Rev. 117 (2017) 10212–10290. https://doi.org/10.1021/acs.chemrev.7b00074.

[35] X. Wang, M. Jiang, Z. Zhou, J. Gou, D. Hui, 3D printing of polymer matrix composites: A review and prospective, Compos. B. Eng 110 (2017) 442–458. https://doi.org/10.1016/j.compositesb.2016.11.034.

[36] J.W. Stansbury, M.J. Idacavage, 3D printing with polymers: Challenges among expanding options and opportunities, Dent Mater 32 (2016) 54–64. https://doi.org/10.1016/j.dental.2015.09.018.

[37] B. Wendel, D. Rietzel, F. Kühnlein, R. Feulner, G. Hülder, E. Schmachtenberg, Additive Processing of Polymers, Macro Materials & Eng 293 (2008) 799–809. https://doi.org/10.1002/mame.200800121.

[38] ISO/ASTM 52915:2020, Specification for additive manufacturing file format (AMF) Version 1.2, (2020). https://www.iso.org/standard/74640.html (accessed July 30, 2024).

[39] X. Zheng, C. Williams, C.M. Spadaccini, K. Shea, Perspectives on multi-material additive manufacturing, J. Mater. Res 36 (2021) 3549–3557. https://doi.org/10.1557/s43578-021-00388-y.

[40] C. Yuan, F. Wang, B. Qi, Z. Ding, D.W. Rosen, Q. Ge, 3D printing of multi-material composites with tunable shape memory behavior, Mater. Des 193 (2020) 108785. https://doi.org/10.1016/j.matdes.2020.108785.

[41] A. Nazir, O. Gokcekaya, K. Md Masum Billah, O. Ertugrul, J. Jiang, J. Sun, S. Hussain, Multi-material additive manufacturing: A systematic review of design, properties, applications, challenges, and 3D printing of materials and cellular metamaterials, Mater. Des 226 (2023) 111661. https://doi.org/10.1016/j.matdes.2023.111661.

[42] D.J. Roach, C.M. Hamel, C.K. Dunn, M.V. Johnson, X. Kuang, H.J. Qi, The m4 3D printer: A multi-material multi-method additive manufacturing platform for future 3D printed structures, Addit Manuf 29 (2019) 100819. https://doi.org/10.1016/j.addma.2019.100819.

[43] A.S.K. Kiran, J.B. Veluru, S. Merum, A.V. Radhamani, M. Doble, T.S.S. Kumar, S. Ramakrishna, Additive manufacturing technologies: an overview of challenges and perspective of using electrospraying, Nanocomposites 4 (2018) 190–214. https://doi.org/10.1080/20550324.2018.1558499.

[44] S. Wickramasinghe, C. Peng, R. Ladani, P. Tran, Analysing fracture properties of bio-inspired 3D printed suture structures, THIN WALL STRUCT 176 (2022) 109317. https://doi.org/10.1016/j.tws.2022.109317.

[45] A. Gupta, S. Hasanov, I. Fidan, Z. Zhang, Homogenized modeling approach for effective property prediction of 3D-printed short fibers reinforced polymer matrix composite material, Int J Adv Manuf Technol 118 (2022) 4161–4178. https://doi.org/10.1007/s00170-021-08230-9.

[46] J. Yin, C. Lu, J. Fu, Y. Huang, Y. Zheng, Interfacial bonding during multi-material fused deposition modeling (FDM) process due to inter-molecular diffusion, Mater. Des 150 (2018) 104–112. https://doi.org/10.1016/j.matdes.2018.04.029.

[47] D. Ke, A.A. Vu, A. Bandyopadhyay, S. Bose, Compositionally graded doped hydroxyapatite coating on titanium using laser and plasma spray deposition for bone implants, Acta Biomaterialia 84 (2019) 414–423. https://doi.org/10.1016/j.actbio.2018.11.041.

[48] S. Hasanov, A. Gupta, A. Nasirov, I. Fidan, Mechanical characterization of functionally graded materials produced by the fused filament fabrication process, J Manuf Process 58 (2020) 923–935. https://doi.org/10.1016/j.jmapro.2020.09.011.

[49] M. Ribeiro, O. Sousa Carneiro, A. Ferreira Da Silva, Interface geometries in 3D multi-material prints by fused filament fabrication, Rapid Prototyp J 25 (2019) 38–46. https://doi.org/10.1108/RPJ-05-2017-0107.

[50] L.R. Lopes, A.F. Silva, O.S. Carneiro, Multi-material 3D printing: The relevance of materials affinity on the boundary interface performance, Addit Manuf 23 (2018) 45–52. https://doi.org/10.1016/j.addma.2018.06.027.

[51] C. Wei, Z. Zhang, D. Cheng, Z. Sun, M. Zhu, L. Li, An overview of laser-based multiple metallic material additive manufacturing: from macro- to micro-scales, Int. J. Extrem. Manuf. 3 (2021) 012003. https://doi.org/10.1088/2631-7990/abce04.

[52] N.E. Putra, M.J. Mirzaali, I. Apachitei, J. Zhou, A.A. Zadpoor, Multi-material additive manufacturing technologies for Ti-, Mg-, and Fe-based biomaterials for bone substitution, Acta Biomaterialia 109 (2020) 1–20. https://doi.org/10.1016/j.actbio.2020.03.037.

[53] K. Wei, X. Zeng, F. Li, M. Liu, J. Deng, Microstructure and Mechanical Property of Ti-5Al-2.5Sn/Ti-6Al-4V Dissimilar Titanium Alloys Integrally Fabricated by Selective Laser Melting, JOM 72 (2020) 1031–1038. https://doi.org/10.1007/s11837-019-03988-6.

[54] Y.-H. Chueh, C. Wei, X. Zhang, L. Li, Integrated laser-based powder bed fusion and fused filament fabrication for three-dimensional printing of hybrid metal/polymer objects, Addit Manuf 31 (2020) 100928. https://doi.org/10.1016/j.addma.2019.100928.

[55] B. Wu, Z. Pan, D. Ding, D. Cuiuri, H. Li, J. Xu, J. Norrish, A review of the wire arc additive manufacturing of metals: properties, defects and quality improvement, J Manuf Process 35 (2018) 127–139. https://doi.org/10.1016/j.jmapro.2018.08.001.

[56] O. Gokcekaya, T. Ishimoto, T. Todo, P. Wang, T. Nakano, Influence of powder characteristics on densification via crystallographic texture formation: Pure tungsten prepared by laser powder bed fusion, ADDIT MANUF LETT 1 (2021) 100016. https://doi.org/10.1016/j.addlet.2021.100016.

[57] J.A. Glerum, S. Hocine, C.S.T. Chang, C. Kenel, S. Van Petegem, N. Casati, D.F. Sanchez, H. Van Swygenhoven, D.C. Dunand, Operando X-ray diffraction study of thermal and phase evolution during laser powder bed fusion of Al-Sc-Zr elemental powder blends, Addit Manuf 55 (2022) 102806. https://doi.org/10.1016/j.addma.2022.102806.

[58] Y.L. Yap, C. Wang, S.L. Sing, V. Dikshit, W.Y. Yeong, J. Wei, Material jetting additive manufacturing: An experimental study using designed metrological benchmarks, Precis Eng 50 (2017) 275–285. https://doi.org/10.1016/j.precisioneng.2017.05.015.

[59] I. Vu, L. Bass, N. Meisel, B. Orler, C.B. Williams, D.A. Dilliard, Characterization of mutli-material interfaces in polyjet additive manufacturing, in: Proceedings - 26th Annual International Solid Freeform Fabrication Symposium, Austin, n.d.: pp. 959–982. https://doi.org/Code 159684.

[60] Q. Song, Y. Chen, P. Hou, P. Zhu, D. Helmer, F. Kotz-Helmer, B.E. Rapp, Fabrication of Multi-Material Pneumatic Actuators and Microactuators Using Stereolithography, Micromachines 14 (2023) 244. https://doi.org/10.3390/mi14020244.

[61] H. Hwangbo, S.-J. Jeon, Digital light processing 3D printing of multi-materials with improved adhesion using resins containing low functional acrylates, Korean J. Chem. Eng. 39 (2022) 451–459. https://doi.org/10.1007/s11814-021-0934-x.

[62] C.-C. Shih, M. Burnette, D. Staack, J. Wang, B.L. Tai, Effects of cold plasma treatment on interlayer bonding strength in FFF process.pdf, Addit Manuf 25 (2019) 104–111. https://doi.org/10.1016/j.addma.2018.11.005.

[63] F.L. Ribeiro, L. Borges, J.R.M. d'Almeida, Numerical stress analysis of carbon-fibre-reinforced epoxy composite single-lap joints, Int J Adhes Adhes 31 (2011) 331–337. https://doi.org/10.1016/j.ijadhadh.2011.01.008.

[64] D5868, Standard Test Method for Lap Shear Adhesion for Fiber Reinforced Plastic (FRP) Bonding, (n.d.). https://www.astm.org/d5868-01r14.html (accessed July 30, 2024).

[65] ISO 21194:2019, Elastic adhesives — Testing of adhesively bonded joints — Bead peel test, (2019). https://www.iso.org/standard/70066.html (accessed July 30, 2024).

[66] V.S. Hiremath, T. Dhilipkumar, D. Mallikarjuna Reddy, S. Bagewadi, Effect of print orientation on tensile and shear properties of 3D printed lap joints, Mater. Today (2023) S2214785323037550. https://doi.org/10.1016/j.matpr.2023.06.362.

[67] A. Thirunavukarasu, R.S. Sikarwar, Enhancing the strength of adhesively bonded single-lap composite joints using fiber fabrics, Mater. Lett 357 (2024) 135664. https://doi.org/10.1016/j.matlet.2023.135664.

[68] B.N.V.S. Ganesh Gupta K, M.M. Hiremath, B. Sen, R.K. Prusty, B.C. Ray, Influence of loading rate on adhesively bonded Tin-glass/epoxy single lap joint, Mater. Today 26 (2020) 1850–1854. https://doi.org/10.1016/j.matpr.2020.02.406.

[69] ASTM D5573-99, Practice for Classifying Failure Modes in Fiber-Reinforced-Plastic (FRP) Joints, (2019). https://doi.org/10.1520/D5573-99R19.

[70] X. Tian, T. Liu, C. Yang, Q. Wang, D. Li, Interface and performance of 3D printed continuous carbon fiber reinforced PLA composites, Compos. Part A Appl. Sci. Manuf 88 (2016) 198–205. https://doi.org/10.1016/j.compositesa.2016.05.032.

[71] K. Mori, T. Maeno, Y. Nakagawa, Dieless Forming of Carbon Fibre Reinforced Plastic Parts Using 3D Printer, Procedia Eng 81 (2014) 1595–1600. https://doi.org/10.1016/j.proeng.2014.10.196.

[72] A. Pilipović, P. Raos, M. Šercer, Experimental analysis of properties of materials for rapid prototyping, Int J Adv Manuf Technol 40 (2009) 105–115. https://doi.org/10.1007/s00170-007-1310-7.

[73] R.W. Gray IV, D.G. Baird, J.H. Bøhn, Thermoplastic composites reinforced with long fiber thermotropic liquid crystalline polymers for fused deposition modeling, Polym. Compos 19 (1998) 383–394. https://doi.org/10.1002/pc.10112.

[74] G.C. Pidcock, M. In Het Panhuis, Extrusion printing of flexible electrically conducting carbon nanotube networks, Adv. Funct. Mater 22 (2012) 4790–4800. https://doi.org/10.1002/adfm.201200724.

[75] W. Zhong, F. Li, Z. Zhang, L. Song, Z. Li, Short fiber reinforced composites for fused deposition modeling, Mater. Sci. Eng. A 301 (2001) 125–130. https://doi.org/10.1016/S0921-5093(00)01810-4.

[76] S.J. Leigh, R.J. Bradley, C.P. Purssell, D.R. Billson, D.A. Hutchins, A Simple, Low-Cost Conductive Composite Material for 3D Printing of Electronic Sensors, PLoS ONE 7 (2012) e49365. https://doi.org/10.1371/journal.pone.0049365.

[77] N. Li, Y. Li, S. Liu, Rapid prototyping of continuous carbon fiber reinforced polylactic acid composites by 3D printing, J. Mater. Process. Technol 238 (2016) 218–225. https://doi.org/10.1016/j.jmatprotec.2016.07.025.

[78] L.J. Love, V. Kunc, O. Rios, C.E. Duty, A.M. Elliott, B.K. Post, R.J. Smith, C.A. Blue, The importance of carbon fiber to polymer additive manufacturing, J. Mater. Res. 29 (2014) 1893–1898. https://doi.org/10.1557/jmr.2014.212.

[79] H.L. Tekinalp, V. Kunc, G.M. Velez-Garcia, C.E. Duty, L.J. Love, A.K. Naskar, C.A. Blue, S. Ozcan, Highly oriented carbon fiber–polymer composites via additive manufacturing, Compos Sci Technol 105 (2014) 144–150. https://doi.org/10.1016/j.compscitech.2014.10.009.

[80] C.-R. Moon, B.-R. Bang, W.-J. Choi, G.-H. Kang, S.-Y. Park, A technique for determining fiber content in FRP by thermogravimetric analyzer, Polym. Test 24 (2005) 376–380. https://doi.org/10.1016/j.polymertesting.2004.10.002.

[81] M.H. Hassan, A.R. Othman, S. Kamaruddin, Void Content Determination of Fiber Reinforced Polymers by Acid Digestion Method, Adv Mat Res 795 (2013) 64–68. https://doi.org/10.4028/www.scientific.net/AMR.795.64.

[82] C.N. Morales, G. Claure, J. Álvarez, A. Nanni, Evaluation of fiber content in GFRP bars using digital image processing, Compos. B. Eng. 200 (2020) 108307. https://doi.org/10.1016/j.compositesb.2020.108307.

[83] R. Meier, I. Kahraman, A.T. Seyhan, S. Zaremba, K. Drechsler, Evaluating vibration assisted vacuum infusion processing of hexagonal boron nitride sheet modified carbon fabric/epoxy composites in terms of interlaminar shear strength and void content, Compos Sci Technol 128 (2016) 94–103. https://doi.org/10.1016/j.compscitech.2016.03.022.

[84] X. Zhu, L. Yao, X. Yang, H. Sun, A. Guo, A. Li, H. Yang, Spatiotemporal expression of KHSRP modulates Schwann cells and neuronal differentiation after sciatic nerve injury, Int. J. Biochem. Cell Biol 48 (2014) 1–10. https://doi.org/10.1016/j.biocel.2013.12.008.

[85] K. Naito, H. Oguma, Tensile properties of novel carbon/glass hybrid thermoplastic composite rods, Compos. Struct 161 (2017) 23–31. https://doi.org/10.1016/j.compstruct.2016.11.042.

[86] R.Y. Yee, T.S. Stephens, A TGA technique for determining graphite fiber content in epoxy composites, Thermochim Acta (n.d.) 191–199. https://doi.org/10.1016/0040-6031(95)02606-1.

[87] C.C. Perry, Strain-Gage Reinforcement Effects on Orthotropic Materials, Exp. Tech 10 (1986) 20–24. https://doi.org/10.1111/j.1747-1567.1986.tb01386.x.

[88] B. Pan, K. Qian, H. Xie, A. Asundi, Two-dimensional digital image correlation for in-plane displacement and strain measurement: a review, Meas. Sci. Technol. 20 (2009) 062001. https://doi.org/10.1088/0957-0233/20/6/062001.

[89] E. Jones, M. Iadicola, R. Bigger, B. Blaysat, C. Boo, M. Grewer, J. Hu, A. Jones, M. Klein, K. Raghavan, P. Reu, T. Schmidt, T. Siebert, M. Simenson, D. Turner, A. Vieira, T. Weikert, A Good Practices Guide for Digital Image Correlation, 1st ed., International Digital Image Correlation Society, 2018. https://doi.org/10.32720/idics/gpg.ed1.

[90] H. Schreier, J.-J. Orteu, M.A. Sutton, Image Correlation for Shape, Motion and Deformation Measurements: Basic Concepts,Theory and Applications, Springer US, Boston, MA, 2009. https://doi.org/10.1007/978-0-387-78747-3.

[91] B.M.B. Grant, H.J. Stone, P.J. Withers, M. Preuss, High-temperature strain field measurement using digital image correlation, The Journal of Strain Analysis for Engineering Design 44 (2009) 263–271. https://doi.org/10.1243/03093247JSA478.

[92] Y. Dong, H. Kakisawa, Y. Kagawa, Optical system for microscopic observation and strain measurement at high temperature, Meas. Sci. Technol. 25 (2014) 025002. https://doi.org/10.1088/0957-0233/25/2/025002.

[93] G.W. Melenka, J.P. Carey, Experimental analysis of diamond and regular tubular braided composites using three-dimensional digital image correlation, J Compos Mater 51 (2017) 3887–3907. https://doi.org/10.1177/0021998317695418.

[94] W.H. Peters, W.F. Ranson, Digital Imaging Techniques In Experimental Stress Analysis, Opt. Eng 21 (1982). https://doi.org/10.1117/12.7972925.

[95] M. Sutton, C. Mingqi, W. Peters, Y. Chao, S. McNeill, Application of an optimized digital correlation method to planar deformation analysis, Image Vis Comput 4 (1986) 143–150. https://doi.org/10.1016/0262-8856(86)90057-0.

[96] H.A. Bruck, S.R. McNeill, M.A. Sutton, W.H. Peters, Digital image correlation using Newton-Raphson method of partial differential correction, Exp Mech 29 (1989) 261–267. https://doi.org/10.1007/BF02321405.

[97] Z. Sun, J.S. Lyons, S.R. McNeill, Measuring Microscopic Deformations with Digital Image Correlation, Opt Lasers Eng 27 (1997) 409–428. https://doi.org/10.1016/S0143-8166(96)00041-3.

[98] M. Pitter, C. See, J. Goh, M. Somekh, Focus errors and their correction in microscopic deformation analysis using correlation, Opt. Express 10 (2002) 1361. https://doi.org/10.1364/OE.10.001361.

[99] M. Luo, Displacement/strain measurements using an optical microscope and digital image correlation, Opt. Eng 45 (2006) 033605. https://doi.org/10.1117/1.2182108.

[100] T.A. Berfield, J.K. Patel, R.G. Shimmin, P.V. Braun, J. Lambros, N.R. Sottos, Fluorescent Image Correlation for Nanoscale Deformation Measurements, Small 2 (2006) 631–635. https://doi.org/10.1002/smll.200500289.

[101] C. Franck, S. Hong, S.A. Maskarinec, D.A. Tirrell, G. Ravichandran, Three-dimensional Full-field Measurements of Large Deformations in Soft Materials Using Confocal Microscopy and Digital Volume Correlation, Exp Mech 47 (2007) 427–438. https://doi.org/10.1007/s11340-007-9037-9.

[102] N. Sabaté, D. Vogel, A. Gollhardt, J. Keller, B. Michel, C. Cané, I. Gràcia, J.R. Morante, Measurement of residual stresses in micromachined structures in a microregion, Appl. Phys. Lett 88 (2006) 071910. https://doi.org/10.1063/1.2177357.

[103] J. Keller, A. Gollhardt, D. Vogel, E. Auerswald, N. Sabate, J. Auersperg, B. Michel, FibDAC - Residual Stress Determination by Combination of Focused Ion Beam Technique and Digital Image Correlation, MSF 524–525 (2006) 121–126. https://doi.org/10.4028/www.scientific.net/MSF.524-525.121.

[104] N. Sabaté, D. Vogel, A. Gollhardt, J. Marcos, I. Gràcia, C. Cané, B. Michel, Digital image correlation of nanoscale deformation fields for local stress measurement in thin films, Nanotechnology 17 (2006) 5264–5270. https://doi.org/10.1088/0957-4484/17/20/037.

[105] I. Chasiotis, W.G. Knauss, A New Microtensile Tester for the Study of MEMS Materials with the Aid of Atomic Force Microscopy, Exp Mech 42 (2002) 51–57. https://doi.org/10.1007/BF02411051.

[106] W.G. Knauss, I. Chasiotis, Y. Huang, Mechanical measurements at the micron and nanometer scales, Mech. Mater 35 (2003) 217–231. https://doi.org/10.1016/S0167-6636(02)00271-5.

[107] S. Cho, I. Chasiotis, T.A. Friedmann, J.P. Sullivan, Young's modulus, Poisson's ratio and failure properties of tetrahedral amorphous diamond-like carbon for MEMS devices, J. Micromech. Microeng. 15 (2005) 728–735. https://doi.org/10.1088/0960-1317/15/4/009.

[108] G. Vendroux, W.G. Knauss, Submicron deformation field measurements: Part 1. Developing a digital scanning tunneling microscope, Exp Mech 38 (1998) 18–23. https://doi.org/10.1007/BF02321262.

[109] G. Vendroux, W.G. Knauss, Submicron deformation field measurements: Part 2. Improved digital image correlation, Exp Mech 38 (1998) 86–92. https://doi.org/10.1007/BF02321649.

[110] G. Vendnroux, N. Schmidt, W.G. Knauss, Submicron deformation field measurements: Part 3. Demonstration of deformation determinations, Experimental Mechanics 38 (1998) 154–160. https://doi.org/10.1007/BF02325737.

[111] J. Kim, P. Lopez-Cruz, M. Heidari-Rarani, L. Lessard, J. Laliberté, An experimental study on the mechanical behaviour of bonded and hybrid bonded-bolted composite joints using digital image correlation (DIC) technique, Compos. Struct 276 (2021) 114544. https://doi.org/10.1016/j.compstruct.2021.114544.

[112] A. Dondish, L. Li, G.W. Melenka, Full-field deformation and failure analysis for compression after impact of carbon fibre reinforced polymer laminates, Compos. Struct 323 (2023) 117469. https://doi.org/10.1016/j.compstruct.2023.117469.

[113] J.P. Moore, C.B. Williams, Fatigue properties of parts printed by PolyJet material jetting, Rapid Prototyp J 21 (2015) 675–685. https://doi.org/10.1108/RPJ-03-2014-0031.

Chapter 3 Analysis of the interface properties of multi-material fused filament fabricated (FFF) printed polymer composite structures

3.1 Introduction

One of the key topics of the 21st century in the society is sustainability. Industrial activity accounts for 22% of total final energy consumption and for about 20% of global CO2 emissions [1]. According to the model calculations shown by Gebler et al., additive manufacturing, which is commonly known as 3D Printing, has the potential to reduce costs by $170-593 billion US, the total primary energy supply by 2.54-9.30 EJ, and CO2 emissions by 130.5-525.5 Mt by 2025 [2]. Additive manufacturing is a rapidly expanding sustainable technology that is used to manufacture components with limited wastage of material [3,4]. In this process, a specimen is fabricated layer-by-layer, facilitating the seamless production of complex geometries.

Fused filament fabrication (FFF) offers distinct advantages compared to other 3D printing methods, primarily affordability and accessibility. It accounts for approximately 60% of the global market share among all different types of 3D printers [5]. The availability of different types of filaments has significantly increased compared to previous years, helping users to utilize non-conventional materials. Until recently, studies have focused on single-material solutions, even after the advent of multi-material 3D printing technologies. One of the main

reasons for limited exploration of multi-material 3D printing is the high price of the multi-material printers [6].

Even though 3D printing has gained popularity in recent years, the mechanical properties of 3D printed parts are generally low compared to those of injection-molded parts [7–9], and hence, unusable for critical applications. This limits the potential of 3D printing to a prototyping technology. To address these issues, 3D printing of multi-material components has enabled manufacturing of 3D printed composite parts with enhanced functionality [10,11], reduced part components, and streamlined assembly. This technology enables to selectively design samples with multiple materials with varying mechanical properties, offering design freedom to manufacture parts with enhanced mechanical properties [12,13] and fracture resistance [14]. MM3DP structures have potential applications in critical sectors such as – biomedical, aerospace and electronics [15]. The challenge with 3D printing processes is the porosity and anisotropy associated with layer-by-layer printing process. This can lead to weak layer adhesion, which results in reduced strength [16].

Limited studies have been found on multi-material FFF printing, but studies are available on multi-material 3D printing based on material jetting process [17]. Rigid materials were combined with flexible materials to fabricate a DNA shoe from PENSAR through material jetting[18]. Many printers, especially independent dual extrusion (IDEX) printers and even printers with five independent extruders, like Prusa XL, are emerging in the current market to facilitate multi-material FFF printing. Despite all the progress, these studies [17,18] have concluded that the performance of the multi-material 3D printed structures depends highly on the adhesion at the interface of the multi-material structures. One of the challenges with

multi-material additive manufacturing is the weak strength of multi-material structures due to poor adhesive strength between different heterogeneous polymers [19]. This is not a concern in materials with multiple-colored filaments, but filaments composed of different materials due to their different polymeric properties. In multi-material inkjet printing [17,20], the authors have reported that the bonding at the interface of the multi-material structures was not as weak as the homogenous materials. Some studies [21,22] have been conducted to investigate the boundary interface of multi-material FFF printed structures, where the most used filaments like Polylactic Acid (PLA) and Thermoplastic Polyurethane (TPU) were used. Though both studies assess different interface mechanisms to evaluate the optimum design for better mechanical performance, the tensile modulus of the multi-material structures is lower than the homogenous specimens. The multi-material structures also show weak zones at the boundary interface and ruptures along it. The research indicates that characterizing the boundary interface of multi-material 3D printed structures is essential for fabricating multi-material parts with better performance. However, current studies lack sufficient data at macroscopic and microscopic levels to improve the mechanical properties.

There have been some studies on the reinforcement of 3D-printed parts in the past few years to enhance the mechanical properties of these parts [23–25]. The performance of Acrylonitrile Butadiene Styrene (ABS) specimens by Zhong et al. [26] showed a 22.5% increase in strength compared to pure ABS specimens when short glass fibres were introduced into ABS. In the work by Shofner et al. [27], ABS filaments with aligned vapor-grown nano-fibers improved the mechanical properties but decreased the ductility of ABS. It has been found that increasing the weight fraction of short fibers by more than 40% results

in a clogged nozzle [28], and hence the studies have limited the short carbon fiber quantity to 40%. The 3D-printed carbon fiber-reinforced thermoplastic structures offer several advantages over conventional thermoplastics, such as recyclability, low cost, and increased mechanical performance [29,30].

Thermogravimetric analysis (TGA) is used widely for fiber-reinforced polymers (FRPs) to measure the weight fraction of the fibers in the polymers [31,32]. Bücheler et al. [33] used TGA to determine the carbon fiber weight percentage of FRP and demonstrated that the absolute error with TGA was less than ±0.5 wt%. TGA was also performed by Kabir et al. to find the weight volume fractions in a commercial carbon fiber reinforced filament (Onyx) [34]. Studies have shown that TGA is a cost-effective, automated, and precise alternative method that can be used instead of other labour-intensive fiber volume fraction methods such as acid digestion, burn-off, and optical instrumentation [35–38].

The strain and failure characteristics need to be assessed at the boundary interface of the multi-material 3D-printed samples to evaluate the strength of the adhesion between the heterogeneous materials. Due to the complexity of the composition of the multi-material structures, non-destruction vision-based methods like digital image correlation (DIC) are ideal for measuring heterogeneous deformation. DIC is an optical full-field deformation measurement technique typically using one or two cameras for image acquisition. It tracks randomized speckles sprayed on the samples before mechanical testing through image acquisition and their correlation to extract the strain field. It has been proven to be a versatile tool and has become common to measure non-uniform deformations during mechanical

testing in complex structures like composites [39–41]. Recent studies have also found DIC to be effective for polymeric materials [42].

This study aims to analyze the adhesion of different materials at the boundary interface using single-lap joints. The samples will be subjected to shear loads in a universal testing machine to assess the strain field and mechanical properties. During testing, 2D DIC technique will be used to evaluate the samples. DIC has not been performed until now for multi-material FFF-printed parts. This would be the first time that DIC has been conducted on FFF-printed multi-material structures for an extensive evaluation of the interface properties of the multi-material structures. Images were taken at two angles simultaneously for both the front and side view to get an overall view of the strain maps along the samples as illustrated in Figure 3-3(b). Microscopic images of the cross-section were also taken to investigate the adhesion between the different polymers at the interface.

3.2 Materials and methods

3.2.1 Sample preparation

3.2.1.1 Printer and feed stock materials

The single lap joints, as shown in Figure 3-1(a) and (b), were designed using SolidWorks (Dassault Systèmes SolidWorks Corporation, Massachusetts, USA) for a standard test method for lap shear adhesion for fiber-reinforced plastic (FRP) bonding [43]. All the samples were fabricated using the open-source FFF 3D printer [Prusa MK3S (Firmware 3.11.0, Prusa Research, Prague, Czech Republic] with a 0.4 mm diameter hardened steel nozzle and 1.75 mm diameter feedstock inlet. Samples were printed with 100 % rectilinear

infill with a + 45°/ - 45° orientation in alternate layers. Multi Material Upgrade 2.0 (MMU2) (Prusa Research, Prague, Czech Republic) was also attached to the printer to allow the printer to print with five different filaments sequentially without physical intervention. The printer has only one extruder, but the MMU2 helps insert and pull out the filaments from the extruder automatically, according to the sliced program, without any physical intervention. The design of the MMU2 had a limitation where it did not support printing different materials if the materials had different printing temperatures. So, custom G-codes were added in the slicer software [Prusa Slicer (Version 2.5.0), Prusa Research, Prague, Czech Republic] to change the extruder temperature before the second filament is introduced in the extruder.

Three different types of commercially available filaments, as listed in Table 3-1, were obtained to manufacture the samples, as shown in Table 3-2. Five samples were fabricated for each material combination to investigate the repeatability and accuracy of the study. Polylactic Acid (PLA) was selected as it is the most extensively used material in extrusion-based 3D printing process [22,44]. Polyethylene Terephthalate Glycol (PETG) is one of the most common filaments used among the polyester family, offering greater strength, durability, and increased impact resistance. It is mainly used for packaging in retail and medical sectors, advertising displays, and electronic insulators [45]. Due to good shock and chemical resistance, this material is also prevalently used to make pressure-clad items, food containers, and protective parts. A PETG with short carbon fibers (PETC) filament was also obtained commercially after literature analysis, where it was found that the maximum allowable weight fraction of carbon fibers in a filament for FFF printing is 40 % [28]. The PETC used in this study was PETG infused with 20 % weight fraction of short carbon fibers.

The optimum printing parameters for the three different filaments after multiple iterations with different printing settings, are shown in Table 3-1. Other popular filaments like ABS and TPU have already exhibited poor adhesion at the interface of multi-material 3D printed samples in previous studies [21,22].

Table 3-1: Printing parameters for the different filaments

Filament	Manufacturer	First layer extruder temperature (℃)	Other layers extruder temperature (℃)	Printer bed temperature (℃)
PLA	Eryone, Guandong, China	215	205	60
PETG	Eryone, Guandong, China	235	230	90
PETC	iSANGHU, Guandong, China	235	230	90

Table 3-2: Sample ID for all the different material combinations.

Sample ID	Material combination
AA	PLA-PLA
BB	PETG-PETG
CC	PETC-PETC
AB	PLA-PETG
AC	PLA-PETC
BC	PETG-PETC

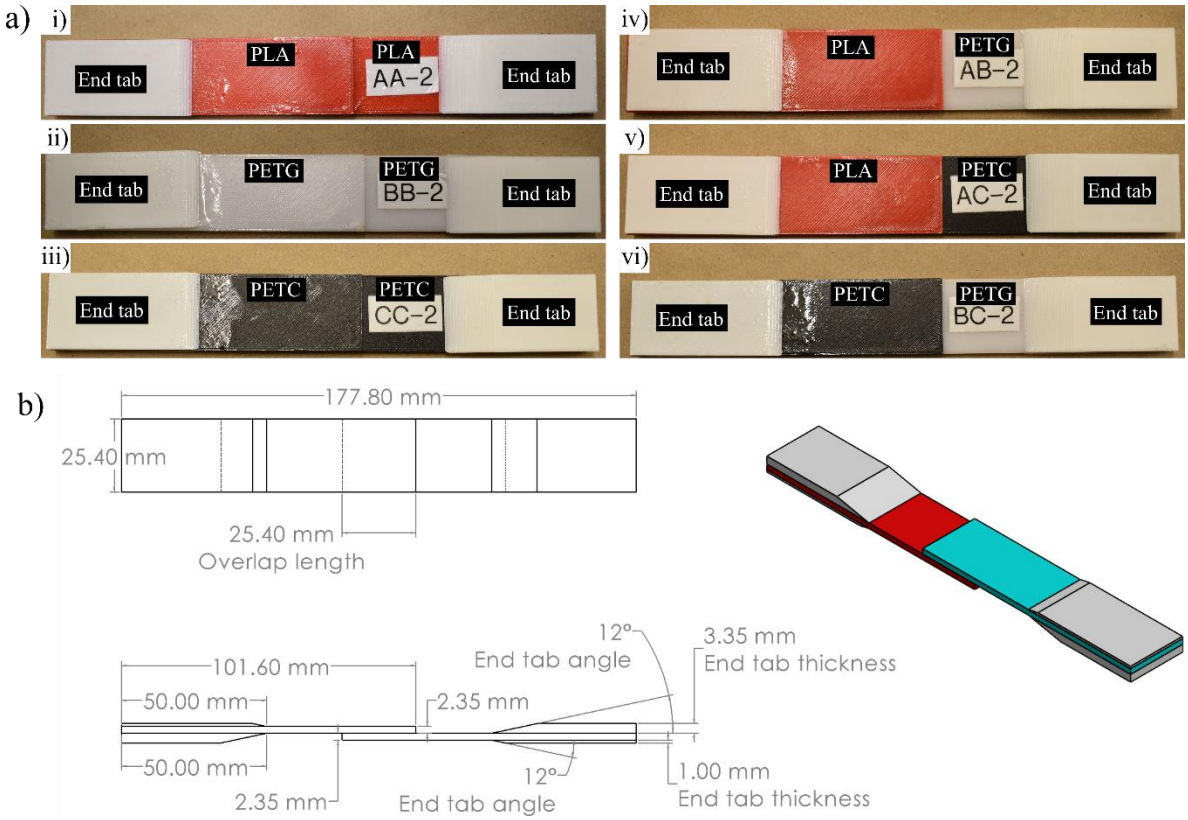

Figure 3-1: (a) Examples of 3D printed single lap joints with end tabs; (i) PLA-PLA, (ii) PETG-PETG, (iii) PETC-PETC, (iv) PLA-PETG, (v) PLA-PETC, and (vi) PETG-PETC; (b) Schematic representation of the 3D printed single lap joints.

3.2.1.2 Shear test

The single-lap joints were subjected to a shear load using an Instron ElectroPuls E3000 (Instron, Norwood, USA) equipped with a 3kN load cell. The samples were loaded at a constant crosshead speed of 5 mm/min. This differs from the standard as the crosshead speed given in the standard was significantly faster, causing the polymer samples to fail quickly and providing insufficient images for good DIC results. The samples were measured using 3732XFL-1 (1-inch) and 3732XFL-2 (2-inch) digital micrometers (Starrett, Athol, USA) at

five different points, and their average was taken for further calculations. The samples were also thinner than the standard due to limited space in the clamps in Instron.

3.2.1.3 Surface preparation and painting

The samples were then prepared to have high-contrast speckle patterns for DIC. A black paint coat was applied to the samples using a flat black paint (Painter's Touch Flat Black, Rust-Oleum Corp., Concord, ON). A mixture of white paint (5212 Opaque White, Createx Airbrush Colors, Createx Colors, East Granby CT) and reducer (4012 High Performance Reducer, Createx) was then applied to the sample with an airbrush (Paasche Airbrush H-3MH set, Paasche Airbrush Co, Chicago, IL) for a random white speckle pattern as shown in Figure 3-2. The histograms in the figure also show well-distributed multiple peaks and valleys, thereby minimizing the error percentage in DIC analysis [46].

3D-printed PLA end tabs were attached to the samples using a high-strength two-part epoxy (Gorilla Epoxy, Gorilla Glue Company, Cincinnati, OH). It allows the shear load to be applied evenly, reduces out-of-plane bending moments and, subsequently, high peel stresses and non-uniform shear stresses [47]. The tab taper angle was 12° as shown in Figure 3-1(b) to reduce the stress concentration at the tab terminals [48].

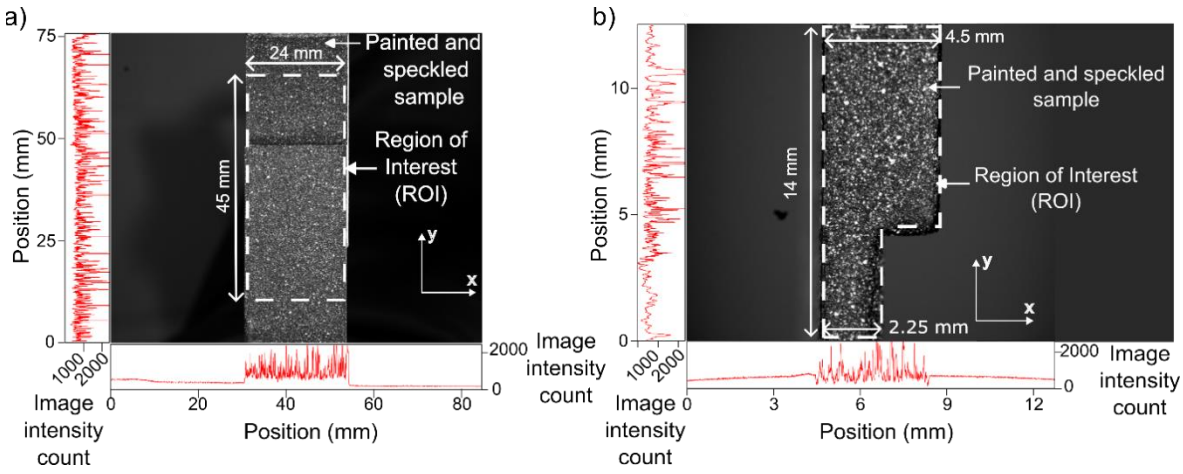

Figure 3-2: Images of the painted and speckled samples from DIC cameras with the ROI, horizontal, and vertical FOV shown. (a) Front view of the sample with 50 mm lens; (b) Lateral view of the sample with macro lens.

3.2.2 Material characterization

Thermogravimetric analysis was performed to determine fiber weight fraction in the PETC filaments. Thermogravimetric instrument TGA55 (TGA 0550-0497, TA Instruments Inc., USA) was used to heat three different samples of the PETC filament following the parameters specified in ASTM E1131- 08 [32]. The samples were heated from 25°C to 750°C at a heating rate of 10°C/min in Platinum HT pan under a dry nitrogen atmosphere at a flowrate of 20 mL/min. TRIOS software was used for data analysis.

3.2.3 Imaging setup

3.2.3.1 2D DIC Imaging Setup

Two high-resolution cameras (Imager M-lite 5M, LaVision GmbH, Göttingen, Germany) were placed at 90° to each other, as shown in Figure 3-3, to take images of both the front and side views of the sample simultaneously. Images were acquired at a rate of 20 frames per

second until failure. The camera and lens properties have been listed in Table 3-3. The camera for imaging the wider front view was equipped with a fixed focal length lens (MVL50M23 50 mm, Navitar, Rochester, USA), and the camera for imaging the narrower side view was equipped with a macro lens (3.3X macro zoom, Edmund Optics, Barrington, USA). Two LED panels (LED Lighting Panel, Adjustable Intensity, 500 Watt, Neewer) were installed beside the cameras to implement bright field illumination for a strong contrast between the white speckles and the black base coat. The cameras and lighting were mounted on different tripods.

Table 3-3: Properties of the imaging setup

Property	Unit	Value for setup for front view	Value for setup for side view
Camera resolution	px x px	2464 x 2056	2464 x 2056
Pixel size	µm	3.45	3.45
Frame rate	Hz	20	20
Image Scaling Factor	px/mm	27	167
Image field of view	mm x mm	91 x 76	14.5 x 12.5

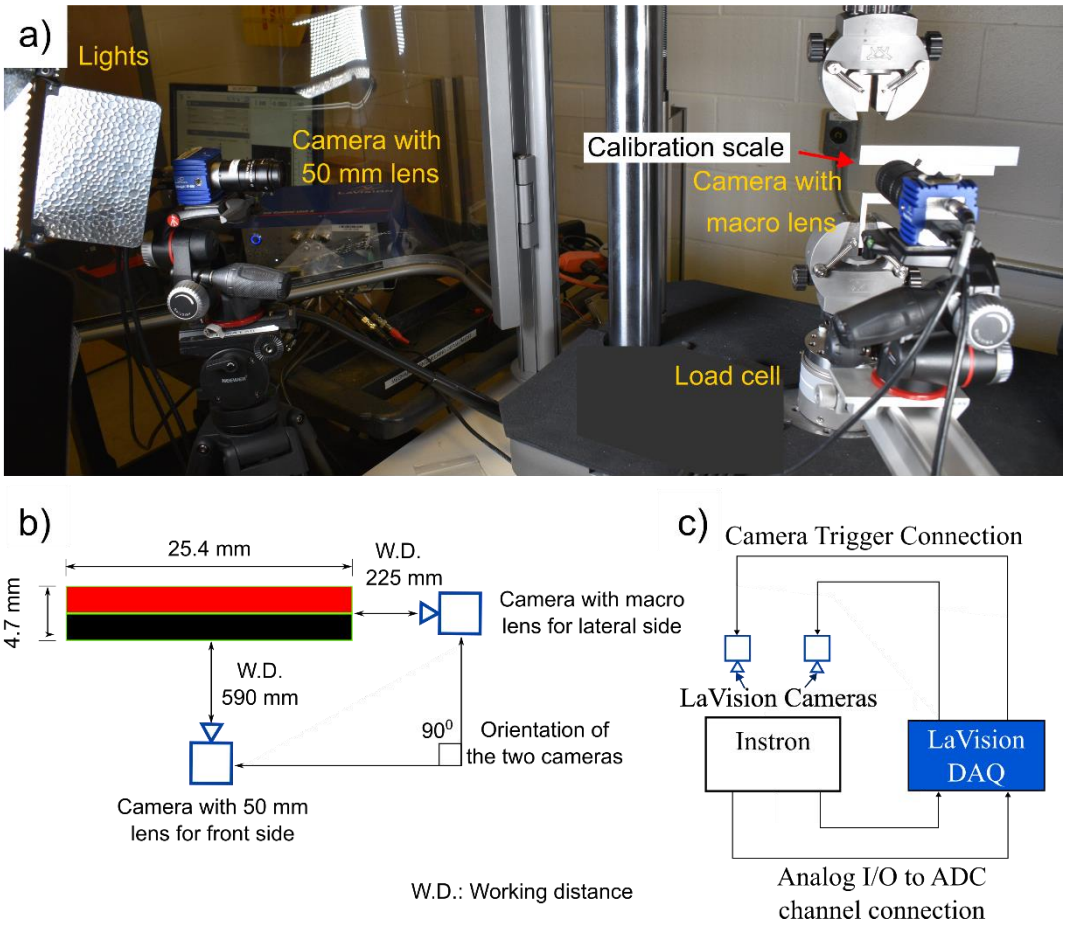

Figure 3-3: (a) Experimental setup of the shear testing with the cameras for DIC, (b) Schematic diagram of setup of cameras with respect to a test sample; c) Wiring diagram for imaging and synchronization of front-view and side-view imaging systems.

3.2.3.2 Data acquisition

The analog voltage data was acquired from the testing machine for each individual frame, as shown in Figure 3-3(c). The applied load was converted to output analog voltage using a scaling factor of 517 N per volt, which was then converted to stress using the overlap cross-section area of the lap joints.

3.2.3.3 2D DIC Imaging Processing

All the acquired images were processed using a commercial image processing software (Davis version 10.2 Strainmaster, LaVision GmbH, Göttingen, Germany) to measure the displacement and strain of the lap joint samples. The images captured by the two cameras simultaneously for two different views of the samples were separated into different frames for calibration in the DaVis software. The images collected with the 50 mm lens were calibrated using a two-level 3D calibration plate (Type 058-5-SSDP, LaVision GmbH, Göttingen, Germany) with the reference point at the middle of the sample in the first frame. The images with the macro lens were scaled using a steel ruler (182-105, Mitutoyo Canada Inc., Mississauga, ON) with the reference point to the left of the sample. The calibration targets are a reference for scaling the captured images with minimum error. The correlation performed for each individual frame before failure was the sum of differential where each image is correlated to the previous image. The specimen images with the 50 mm lens were processed with a subset size of 15 pixels and a step size of 7 pixels for correlation. On the contrary, the specimen images with the macro lens were processed with a subset size of 25 pixels and a step size of 12 pixels for correlation.

Rectangular digital strain gauges were constructed on both the front and lateral view of the samples in the Davis software, as shown in Figure 3-4, to calculate the average strain in the different parts of the sample. Average axial strains at four different regions on the samples were evaluated by constructing 23.5 mm × 9.5 mm virtual strain gauges in the DIC software, as shown in Figure 3-4(a). Two strain gauges were placed at the two extreme ends of the overlap region to assess the strain at the ends of the overlap region.

Two 2 mm × 8mm virtual strain gauges, as shown in Figure 3-4(b), were constructed for the lateral side of the sample to assess the average shear strain in those regions. Two virtual strain gauges, as shown in Figure 3-4(b), were constructed for the lateral side of the sample to assess the average shear strain in those regions. The remaining two strain gauges were placed above and below the overlap region.

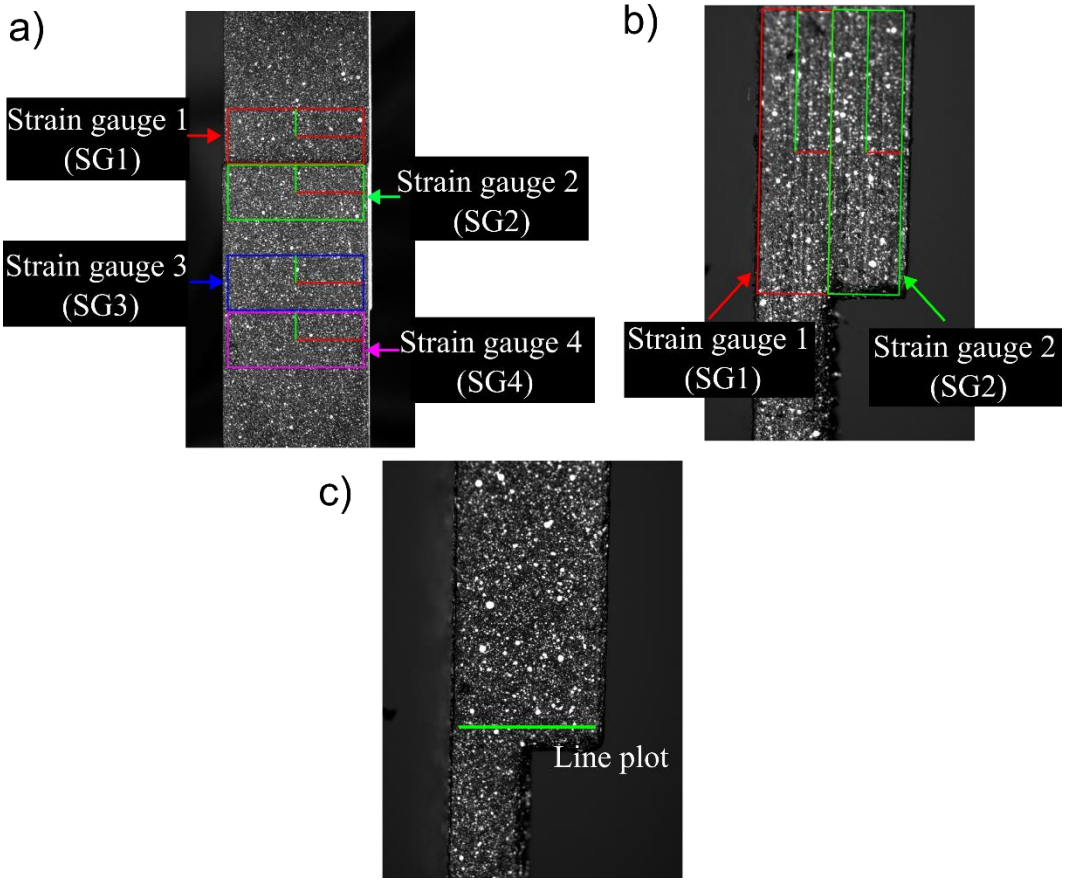

Figure 3-4: Post-processing in DaVis software. (a) Strain gauges on the front view of the sample; (b) Strain gauges on the lateral view of the sample; (c) Line plot on the lateral view of the sample.

3.2.4 Microscopic imaging

The samples were cut at the cross-section of the overlap region using a high-speed cut-off machine (Mecatome T260, PRESI, Hungary) and examined under a microscope to observe the layer adhesion at the boundary interface. Cut samples were mounted in a transparent resin (West System 105 Epoxy Resin, West System, US) mixed with a transparent hardener (West System 207 Hardener, West System, US) in a ratio of 3.7:1 by weight. It was cured for 24 hours, after which the mounted samples were prepared using a grinding and polishing machine (StarGrind^{TM} 200-2V, Microstar 2000, Canada) through five steps of grinding using 180, 400, 600, 800, and 1200 grit silicon carbide papers. This helps to remove any unwanted modifications at the cross-section of the samples due to the cutting technique and reveal the true microstructure of the interface. A 0.05µm alumina powder was used to polish the samples after grinding at 300 rpm. Microscopic images of the samples were taken using a 6 Megapixel Microscope camera (Zeiss Axiocam 506 color, Carl Zeiss Microscopy GmbH, Göttingen, Germany). The microscope had multiple magnification lenses, of which the 20x and the 40x lens were used to take the images of the interface of the samples. The 400x lens from a digital micro hardness tester (MetLab, MetLab Corporation, Canada) was also used to take images of the interface at a higher zoom ratio.

3.3 Results and discussion

3.3.1 Thermogravimetric analysis

As discussed in Chapter 2, Kabir et al. [34] demonstrated the fibre volume fraction in an Onyx composite filament was 10.5% using TGA. In this study, the mass reduction of the

different filament samples during the TGAs using nitrogen as purge gas as shown in Figure 3-5. The TGA curve shows that the PETG starts decomposing at approximately 385°C. The average weight percentage of the three samples used in TGA at 750°C was 19.051%, which was the carbon content of those samples after PETG was decomposed. This remaining carbon content is the carbon weight fraction of the PETC filament used in the study, which is found to be quite close to the manufacturer's specification of 20% carbon fiber weight fraction.

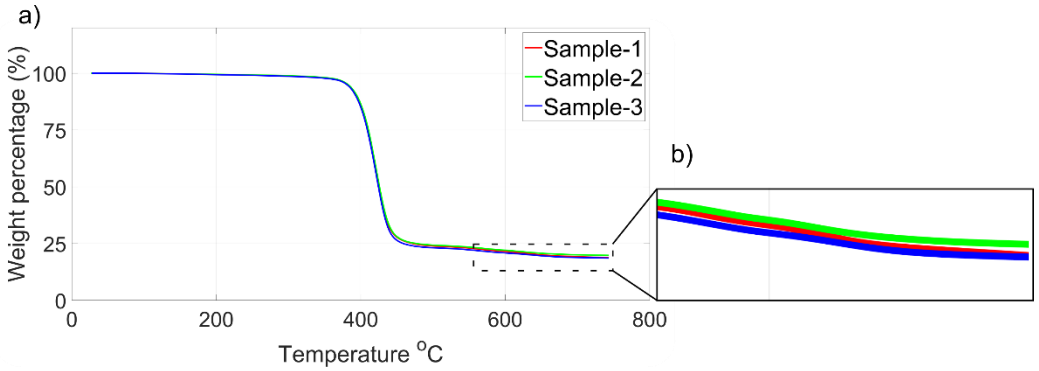

Figure 3-5: (a) Thermogravimetric analysis of PETC filament determining the carbon weight percentage. (b) Zoomed-in view of the plot showing the carbon weight percentage of the three different samples.

3.3.2 Mechanical properties

3.3.2.1 Axial strain

2D DIC technique was used to get the full field strain measurements on the 3D-printed single lap joint samples. This technique provides accurate strains with proper calibration and minimal fit error, which was 0.513 in this study. The 2D images of the axial strain distributions on the surface of all the samples under loads from 100 N to 1950 N, after which all the samples fail, have been shown in Figure 3-6. A 24 mm × 45 mm ROI, as shown in

Figure 3-2, has been chosen to obtain the average strains in the area around the overlap area, which is the main interest of this study. The strain variations show the increment of strains as the applied load increases over time, illustrated by the rich red strain fields. High strains can be observed right above and below the overlap area, especially for the homogenous lap joint samples and the PETG-PETC sample, as they fail under higher loads. The heterogenous PLA-PETG and PLA-PETC samples can be seen to fail at lower loads, even when the strains around the overlap area were lower compared to the other samples.

For the heterogenous PLA-PETG and PLA-PETC samples, the strains are particularly high along the upper boundary of the overlap area, as seen in Figure 3-6. After this, the two parts delaminate and separate from each other, showing weak adhesion. As shown in Figure 3-7, both the samples undergo cohesive failure, where the other overlap area can be seen completely.

All the homogenous samples and the heterogenous PETG-PETC samples exhibit higher strains above and below the overlap area and undergo stock break failure. The adhesion in the overlap area was better than the two heterogeneous samples PLA-PETG and PLA-PETC and, hence, did not delaminate at the overlap region.

From the plots in Figure 3-8 and Figure 3-9, it can be seen that the strain is highest outside and above the overlap region covered by the red rectangular box denoting strain gauge 1. For the homogenous samples and the PETG-PETC sample, the strains gradually increase significantly in that region, as seen in the strain maps in Figure 3-6 and in the plots in Figure 3-8 and Figure 3-9**.** The samples then rupture at the region above the overlap region due to strain localization. Average strains within the overlap region are low when compared to the

average strains outside the overlap region, and hence, the strains are well-distributed throughout the samples and do not produce any excessive stress in the overlap region. However, the multi-material PETG-PETC outperforms the homogenous PETG and PETC samples, its base materials, and has shown similar strength as the homogenous PLA sample. Both the PLA-PLA sample and PETG-PETC samples fail after 1950 N.

For the heterogeneous samples PLA-PETG and PLA-PETC, strain increases right at the upper boundary of the overlap region. As the load increases, the strain starts creeping upwards in the direction of the applied load right from the joint interface. The PLA-PETG samples then delaminate cleanly at the interface due to weak adhesion between the two dissimilar materials at 400 N. PLA-PETC samples also delaminate at approximately 500 N, showing weak adhesion.

The weaker heterogenous lap joints PLA-PETG and PLA-PETC also show similar axial stress vs strain plots, as seen in Figure 3-9. The axial strain increases significantly at strain gauge 1 for both samples as load increases, which shows that the strain along the boundary interface creeps along it and then delaminates along that plane. The heterogeneous PETG-PETC samples' axial stress vs strain plots follow a similar pattern as the other homogenous materials as load increases. PETG-PETC samples show similar mechanical behavior as the homogenous samples and even fail at similar regions.

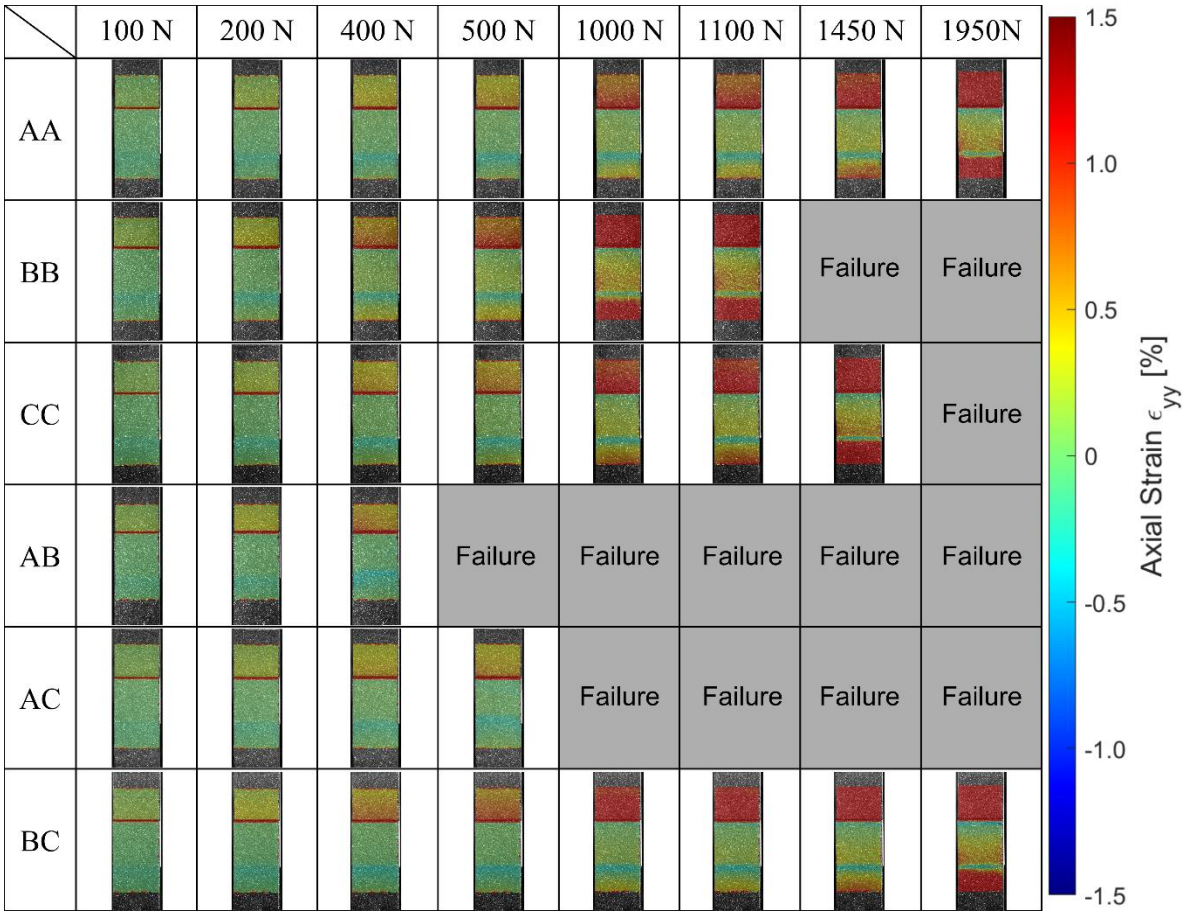

Figure 3-6: Axial strain distributions in different samples under different loads. Sample manufacturing codes are summarized in Table 3-2.

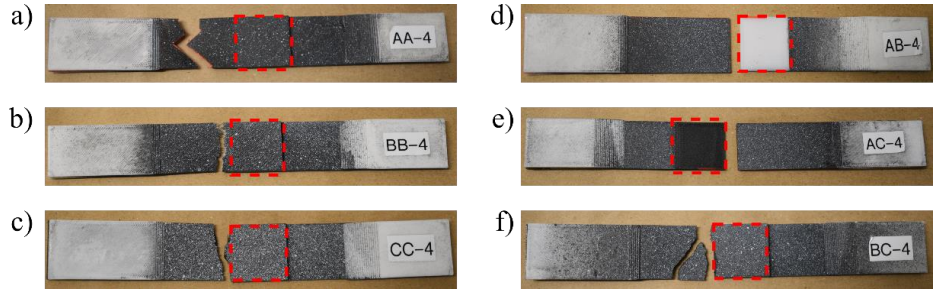

Figure 3-7: Samples after failure; (a) PLA-PLA, (b) PETG-PETG, (c) PETC-PETC, (d) PLA-PETG, (e) PLA-PETC, (f) PETG-PETC. The overlap area has been highlighted in red. Sample manufacturing codes are summarized in Table 3-2.

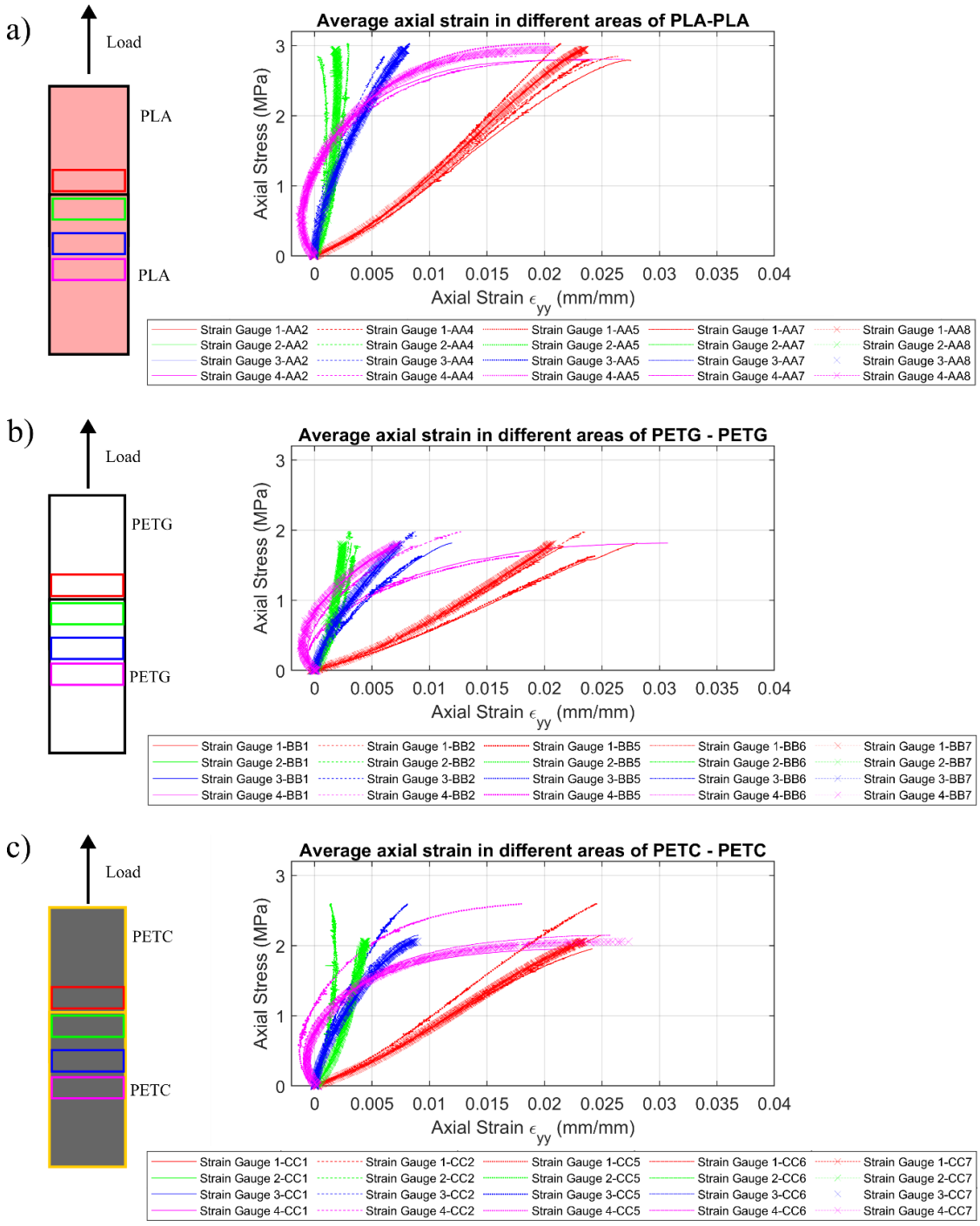

Figure 3-8: Stress vs average strain plots for the different samples in the different areas of the samples for each homogenous combination; (a) PLA-PLA; (b) PETG-PETG; (c) PETC-PETC. Sample manufacturing codes are summarized in Table 3-2.

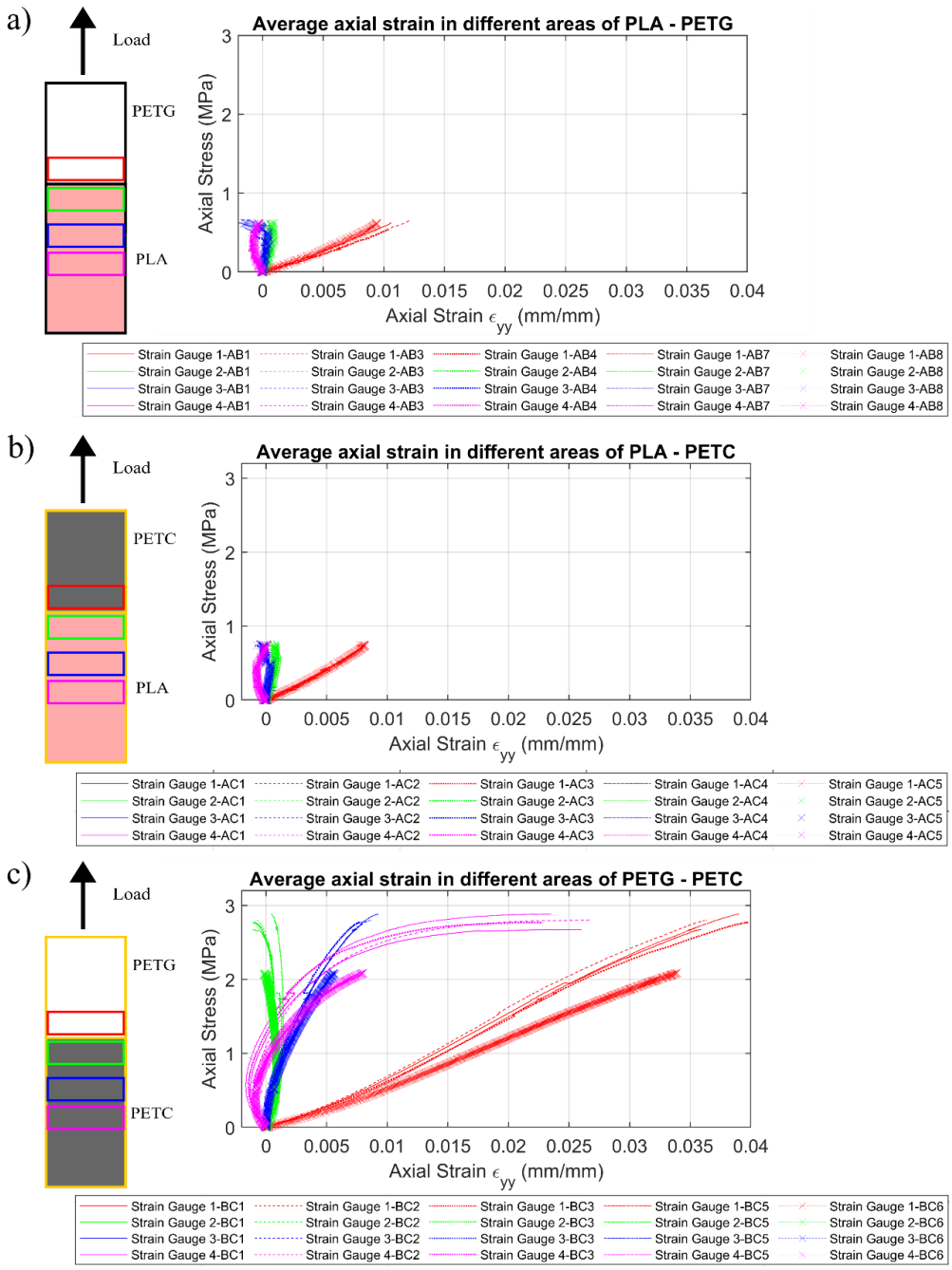

Figure 3-9: Stress vs average axial strain plots for the different samples in the different areas of the samples for each heterogeneous combination; (a) PLA-PETG; (b) PLA-PETC; (c) PETG-PETC. Sample manufacturing codes are summarized in Table 3-2.

3.3.2.2 Shear strain

The shear strain maps for all the sample combinations have been shown in Figure 3-10**.** The shear strain maps were obtained from the images taken through DIC for the lateral view of the samples. This provides a better understanding of the sample's mechanical behavior at the interface of the overlap region. Shear strain is found to be more evenly spread out for the homogenous samples and the PETG-PETC sample. For the heterogenous PLA-PETG and PLA-PETC samples, shear strains increase from the bottom of the overlap region and creep along the interface as load increases. The failure also happens right along the localized stress region.

The difference in shear strain distributions is quite prominent in the multi-material samples, where the strain in the two regions is unequal, as seen in Figure 3-12. The individual material orientation for each sample combination has been indicated in Figure 3-11 and Figure 3-12. Figure 3-12 indicates that the average shear strain in the two heterogenous lap joints increases as stresses increase on the samples. The shear stress vs strain plots in the heterogenous PLA-PETG and PLA-PETC show similar patterns while failing at lower loads compared to the other samples. The PETG-PETC sample again shows similar patterns in the shear stress vs train plot before failing close to 1950 N.

In the homogenous samples, the shear stress vs strain plots tend to converge at maximum stress for both the regions covered by strain gauge 1 and strain gauge 2. But, for the PETG-PETC samples, the shear vs strain plots do not converge like the homogenous samples. This shows the difference in mechanical behavior between the two different materials in the same sample.

The shear stress vs strain plots for the different homogenous samples as well as the weaker heterogeneous materials as illustrated in Figure 3-11 and Figure 3-12, exhibit a high degree of consistency. This indicates that the sample fabrication process was both consistent and suitable for ensuring repeatability.

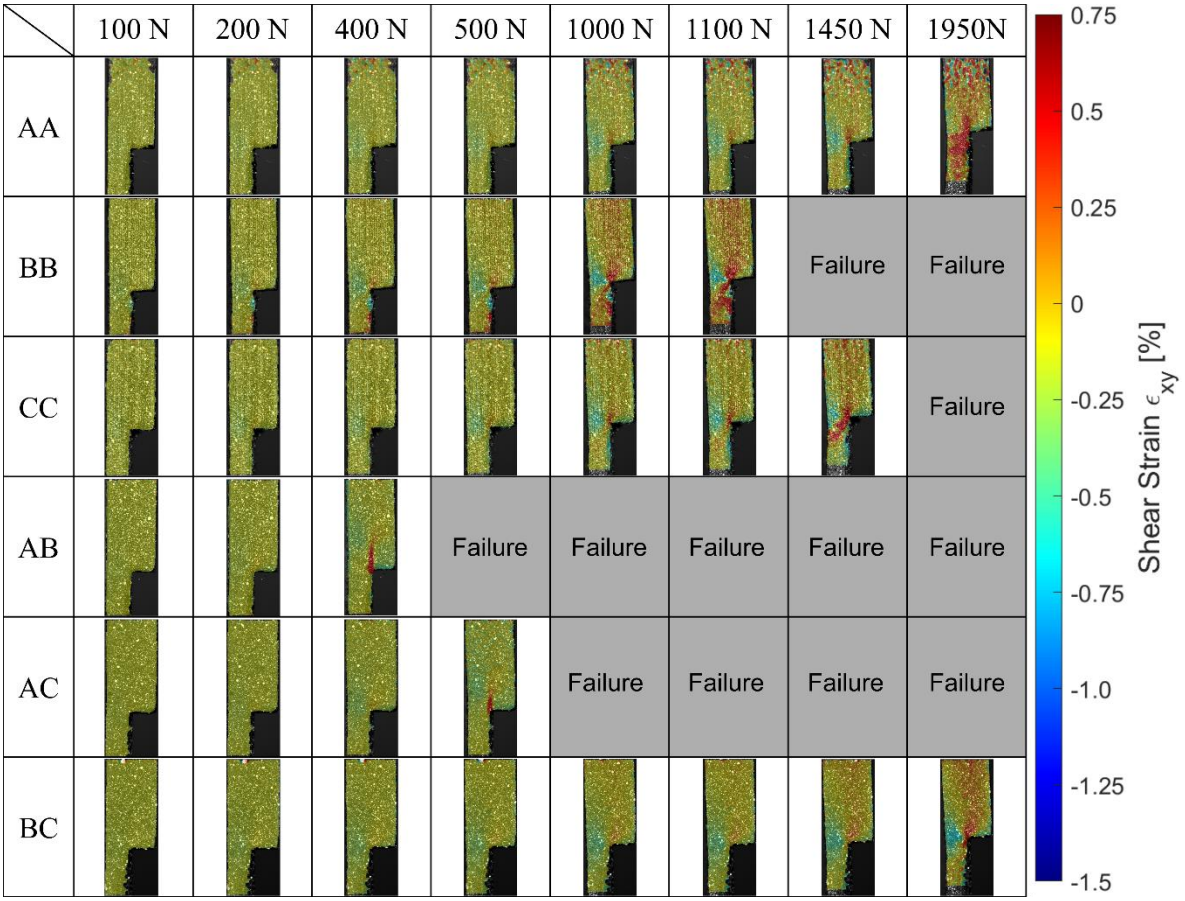

Figure 3-10: Shear strain maps of all the different sample combinations at different loads. Sample manufacturing codes are summarized in Table 3-2.

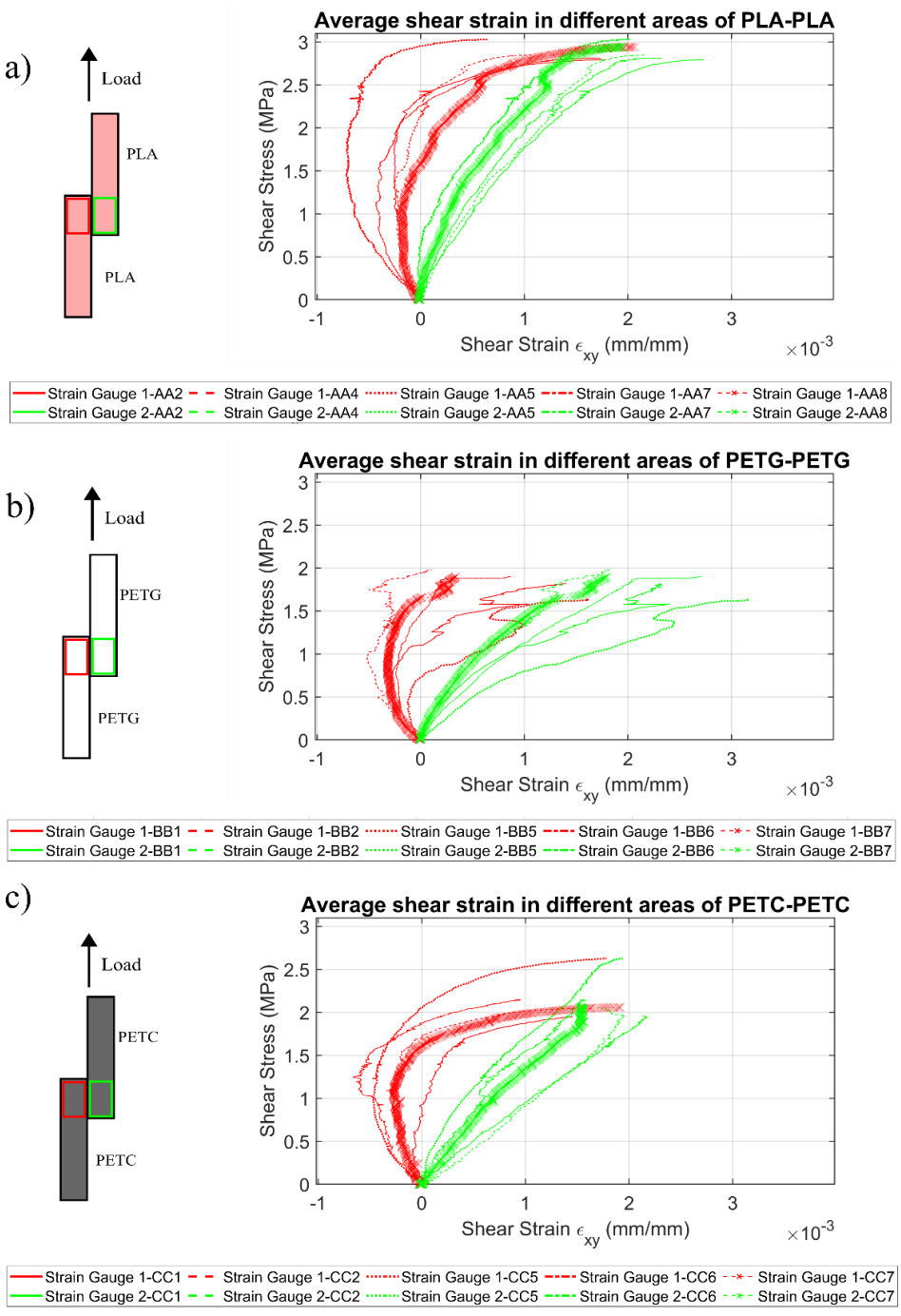

Figure 3-11: Stress vs average shear strain plots for all the samples in different areas of the samples for the homogenous combinations; (a) PLA-PLA; (b) PETG-PETG; (c) PETC-PETC. Sample manufacturing codes are summarized in Table 3-2.

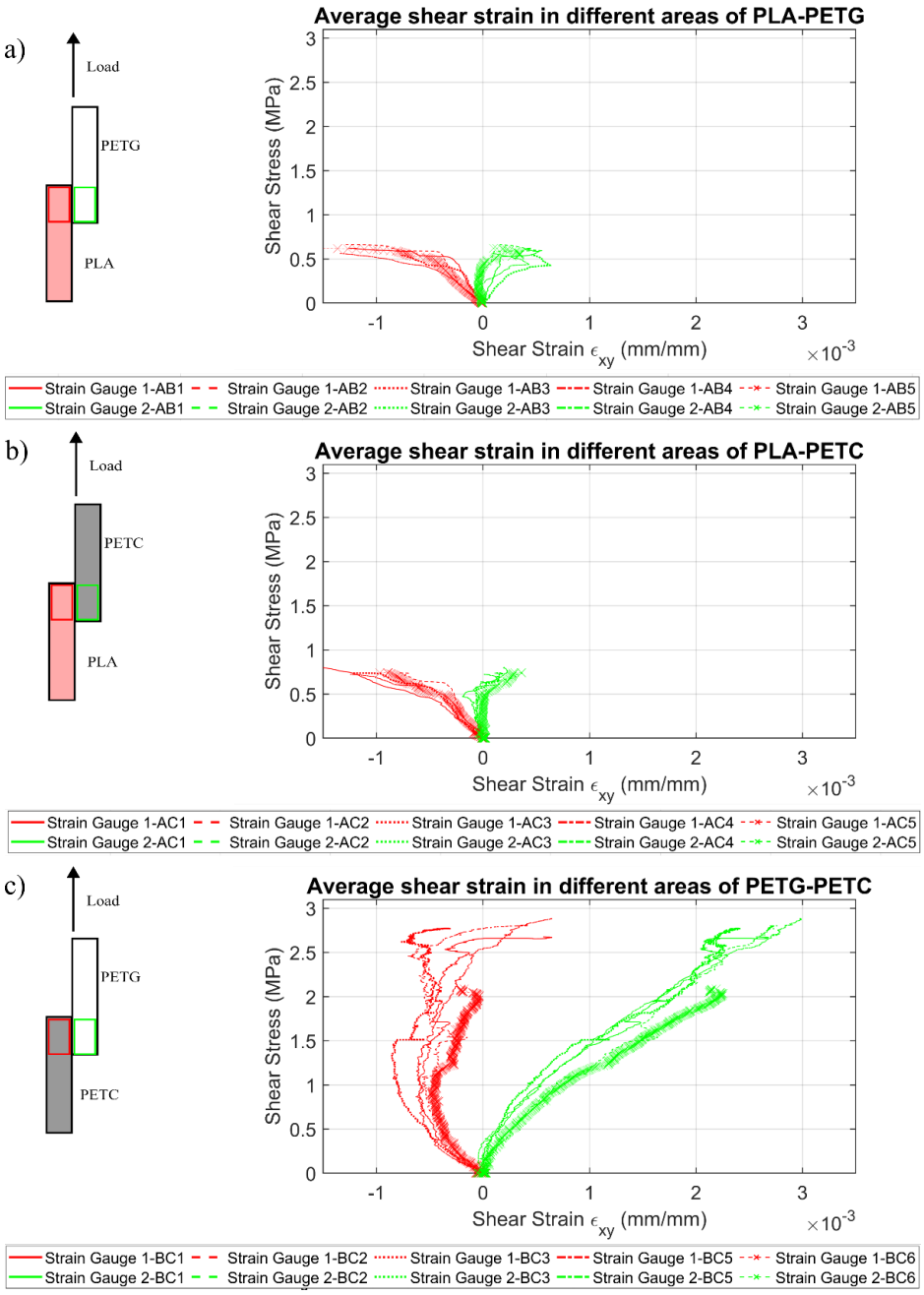

Figure 3-12: Shear stress vs average shear strain plots for all the samples in different areas of the samples for the heterogeneous combinations; (a) PLA-PETG; (b) PLA-PETC; (c) PETG-PETC. Sample manufacturing codes are summarized in Table 3-2.

3.3.2.2.1 Horizontal line plot

Shear strain along the green horizontal line in Figure 3-4(c) has been analyzed in the DaVis software as shown in Figure 3-13. The horizontal green line illustrates the line plot which determines varying shear strains along the horizontal line for different material combinations. The shear strains are highest along the lap joint interface within the overlap area. Thus, there is less possibility of fracture within the overlap area except at the interface. Notably, the two heterogeneous samples PLA-PETG and PLA-PETC exhibit the highest shear strains at the interface, and these are the only samples that delaminate at the interface. Thus, this figure aids in predicting the failure of the samples.

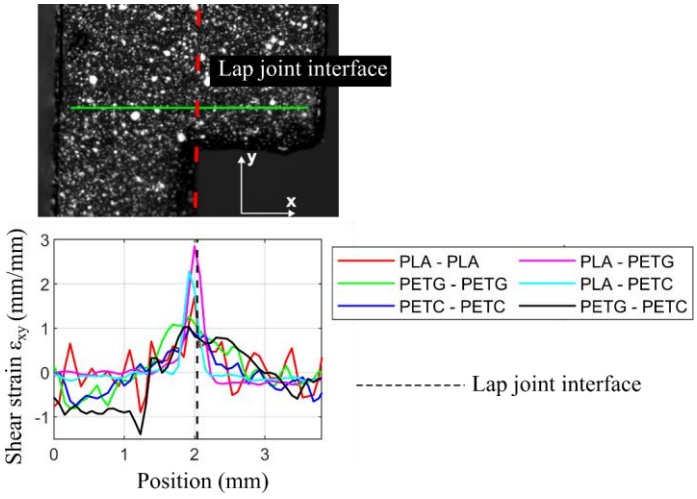

Figure 3-13*:* Shear strains along the lap joint interface for all the samples just before failure.

3.3.3 Optical microscopy

The microstructure at the boundary interface of all the different sample combinations was investigated, as seen in Figure 3-14. The figure shows the cross-section of the interface of

the different sample combinations in this study. For the homogenous samples, the rasters are attached to the immediate neighbouring rasters as seen in conventional 3D printed parts. The sample combinations with PETC show a significant presence of carbon fibers at the interface. PLA-PETC has higher strength than PLA-PETG, while PETG-PETC has higher strength than PETC-PETC. This can be attributed to the presence of short carbon fibers, especially at the interface layer, which provides better adhesion.

In their study, Dam et al. showed that the rougher surface due to the presence of carbon fibers contributed to mechanical interlocking in a steel-epoxy adhesive interface [49]. The rougher surface will also have more microscopic peaks and valleys compared to a smooth surface. This will increase the contact surface area of the different substrates and provide improved adhesion.

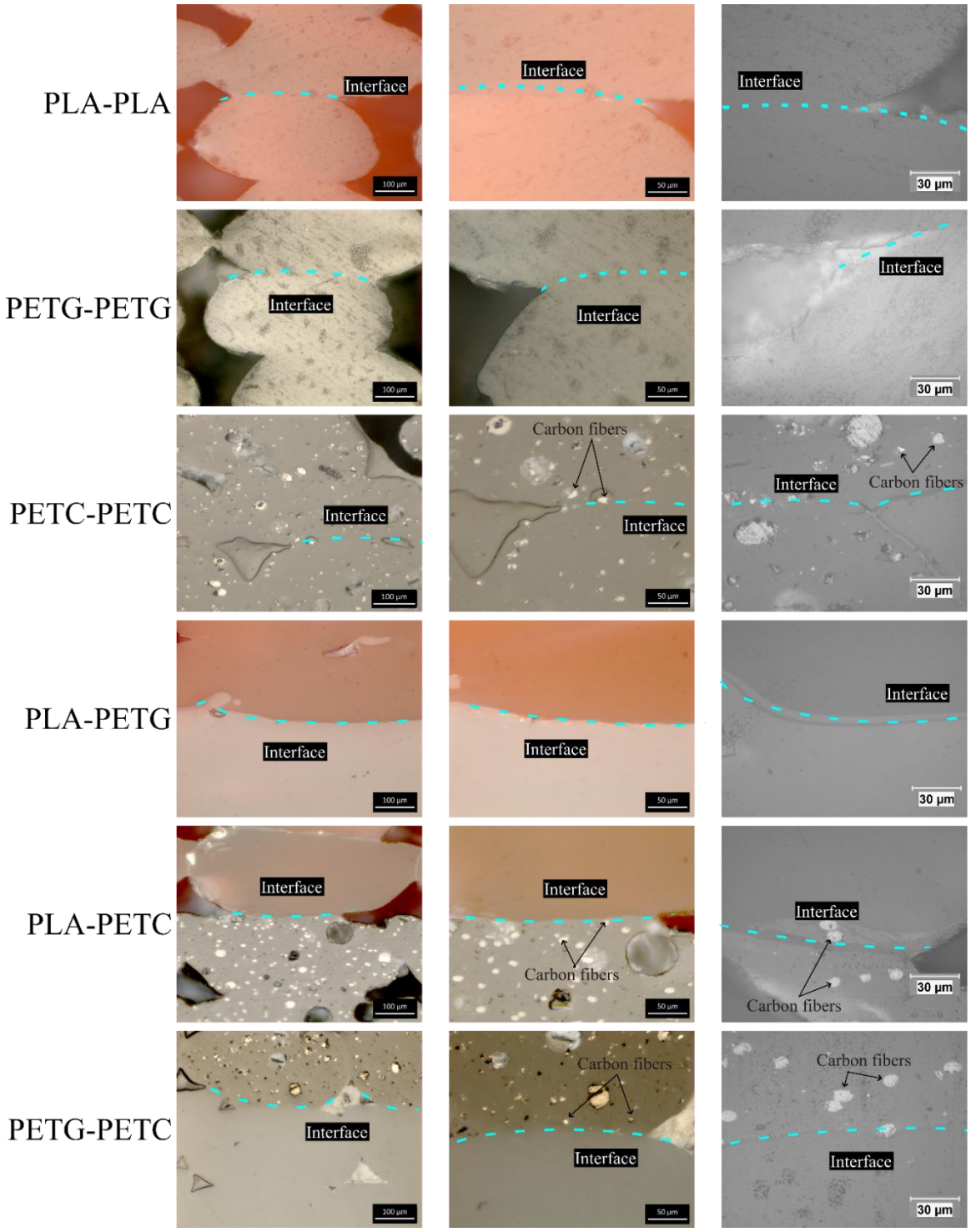

Figure 3-14: Microscopic images of the samples at the boundary interface in the overlap region with different zoom lens.

3.3.4 Statistical analysis

The lap shear strength of all the sample combinations has been shown in Table 3-4. PLA-PLA has the highest strength of all the sample combinations used in this study. However, the lap shear strength of PETG-PETC was found to be higher than the other two homogenous sample combinations – PETG-PETG and PETC-PETC. Hence, it was possible to fabricate a multi-material sample using FFF, which demonstrated better adhesive performance than its homogenous samples made from either filament. The remaining two heterogeneous PLA-PETG and PLA-PETC samples had the lowest shear strength, which was expected based on the previous literature discussions.

One-way analysis of variance (ANOVA) was performed to find the statistical correlation between the different sample combinations, as listed in Table 3-5. However, one-way ANOVA is limited to finding the variability of the mean of a particular group relative to the other groups. It cannot evaluate the correlation between the two groups.

Subsequently, a Tukey-Kramer test was performed to find the correlation between all the sample combinations. It estimates the difference between the means of different groups and measures a 95% confidence interval for the difference between the corresponding population means.

Table 3-6 shows the p-value for all the 15 pairs of combinations possible with the sample combinations used in this study. The p-value was higher than 0.05 for [PLA-PLA and PETG-PETC], [PETG-PETG and PETC-PETC], and [PLA-PETG and PLA-PETC]. This signifies that there is no evidence that supports the null hypothesis for these combinations, i.e. these pairs are statistically significantly different at 5% significance level.

This is quite evident from Figure 3-15 the lap shear strength of the PETG-PETC samples is quite similar to that of PLA-PLA. The homogenous PETC-PETC and PETG-PETG also have similar lap shear strengths, which support the statistical analysis. The heterogeneous PLA-PETC and PLA-PETG have almost similar lap shear strengths, too.

Thus, the Tukey-Kramer test supports the analysis that the heterogeneous PETG-PETC samples achieved similar lap shear strengths to the homogenous PLA-PLA samples and, hence, almost similar adhesive strengths.

Contemporary studies show that Ribeiro et al. experienced a 90.77% loss approximately of tensile strength in their PLA-TPU multi-material 3D-printed mechanically interlocked sample compared to their PLA-PLA homogenous samples [21]. The results from the study with zebra crossing specimens by Lopes et al. [22] showed a decrease of 73.07% tensile strength for the PLA-PET samples compared to the PLA-PLA samples and a decrease of 67.2% tensile strength compared to the PET-PET samples. In this study, the heterogeneous PLA-PETG samples had a 79.3% loss of shear strength decline compared to PLA-PLA samples and 67.28% shear strength decline compared to PETG-PETG samples. PLA-PETC samples had a loss of 73.62% shear strength compared to PLA-PLA samples and a loss of 64.97% shear strength compared to PETC-PETC samples. But, the PETG-PETC samples achieved 22.72% higher strength than PETC-PETC samples and 46.08 % higher strength than PETG-PETG samples. Thus, at least one multi-material sample that had a better strength than its base material homogenous samples was obtained.

Table 3-4: Lap shear strength of all the sample combinations

Samples	Lap shear strength (MPa)
PLA-PLA	2.923 ± 0.11
PETG-PETG	1.849 ± 0.79
PETC-PETC	2.201 ± 0.25
PLA-PETG	0.605 ± 0.05
PLA-PETC	0.771 ± 0.03
PETG-PETC	2.701 ± 0.33

Table 3-5: One way ANOVA analysis for the samples

Source	SS	df	MS	F	p-value (Prob>F)
Groups	23.5742	5	4.7148	139.82	$p < 0.001$
Error	0.8093	24	0.0337	-	-
Total	24.3835	29	-	-	-

Table 3-6: Tukey-kramer analysis for all the samples

Index	Sample 1	Sample 2	Lower Bound	Difference	Upper bound	p-value
1	PLA-PLA	PETG-PETG	0.7143	1.0734	1.4324	$p < 0.001$
2	PLA-PLA	PETC-PETC	0.3626	0.7217	1.0807	0.00002
3	PLA-PLA	PLA-PETG	1.9594	2.3185	2.6776	$p < 0.001$
4	PLA-PLA	PLA-PETC	1.7926	2.1517	2.5108	$p < 0.001$
5	PLA-PLA	PETG-PETC	-0.1379	0.2212	0.5803	**0.4237**
6	PETG-PETG	PETC-PETC	-0.7108	-0.3517	0.0074	**0.0573**
7	PETG-PETG	PLA-PETG	0.8861	1.2452	1.6042	$p < 0.001$
8	PETG-PETG	PLA-PETC	0.7192	1.0783	1.4374	$p < 0.001$
9	PETG-PETG	PETG-PETC	-1.2113	-0.8522	-0.4931	$p < 0.001$
10	PETC-PETC	PLA-PETG	1.2378	1.5969	1.9559	$p < 0.001$
11	PETC-PETC	PLA-PETC	1.0709	1.4300	1.7891	$p < 0.001$
12	PETC-PETC	PETG-PETC	-0.8596	-0.5005	-0.1414	0.0029
13	PLA-PETG	PLA-PETC	-0.5259	-0.1668	0.1923	**0.7054**
14	PLA-PETG	PETG-PETC	-2.4564	-2.0973	-1.7383	$p < 0.001$
15	PLA-PETC	PETG-PETC	-2.2896	-1.9305	-1.5714	$p < 0.001$

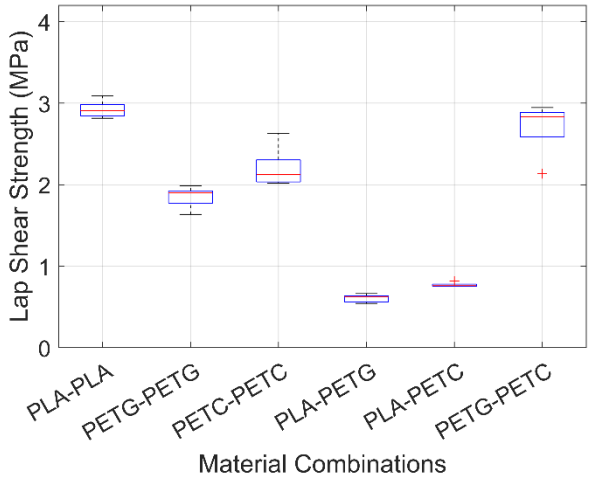

Figure 3-15: Box and whisker plot showing the lap shear strength of the different lap joint sample combinations.

3.3.5 Surface modifications

Future work could involve modifying the surface layer at the joint interface to achieve different levels of surface roughness, as illustrated in Figure 3-16 and subsequently investigating the adhesion properties of the lap joints. The smooth surface in the picture was obtained by using the default ironing setting in the same printer used in the study, and the rougher surface was obtained using the default fuzzy skin settings. The rougher surface may improve the adhesion at the interface by providing more points of contact.

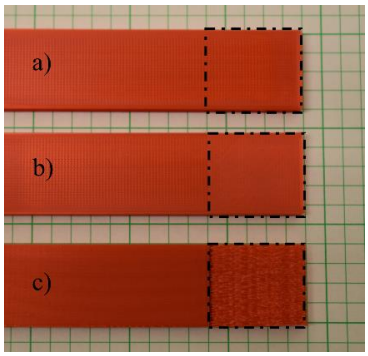

Figure 3-16: Lap joint interface highlighted with the dotted box with different surface characteristics; (a) sample without any surface modifications; (b) sample with a smooth surface; (c) sample with a rough surface.

3.4 Conclusion

Single lap shear joints were fabricated with three different thermoplastic 3D printing filaments to evaluate the adhesion of the multi-material structures at the boundary interface. Shear test was performed on the samples to evaluate the shear strains and strain concentrations on the sample using 2D DIC technique. The two cameras used for the DIC effectively captured the front and lateral sides of the samples to evaluate the strains on all sides of the samples. Microscopic images of the cross-section of the samples were also analyzed to investigate the microstructure at the interface. The findings of this study can be summarized as following:

(1) The heterogenous PETG-PETC single lap joints achieved a strength similar to the lap shear strength of the homogenous PLA-PLA sample, which had the highest strength of all the samples. The PETG-PETC sample had higher strength than the other homogenous samples. This is the first time an FFF-

printed multi-material could achieve a strength similar to a homogenous sample or surpass the strength of other homogenous sample combinations.

(2) This study suggests the possibility of fabricating FFF-printed composite structures with better mechanical performance than conventional homogenous FFF-printed structures. The key is to choose the same base materials to maintain the chemical affinity between the polymers, introduce fibers in one of the base materials, and tailor it according to its potential application. The presence of fibers also provides additional strength to the structures.

(3) The 2D DIC technique highlights the lack of a suitable standard for evaluating multi-material polymeric structures without adhesives. Though this study was tailored according to ASTM D5868, it is meant for polymer bonding with adhesive. Some of the parameters were tuned to fit the current study, but the strain maps from DIC point out that the two dissimilar materials undergo different strains due to the different mechanical properties of the different materials. So, the samples do not undergo pure shear loading conditions. Other standards, such as ASTM D5379 [50] or Iosipescu shear test [51] could be explored to determine if they would be a better fit to analyse multi-material 3D-printed lap joints.

(4) In the future, the percentage of carbon fibers in the filament can be varied to find an optimum fiber content in the filament which may increase the strength of the multi-material 3D-printed structures.

(5) Setting the raster orientation in alignment with the load direction can enhance the shear strength of 3D-printed samples, particularly when strong adhesion is observed, as seen in samples that experience stock-break failure.

(6) The manufacturing technique discussed in this study can be optimized in future research and integrated into robotic arms of 3D printers to fabricate complex functional parts with reinforcements in critical locations.

3.5 Acknowledgements

The authors gratefully acknowledge the financial support from the Natural Sciences and Engineering Research Council of Canada RGPIN-2018-05899.

3.6 References

[1] I. Energy Agency, Review 2021 Assessing the effects of economic recoveries on global energy demand and CO 2 emissions in 2021 Global Energy, 2021. www.iea.org/t&c/.

[2] M. Gebler, A.J.M. Schoot Uiterkamp, C. Visser, A global sustainability perspective on 3D printing technologies, Energy Policy 74 (2014) 158–167. https://doi.org/10.1016/j.enpol.2014.08.033.

[3] H. Zhang, D. Liu, T. Huang, Q. Hu, H. Lammer, Three-dimensional printing of continuous flax fiber-reinforced thermoplastic composites by five-axis machine, Materials 13 (2020). https://doi.org/10.3390/ma13071678.

[4] N. Jayanth, K. Jaswanthraj, S. Sandeep, N.H. Mallaya, S.R. Siddharth, Effect of heat treatment on mechanical properties of 3D printed PLA, J Mech Behav Biomed Mater 123 (2021). https://doi.org/10.1016/j.jmbbm.2021.104764.

[5] S.J. Ahn, H. Lee, K.J. Cho, 3D printing with a 3D printed digital material filament for programming functional gradients, Nat Commun 15 (2024). https://doi.org/10.1038/s41467-024-47480-5.

[6] E.C. Ehman, G.B. Johnson, J.E.Villanueva-Meyer, S. Cha, A.P. Leynes, P.E. Larson, T.A. Hope, PET/MRI: Where might it replace PET/ct? Journal of Magnetic Resonance Imaging 46 (2017) 1247–1262. doi:10.1002/jmri.25711.

[7] C.G. Amza, A. Zapciu, G. Constantin, F. Baciu, M.I. Vasile, Enhancing mechanical properties of polymer 3D printed parts, Polymers (Basel) 13 (2021) 1–18. https://doi.org/10.3390/polym13040562.

[8] M. Selva Priya, K. Naresh, R. Jayaganthan, R. Velmurugan, A comparative study between in-house 3D printed and injection molded ABS and PLA polymers for low-frequency applications, Mater Res Express 6 (2019). https://doi.org/10.1088/2053-1591/ab2776.

[9] L. Behalek, J. Safka, M. Seidl, J. Habr, J. Bobek, Fused deposition modelling vs. Injection moulding: Influence of fiber orientation and layer thickness on the mechanical properties, MM Science Journal 2018 (2018) 2722–2726. https://doi.org/10.17973/MMSJ.2018_12_2018117.

[10] T. Chen, J. Mueller, K. Shea, Integrated Design and Simulation of Tunable, Multi-State Structures Fabricated Monolithically with Multi-Material 3D Printing, Sci Rep 7 (2017). https://doi.org/10.1038/srep45671.

[11] J.P. Moore, C.B. Williams, Fatigue properties of parts printed by PolyJet material jetting, Rapid Prototyp J 21 (2015) 675–685. https://doi.org/10.1108/RPJ-03-2014-0031.

[12] M. Sugavaneswaran, G. Arumaikkannu, Analytical and experimental investigation on elastic modulus of reinforced additive manufactured structure, Mater Des 66 (2015) 29–36. https://doi.org/10.1016/j.matdes.2014.10.029.

[13] M. Sugavaneswaran, G. Arumaikkannu, Modelling for randomly oriented multi material additive manufacturing component and its fabrication, Mater Des 54 (2014) 779–785. https://doi.org/10.1016/j.matdes.2013.08.102.

[14] L.S. Dimas, G.H. Bratzel, I. Eylon, M.J. Buehler, Tough composites inspired by mineralized natural materials: Computation, 3D printing, and testing, Adv Funct Mater 23 (2013) 4629–4638. https://doi.org/10.1002/adfm.201300215.

[15] A. Nazir, O. Gokcekaya, K. Md Masum Billah, O. Ertugrul, J. Jiang, J. Sun, S. Hussain, Multi-material additive manufacturing: A systematic review of design, properties, applications, challenges, and 3D printing of materials and cellular metamaterials, Mater Des 226 (2023). https://doi.org/10.1016/j.matdes.2023.111661.

[16] B. Berman, 3-D printing: The new industrial revolution, Bus Horiz 55 (2012) 155–162. https://doi.org/10.1016/j.bushor.2011.11.003.

[17] J.P. Moore, C.B. Williams, Fatigue properties of parts printed by PolyJet material jetting, Rapid Prototyp J 21 (2015) 675–685. https://doi.org/10.1108/RPJ-03-2014-0031.

[18] Micallef J., Beginning design for 3D printing, New York: Apress 2015.

[19] F. Awaja, M. Gilbert, G. Kelly, B. Fox, P.J. Pigram, Adhesion of polymers, Progress in Polymer Science (Oxford) 34 (2009) 948–968. https://doi.org/10.1016/j.progpolymsci.2009.04.007.

[20] J. Mueller, D. Courty, M. Spielhofer, R. Spolenak, K. Shea, Mechanical Properties of Interfaces in Inkjet 3D Printed Single- and Multi-Material Parts, 3D Print Addit Manuf 4 (2017) 193–199. https://doi.org/10.1089/3dp.2017.0038.

[21] M. Ribeiro, O. Sousa Carneiro, A. Ferreira da Silva, Interface geometries in 3D multi-material prints by fused filament fabrication, Rapid Prototyp J 25 (2019) 38–46. https://doi.org/10.1108/RPJ-05-2017-0107.

[22] L.R. Lopes, A.F. Silva, O.S. Carneiro, Multi-material 3D printing: The relevance of materials affinity on the boundary interface performance, Addit Manuf 23 (2018) 45–52. https://doi.org/10.1016/j.addma.2018.06.027.

[23] X. Tian, T. Liu, C. Yang, Q. Wang, D. Li, Interface and performance of 3D printed continuous carbon fiber reinforced PLA composites, Compos Part A Appl Sci Manuf 88 (2016) 198–205. https://doi.org/10.1016/j.compositesa.2016.05.032.

[24] K.I. Mori, T. Maeno, Y. Nakagawa, Dieless forming of carbon fibre reinforced plastic parts using 3D printer, in: Procedia Eng, Elsevier Ltd, 2014: pp. 1595–1600. https://doi.org/10.1016/j.proeng.2014.10.196.

[25] A. Pilipović, P. Raos, M. Šercer, Experimental analysis of properties of materials for rapid prototyping, International Journal of Advanced Manufacturing Technology 40 (2009) 105–115. https://doi.org/10.1007/s00170-007-1310-7.

[26] W. Zhong, F. Li, Z. Zhang, L. Song, Z. Li, Short fiber reinforced composites for fused deposition modeling, Mater Sci Eng: A 301 (2001) 125–130. doi:10.1016/s0921-5093(00)01810-4.

[27] M.L. Shofner, K. Lozano, F.J. Rodríguez-Macías, E. V. Barrera, Nanofiber-reinforced polymers prepared by fused deposition modeling, J Appl Polym Sci 89 (2003) 3081–3090. https://doi.org/10.1002/app.12496.

[28] X. Wang, M. Jiang, Z. Zhou, J. Gou, D. Hui, 3D printing of polymer matrix composites: A review and prospective, Compos B Eng 110 (2017) 442–458. https://doi.org/10.1016/j.compositesb.2016.11.034.

[29] N. Li, Y. Li, S. Liu, Rapid prototyping of continuous carbon fiber reinforced polylactic acid composites by 3D printing, J Mater Process Technol 238 (2016) 218–225. https://doi.org/10.1016/j.jmatprotec.2016.07.025.

[30] X. Tian, T. Liu, Q. Wang, A. Dilmurat, D. Li, G. Ziegmann, Recycling and remanufacturing of 3D printed continuous carbon fiber reinforced PLA composites, J Clean Prod 142 (2017) 1609–1618. https://doi.org/10.1016/j.jclepro.2016.11.139.

[31] ISO 11358–1, Plastics—Thermogravimetry (TG) of polymers—Part 1: General principles, ISO, 2014; https://www.iso.org/standard/59710.html. (accessed 31 Jan 2022).

[32] ASTM E1131-20 ISO 11358, Standard test method for compositional analysis by thermogravimetry (2020). https://doi.org/10.1520/E1131-20.

[33] D. Bücheler, A. Kaiser, F. Henning, Using Thermogravimetric Analysis to Determine Carbon Fiber Weight Percentage of Fiber-Reinforced Plastics, Compos B Eng 106 (2016) 218–223. https://doi.org/10.1016/j.compositesb.2016.09.028.

[34] S.M.F. Kabir, K. Mathur, A.F.M. Seyam, The Road to Improved Fiber-Reinforced 3D Printing Technology, Technologies (Basel) 8 (2020). https://doi.org/10.3390/technologies8040051.

[35] R. Meier, I. Kahraman, A.T. Seyhan, S. Zaremba, K. Drechsler, Evaluating vibration assisted vacuum infusion processing of hexagonal boron nitride sheet modified carbon fabric/epoxy composites in terms of interlaminar shear strength and void content, Compos Sci Technol 128 (2016) 94–103. https://doi.org/10.1016/j.compscitech.2016.03.022.

[36] X. Zhu, L. Yao, X. Yang, H. Sun, A. Guo, A. Li, H. Yang, Spatiotemporal expression of KHSRP modulates Schwann cells and neuronal differentiation after sciatic nerve injury, International Journal of Biochemistry and Cell Biology 48 (2014) 1–10. https://doi.org/10.1016/j.biocel.2013.12.008.

[37] K. Naito, H. Oguma, Tensile properties of novel carbon/glass hybrid thermoplastic composite rods, Compos Struct 161 (2017) 23–31. https://doi.org/10.1016/j.compstruct.2016.11.042.

[38] R.Y. Yee, T.S. Stephens, A TGA technique for determining graphite fiber content in epoxy composites, Thermochimica Acta 272 (1996), 191–199. doi:10.1016/0040-6031(95)02606-1.

[39] J. Qiu, M.K. Idris, G. Grau, G.W. Melenka, Electroluminescent strain sensing on carbon fiber reinforced polymer, Compos B Eng 238 (2022). https://doi.org/10.1016/j.compositesb.2022.109893.

[40] A. Armanfard, G.W.Melenka, Experimental evaluation of carbon fibre, fibreglass and aramid tubular braided composites under combined tension–torsion loading, Compos Struct 269 (2021) 1140-1149. doi:10.1016/j.compstruct.2021.114049.

[41] C. Unlusoy, G.W. Melenka, Flexural testing of cellulose fiber braided composites using three dimensional digital image correlation, Compos Struct 230 (2019). https://doi.org/10.1016/j.compstruct.2019.111538.

[42] M. Jerabek, Z. Major, R.W. Lang, Strain determination of polymeric materials using digital image correlation, Polym Test 29 (2010) 407–416. https://doi.org/10.1016/j.polymertesting.2010.01.005.

[43] D14 Committee. Test Method for Lap Shear Adhesion for Fiber Reinforced Plastic (FRP) Bonding n.d. https://doi.org/10.1520/D5868-01R23.

[44] J.M. Chacón, M.A. Caminero, E. García-Plaza, P.J. Núñez, Additive manufacturing of PLA structures using fused deposition modelling: Effect of process parameters on mechanical properties and their optimal selection, Mater Des 124 (2017) 143–157. https://doi.org/10.1016/j.matdes.2017.03.065.

[45] What is PETG? (everything you need to know). TWI n.d. https://www.twi-global.com/technical-knowledge/faqs/what-is-petg#WhatisitUsedFor (accessed July 17, 2024)..

[46] H. Schreier, J.J. Orteu, M.A. Sutton, Image correlation for shape, motion and deformation measurements: Basic concepts, theory and applications, Springer US, 2009. https://doi.org/10.1007/978-0-387-78747-3.

[47] B. Duncan, Developments in testing adhesive joints, in: Advances in Structural Adhesive Bonding, Elsevier Inc., 2010: pp. 389–436. https://doi.org/10.1533/9781845698058.3.389.

[48] D.O. Adams, DO, D.F. Adams, Tabbing Guide for Composite Test specimens, Washington, D.C, Springfield, Va.: Office of Aviation Research, Federal Aviation Administration, Available to the public through the National Technical Information Service, 2002.

[49] J.P.B. van Dam, S.T. Abrahami, A. Yilmaz, Y. Gonzalez-Garcia, H. Terryn, J.M.C. Mol, Effect of surface roughness and chemistry on the adhesion and durability of a steel-epoxy adhesive interface, Int J Adhes Adhes 96 (2020). https://doi.org/10.1016/j.ijadhadh.2019.102450.

[50] Standard Test Method for Shear Properties of Composite Materials by the V-Notched Beam Method 1, (n.d.). https://doi.org/10.1520/D5379_D5379M-1.

[51] D.F. Adams, The Iosipescu shear test method as used for testing polymers and Composite Materials. Polymer Composites 11 (1990), 286–290. doi:10.1002/pc.750110506..

Chapter 4 Analysis of the interface properties of multi-material vat photopolymerization (VPP) printed polymer structures

4.1 Introduction

Additive manufacturing (AM) or 3D printing is constantly evolving to transform into a robust manufacturing technology for intelligent manufacturing from a prototyping technology [1]. The main advantage of AM is the fabrication of parts with reduced lead times [2], allowing for easy design modifications and fewer components [3,4], all while achieving customized mechanical performance [5]. AM also allows for the fabrication of complex lattice structures that are difficult to manufacture with traditional manufacturing processes. Yin et al. [6] and Craddock et al. [7] have demonstrated the impact energy absorption of AM polymer lattices. The Zero2-R Matrix ID Trench helmet from Vicis, featuring customized 3D-printed pads with complex lattice structures, was rated by the NFL as the best player protection in 2023 [8]. Presently the AM market is valued at USD 20.73 billion in 2023 and is estimated to grow at a compound annual growth (CAGR) of 23.3% until 2030 [9]. GE Aerospace and CFM International currently utilize over ten additively manufactured parts that have been approved by the U.S. Federal Aviation Administration (FAA) for use in commercial aviation engines, including GE90, CFM LEAP, GEnx, and GE9X engines [10]. A recent study demonstrated the potential of additively manufactured heart valves for valve replacement surgery, particularly for valvular heart disease (VHD) [11]. The study found that these 3D-printed

valves exhibited mechanical performance comparable to that of native valve leaflets. These studies underscore the wide-ranging commercial applications of AM technologies across various manufacturing sectors, including aerospace and biomedical, reflecting the transformative potential of this advancing technology.

Recently, researchers have been interested in exploring AM with multiple materials in a single print, as industries increasingly focus on using AM to manufacture parts with enhanced visual aesthetics and functionality. Multi-material 3D printing (MM3DP) allows for the fabrication of assemblies with fewer components, eliminating the need for fasteners, glue, clips, and other materials. This approach helps reduce the weight, size, and cost of assemblies while having mechanical performance comparable to that of traditional assemblies [12]. In several studies, multiple material containers were installed in a single nozzle design using the direct ink writing (DIW) technique to print with multiple materials involving elastomers [13–15]. A DNA shoe from PENSAR was designed using a flexible material with a rigid material through material jetting (MJ). Further studies have also explored 3D printing with multi-materials with fused filament fabrication (FFF), but it has resulted in a weak interface at the interface joint [16,17].

DLP is a class of vat photopolymerization technology that initiates the polymerization reaction locally to cure the resin layer by layer, like stereolithography (SLA). Instead of a laser, a digital micromirror device (DMD) based projector is used to print the entire layer in a single step, resulting in faster printing speed than Stereolithography (SLA). In general, optics magnification and the number of mirrors used in the DMD system determine the resolution of the DLP system, which ranges from 10 to 50 μm [5]. Compared to the

conventional AM techniques, digital light processing (DLP) has a number of advantages such as high resolution, dimensional accuracy, varying cross-linking density, relatively lower cost, and excellent surface quality [18–20]. DLP enables the modification of the microscopic structure of layers of printed parts, whereas FFF can only alter the macroscopic structure of its printed parts.

VPP has been used to print flexible materials such as aliphatic urethane diacrylate (AUD) [21], poly(trimethylene carbonate) [22], and hydrogels, with very low Young's modulus of approximately 4 MPa. However, limited studies are available on multi-material 3D printed structures using VPP. A combination of hard and flexible resin material formulation was used to fabricate micro actuators with a minimum feature size of 200 μm using high-resolution DLP by Song et al. [23], where the hard material provides reinforcement to the actuators.

Most of the multi-material studies using 3D printing suggest that the analysis of the interface joint of the multi-material structures is critical for evaluating the feasibility of the printing technique [16,17,24–26]. Polymers generally have low surface free energy and lack polar functional groups on their surface, which results in poor adhesion between layers [27]. Therefore, the strain and failure at the boundary interface of multi-material samples must be evaluated to assess the adhesion between the multi-materials. Non-invasive methods such as digital image correlation (DIC) are particularly suitable for measuring deformation in anisotropic heterogeneous structures [28,29]. DIC is a full-field optical deformation measurement technique generally using a single or stereo camera setup for image acquisition [30]. Random speckles sprayed on the samples prior to mechanical testing increase surface contrast and are tracked through image acquisition and correlated to compute strain and

vector fields. This technique has been used in a number of studies on complex anisotropic structures such as composites [31–33] to determine their non-uniform deformations. DIC has also been found to be a powerful technique for the characterization of polymeric materials [34].

In this study, the adhesion between the multi-materials at the boundary interface was extensively analyzed using single lap joints. The soft resin material was formulated using the techniques introduced by Song et al. [23]. A hard resin material was formulated as a rigid material. The presence of a high concentration of acrylate monomers in both the formulated resins promoted covalent bonding with each other, thus providing strong adhesion. This resulted in strong interlinking between the heterogeneous materials, reducing the possibility of delamination at high-stress concentrations. The mechanical properties of the samples were assessed with shear test on the samples in a universal testing machine. 2D DIC was conducted to determine the surface strain during shear testing, capturing images at two different angles to obtain both front and lateral sample views.

4.2 Materials and methods

4.2.1 Sample preparation

4.2.1.1 Materials

Poly(ethylene glycol) (PEG) (Mn~10,000), PEG (Mn~400), 2-carboxyethyl acrylate (CEA), isobornyl acrylate (IA), diurethane dimethacrylate (DUDMA), diphenyl(2,4,6-trimethylbenzoyl) phosphine oxide (TPO), and sudan orange g (SOG) were purchased from Sigma-Aldrich (Taufkirchen, Germany). 2-propanol was purchased from Carl Roth

(Karlsruhe, Germany). A cross-linker PEG dimethacrylate (PEGDMA) (Mn~10,000), a combination of unmodified PEG (Mn~10,000), methacrylic anhydride, and 4-dimethylaminopyridine (DMAP), was used. The synthesis was done according to Song et al. [23].

4.2.1.2 Resin preparation for 3D printing

The chemicals were weighed into a 250 ml brown glass vial according to the resin formulations in Table 4-1 (soft material) and Table 4-2 (hard material). The mixture was placed in an ultrasonic bath (Elasonic 30H, Elma, Germany) under 50 °C for 60 min, and homogenous resins were yielded.

Table 4-1: Resin formulation for soft material

Chemicals	Weight (%)
CEA	40
PEG (Mn~4000)	30
PEG (Mn~400)	20
PEGDMA (Mn~10,000)	9.67
TPO	0.3
SOG	0.03

Table 4-2: Resin formulation for hard material

Chemicals	Weight (%)
IA	49.84
DUDMA	49.84
TPO	0.3
SOG	0.03

4.2.1.3 Digital Light Processing

Single lap joint samples were designed in SolidWorks (Dassault Systèmes SolidWorks Corporation, Massachusetts, USA) as shown in Figure 4-1(a) and (b) for lap shear test according to ASTM standard D5868 [35]. The dimensions of the samples had to be reduced due to the size limitations of the build plate in the DLP printer used. The two aforementioned resins were used to manufacture three different samples – a homogenous hard material lap joint (IADD), a homogenous soft material (SPEG), and a multi-material lap joint (MM) using the two different resins. Five samples were fabricated for each material combination to examine the repeatability and consistency of the test.

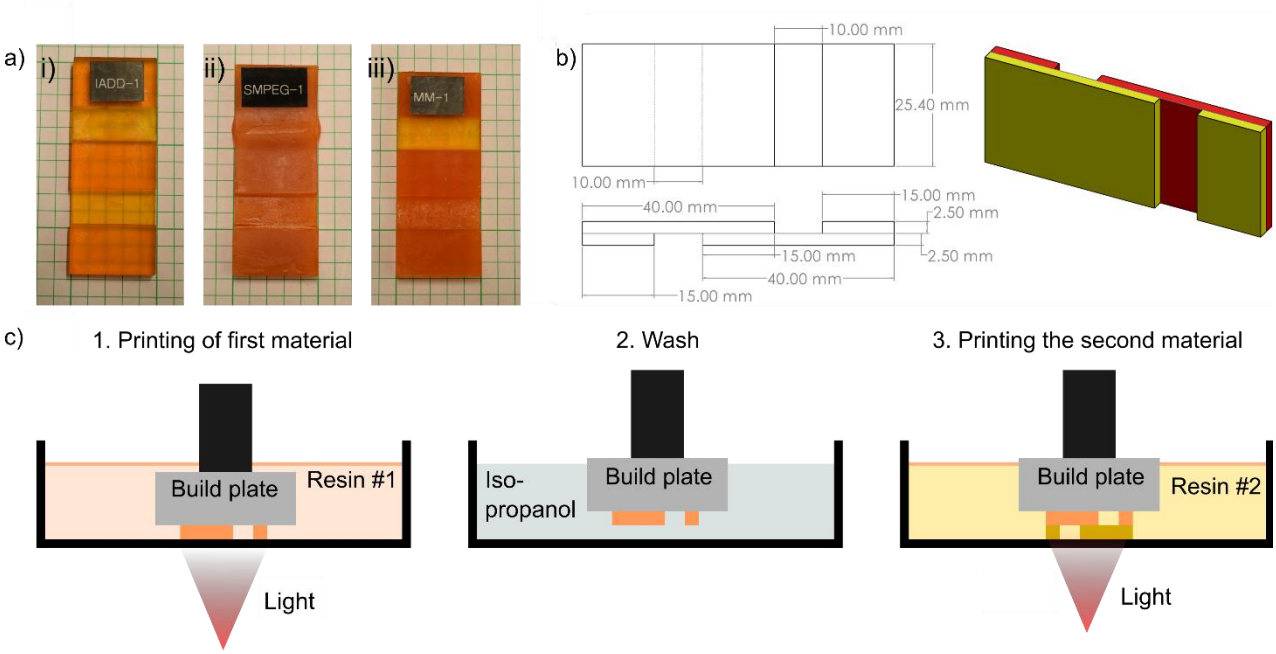

Figure 4-1:Samples, sample dimensions, and printing process. (a) Samples after printing (i) IADD, (ii) SPEG, and (iii) MM; (b) Schematic representation of the 3D printed single lap joints; c) Schematic representation of the printing process of the samples in three steps: printing the material with the first resin, washing it with isopropanol to remove residues, and then printing the second material.

The STL files for the samples were sliced using the slicer software Asiga Composer (Asiga, Erfurt, Germany) and printed using a DLP printer, Asiga Max X35 (Asiga, Erfurt, Germany). The printing parameters have been listed in Table 4-3.

Table 4-3: Printing parameters for soft and hard resin

Printer settings	SPEG	IADD	Units
Layer thickness	0.05	0.05	mm
Light intensity	8.4	8.4	mW/cm^2
Exposure time	5	8	s
Burn-in time	16	21	s
Separation distance	10	10	mm
Printing temperature	50	50	℃
Z-compensation	0	0	mm
XY-compensation	-0.100	-0.037	mm

When printing with SPEG resin, a 76×53×1 mm microscopic glass slide (Objektträger, Paul Marienfeld GmbH & Co. KG, Lauda-Königshofen, Germany) was attached to the build plate for better surface quality of the soft resin. For the multi-material lap joint, SPEG was printed on the build plate, after which the sample was washed with isopropanol to remove any uncured resin, as shown in Figure 4-1(c). The resin tank was changed to the IADD resin tank for further printing of the hard material on top of SPEG. There were no alignment issues, as both the resin tanks used were of the exact specifications.

After the samples were printed, they were flushed with isopropanol to remove uncured resin residues and then blow-dried with nitrogen air. They were then post-cured using a UV curing chamber (Asiga Flash UV chamber, Asiga, Erfurt, Germany).

The hardness of the hard and soft material samples was tested with a shore A durometer (560-10A, Shore-a Hardness Tester, Gain Express Holdings Ltd, Hong Kong).

4.2.1.4 Shear test

The single-lap joints were subjected to a shear load using an Instron ElectroPlus E3000 (Instron, Norwood, USA) equipped with a 3kN load cell. The samples were loaded at a constant crosshead speed of 5 mm/min. The samples were measured at five different points using 3732XFL-1 (1-inch) and 3732XFL-2 (2-inch) digital micrometers (Starrett, Athol, USA), and the average value was used for further calculations.

4.2.1.5 Surface preparation and painting

A matte black paint was applied to the samples using a flat black spray can (Painter's Touch Flat Black, Rust-Oleum Corp., Concord, ON). A mixture of white paint (5212 Opaque White, Createx Airbrush Colors, Createx Colors, East Granby CT) and reducer (4012 High Performance Reducer, Createx) was then applied to the sample with an airbrush (Paasche Airbrush H-3MH set, Paasche Airbrush Co, Chicago, IL) to create a random white speckle pattern as shown in Figure 4-2. The speckled samples show well-distributed peaks and valleys in the histogram plot in Figure 4-2 for both the front and lateral views of the samples, enabling precise DIC measurement [36].

4.2.2 Imaging setup

4.2.2.1 2D DIC Imaging Setup

Both the front and lateral views of the samples were captured with two high-resolution cameras, as shown in Figure 4-2, (Imager M-lite 5M, LaVision GmbH, Göttingen, Germany),

which were placed at 90° to each other, as shown in Figure 4-3. Images were acquired at a rate of 15 frames per second until the samples failed. The camera and lens characteristics are listed in Table 4-4. A fixed focal length lens (MVL50M23 50 mm, Navitar, Rochester, USA) was used to capture the wider front view, and the camera for imaging the narrower side view was equipped with a macro lens (3.3X macro zoom, Edmund Optics, Barrington, USA). Two LED panels (LED Lighting Panel, Adjustable Intensity, 500 Watt, Neewer) were installed next to the cameras to implement the bright field illumination method for a strong contrast between the white speckles and the black base coat. The cameras and lighting were mounted on different tripods.

Table 4-4: Properties of the DIC imaging setup

Property	Unit	Value for setup for front view	Value for setup for side view
Camera resolution	px x px	2464 x 2056	2464 x 2056
Pixel size	µm	3.45	3.45
Frame rate	Hz	15	15
Image Scaling Factor	px/mm	22	80
Image field of view	mm x mm	115 × 97	31 x 26

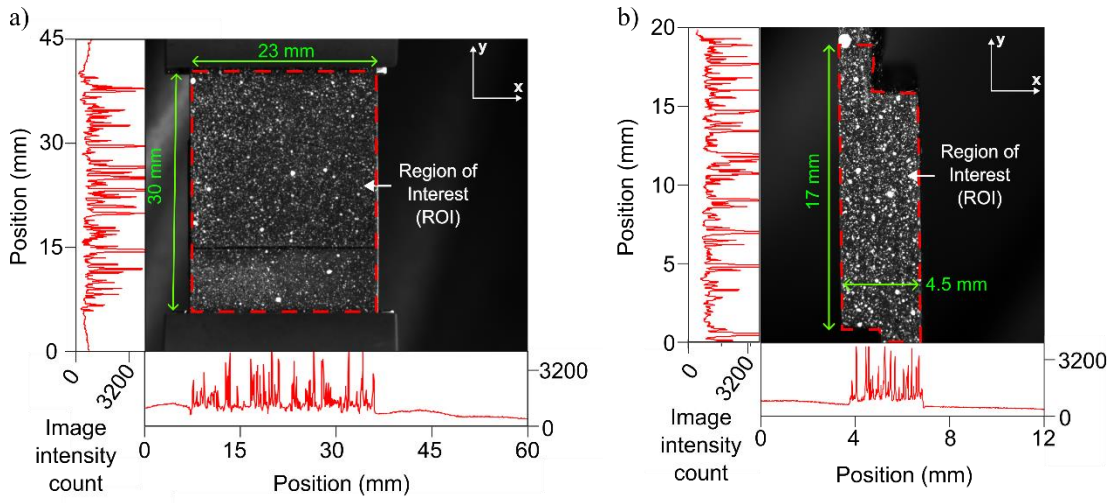

Figure 4-2: Images of the painted and speckled samples from DIC cameras with the respective ROI and image density counts along the two axes. (a) Front view of the sample with 50 mm lens; (b) Lateral view of the sample with macro lens.

4.2.2.2 Data acquisition

Analog voltage data was acquired from the testing machine for each individual frame, as shown in Figure 4-3. The applied load was converted to analog output voltage using a scaling factor of 517 N per volt, which was then converted to stress using the overlap cross-section area of the lap joints.

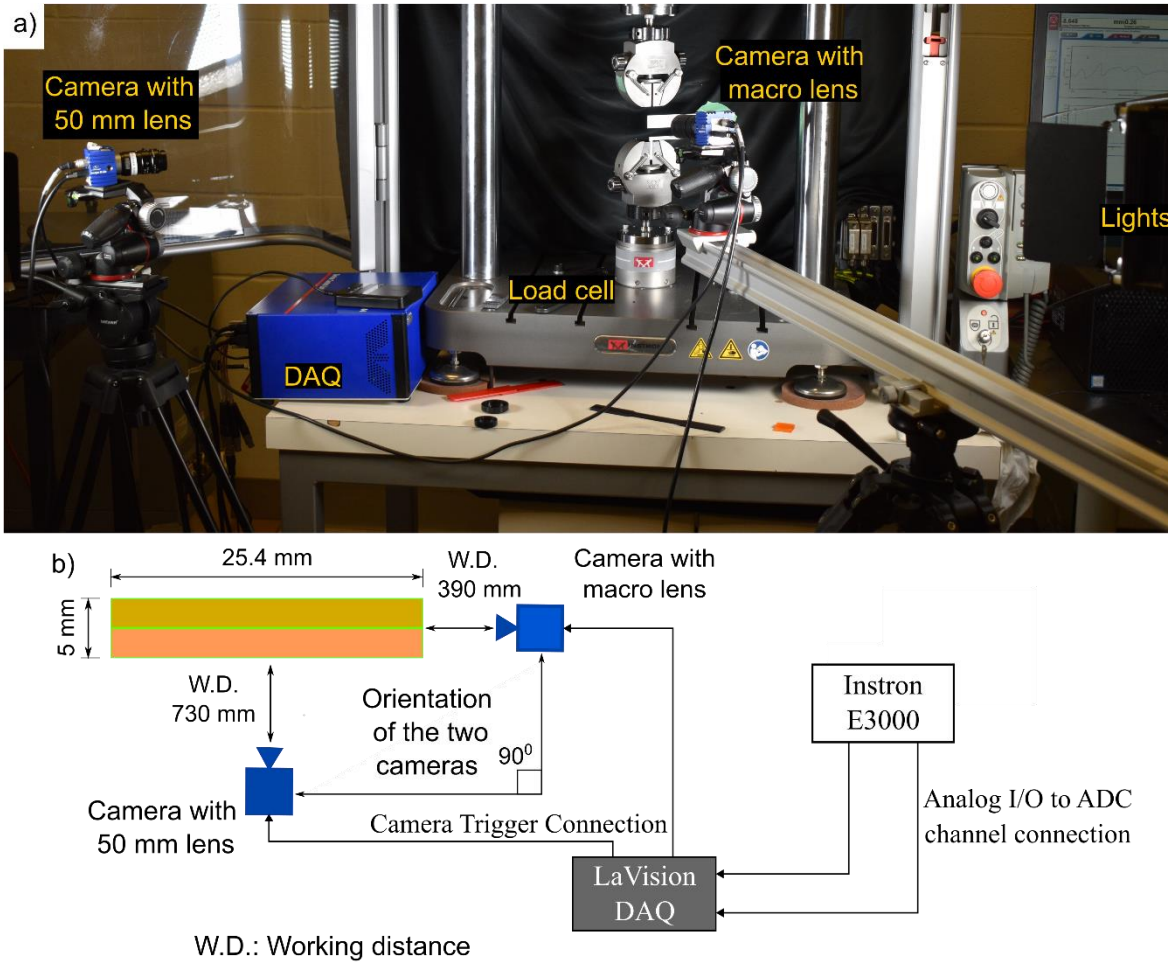

Figure 4-3: (a) Experimental setup of the shear test with two cameras for DIC, (b) Schematic diagram of the camera setup in front of a test sample with wiring connection for imaging and synchronization of front-view and lateral view.

4.2.3 2D DIC Imaging Processing

The images acquired during the lap shear test were processed using a commercial image processing software (Davis version 10.2 Strainmaster, LaVision GmbH, Göttingen, Germany) to measure the displacement and strain of the lap joint samples. Two different views of the samples were separated into different frames for calibration in the Davis software. The images collected with the 50 mm lens were calibrated using a two-level 3D

calibration plate (Type 058-5-SSDP, LaVision GmbH, Göttingen, Germany) with the reference point at the middle of the sample in the first frame. The images taken with the macro lens were scaled using a steel ruler (182-105, Mitutoyo Canada Inc., Mississauga, ON) with the reference point to the left of the sample. The calibration targets provide a reference for scaling the captured images with minimum error. The correlation performed for each individual frame before failure was the sum of differential where each image is correlated to the previous image. The sample images with the 50 mm lens were processed with a subset size of 15 pixels and a step size of 7 pixels for correlation, while the sample images with the macro lens were processed with a subset size of 25 pixels and a step size of 12 pixels.

Within the DIC software, 22.5 mm × 6.5 mm digital strain gauges were constructed on the front side of the samples to determine the average axial strain at different areas. Two strain gauges were placed at the upper and lower parts of the overlap region, while the other two were placed just above and below the overlap region, as shown in Figure 4-4(a). Additionally, two vertical line plots were placed along the length of the sample on the front side, as illustrated in Figure 4-4(c), to calculate the average axial strain along these lines just before the samples failed.

Similarly, two 2.44 mm × 14.71 mm digital strain gauges, as shown in Figure 4-4(c) were also placed on the lateral side of the sample to calculate the average shear strain in each part of the overlap region. Three horizontal lines were plotted on the lateral side, as illustrated in Figure 4-4(d), to determine the shear strain along these lines prior to sample failure.

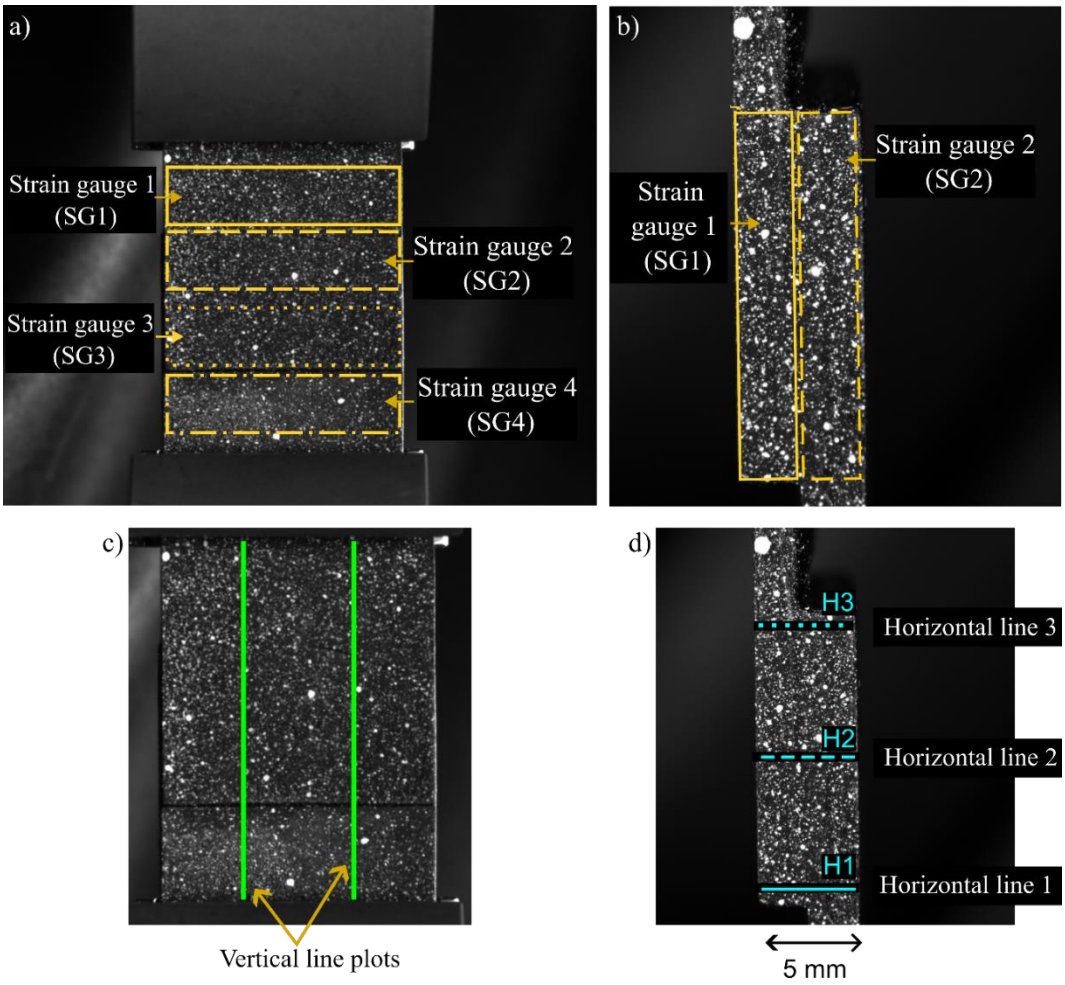

Figure 4-4: Post-processing of DIC data. (a) Digital strain gauges on the front view of the sample; (b) Digital strain gauges on the lateral view of the sample; (c) Vertical line plots on the front side of the sample; (d) Horizontal line plots on the lateral side of the samples at the top, middle and bottom of the overlap region.

4.3 Results and discussion

4.3.1 Mechanical properties

4.3.1.1 Hardness of 3D printed materials

Average hardness of the hard samples (IADD) was determined to be 98.833 HRA with a standard deviation of 1.803, while the average hardness of the soft samples (SPEG) was 75.000 HRA with a standard deviation of 0.764.

4.3.1.2 Analysis of axial strain with DIC

Full-field strain measurements on the 3D-printed single lap joint samples were evaluated using 2D DIC. Strains can be measured with high accuracy using DIC when properly calibrated, with a minimal fit error, which in this study was 0.519. The 2D images of the axial strain distributions on the surface of all the samples under loads from 30 N to 900 N have been shown in Figure 4-5. Axial strain distribution was calculated in the ROI, as illustrated in Figure 4-2.

For the IADD samples, strain concentrations were observed above the overlap region (upper region in Figure 4-5). However, the axial strains in IADD samples were quite low compared to the SPEG samples and the MM samples, showing their rigid and brittle nature. IADD samples did fail at higher loads of approximately 895 N. In contrast, the SPEG samples showed axial strain concentration localized below and above the overlap region (middle row of Figure 4-5). The reddish area denotes the high-strain regions in the samples, and the samples fail exactly at the high-strain region above the overlap area.

The MM samples exhibit higher strains in the entire part below the overlap area as a result of the presence of the soft material, which stretches more at higher loads (lower row in Figure 4-5). Figure 4-6 illustrates that MM samples fail below the overlap region, where strain localization occurs in the softer material. The MM samples also fail at higher loads compared to the SPEG samples because the IADD resin provides additional strength to the samples. No delamination was observed at the lap joint interface; however, stock break failure occurred in all samples [35]. These findings indicate good adhesion, particularly in the heterogeneous multi-material samples.

Average axial strains at four different regions on the front view of the samples, as shown in Figure 4-4, were evaluated by constructing 22.5 mm × 6.5 mm digital strain gauge. The average axial strains in these ROI, as seen in Figure 4-7 and Figure 4-8 further, provide evidence to validate the strain maps in Figure 4-5. The axial stress over strain plots in Figure 4-7 show the stress and strain variations in the three sample combinations as the graphs are plotted with the axes scaled similarly for all the samples. Since the IADD samples fail at higher loads, it also shows that the IADD samples experience significantly higher stress than the SPEG and MM samples. SPEG samples undergo the lowest stresses while having higher axial strains than the IADD samples due to their flexibility. The axial strains were the highest in the multi-material samples, which can be attributed to the heterogeneity of the samples. Since the IADD section of the sample does not stretch notably due to its rigid nature, the SPEG section of the sample experienced a higher strain when the load was applied. The MM samples also experience higher stress than SPEG, combining the properties of both the IADD and SPEG material.

Figure 4-8 provides a detailed representation of the variation among the four front-view strain gauges on the samples by zooming in on the respective plots. Strain gauges 1 and 4, the strain gauges outside of the overlap region, experience an average axial strain of 0.25 % at 0.27 MPa axial stress. The strain gauges in SPEG record higher axial strains than the other strain gauges, which is consistent with the findings of the overview axial strain map (middle row in Figure 4-5), where axial strains were found to be localized above and below the overlap region. Strain gauge 4 in the heterogeneous MM sample recorded an average axial strain of 0.5 % at 0.5 MPa, which was twice the strain of SPEG before failure. It exhibits the highest strain of all the strain gauges of MM samples, as the strain is mainly localized below the overlap area (lower row in Figure 4-5).

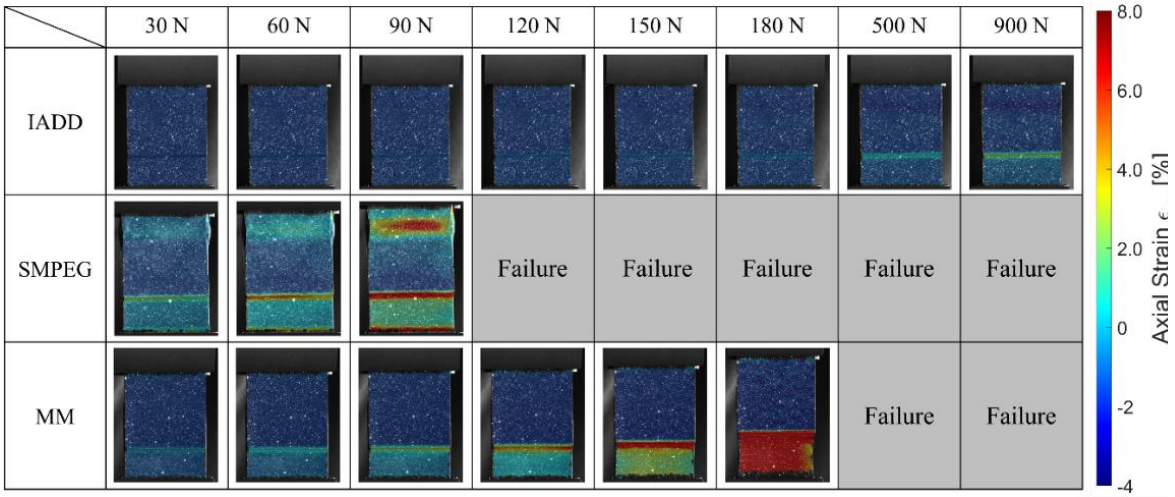

Figure 4-5: Axial strain patterns of the three samples at defined load stages

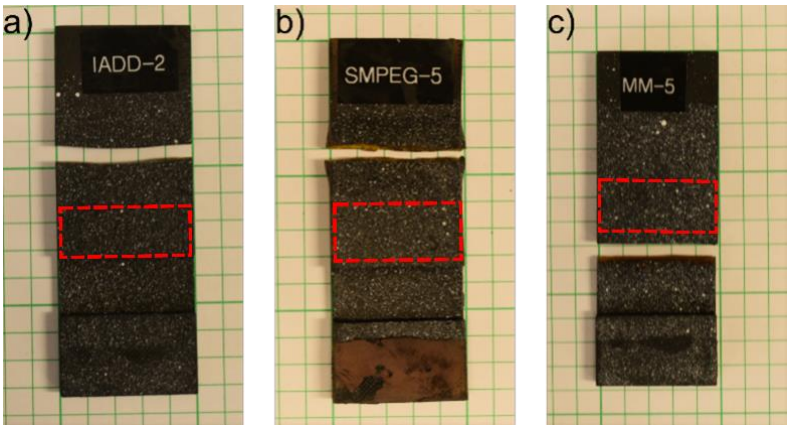

Figure 4-6: Characteristic sample failure; (a) IADD, (b) SPEG, and (c) MM. The overlap area has been highlighted in red.

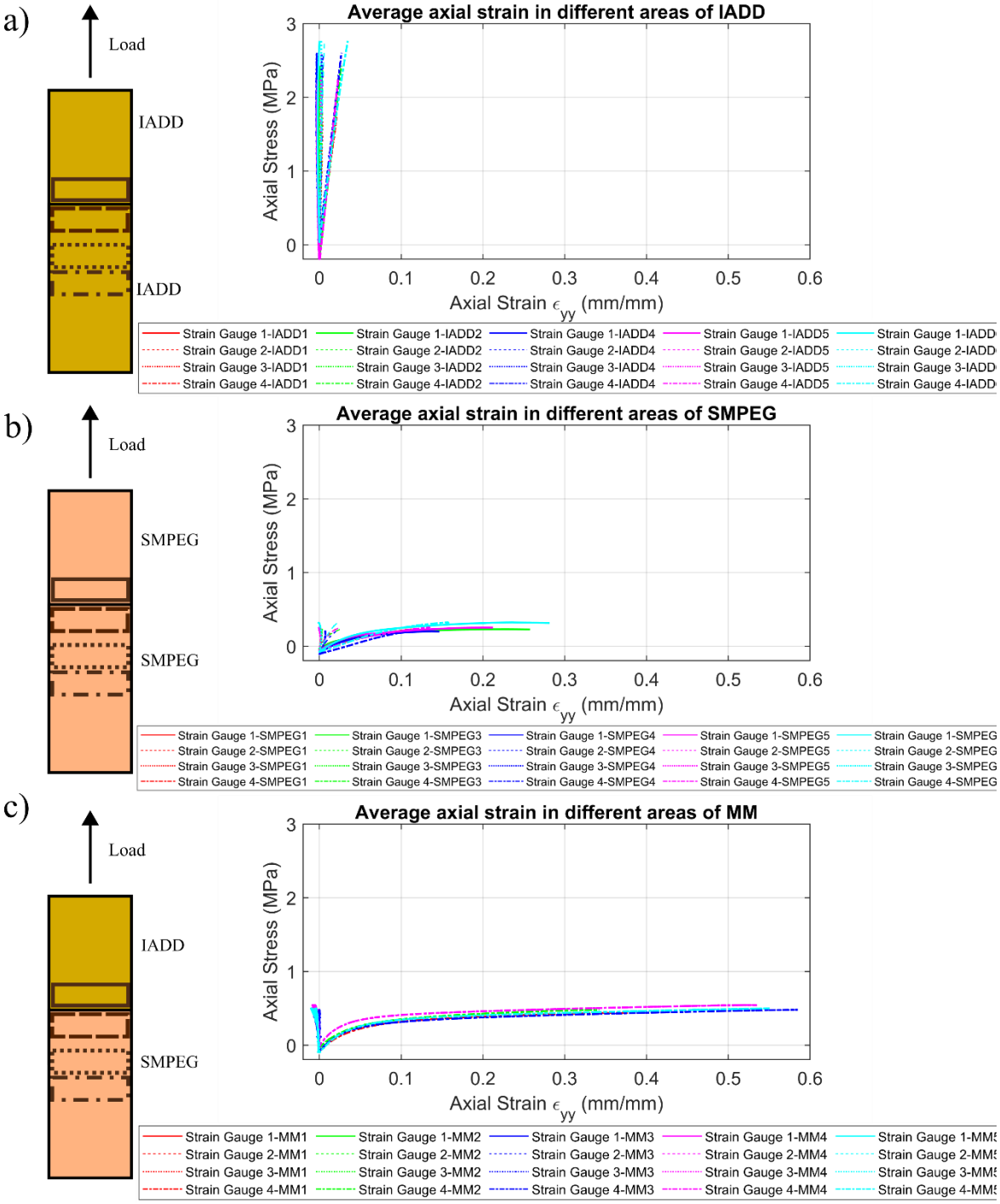

Figure 4-7: Stress vs average strain plots for the different samples in the different areas of the samples for all sample combinations: (a) IADD; (b) SPEG; (c) MM.

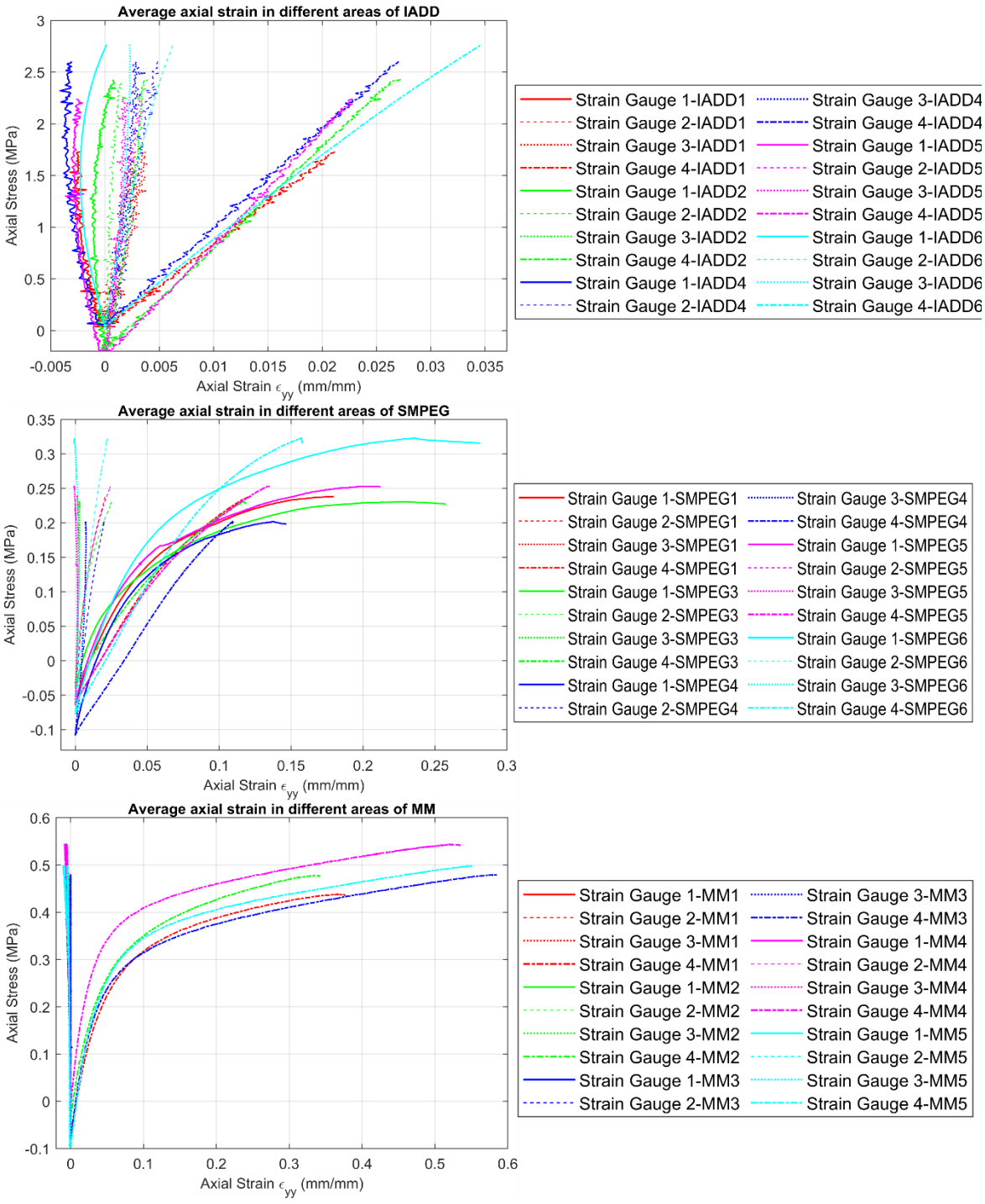

Figure 4-8: Zoomed in axial stress vs average axial strain plots for the different samples in the different areas of the samples; (a) IADD; (b) SPEG; (c) MM.

4.3.1.2.1 Vertical line plots

The average of the axial strain variation along the two vertical line plots on the front side of the samples, as seen in Figure 4-3(c). Figure 4-9 illustrates further support for validating the previous results. All the samples showed higher strains below the overlap region, which was also seen in Figure 4-5 and Figure 4-7. SPEG samples also show higher strains above the overlap region, which was also seen in Figure 4-5. The average axial strain of MM samples is found to be higher than 120% above the overlap region, demonstrating its high ductility.

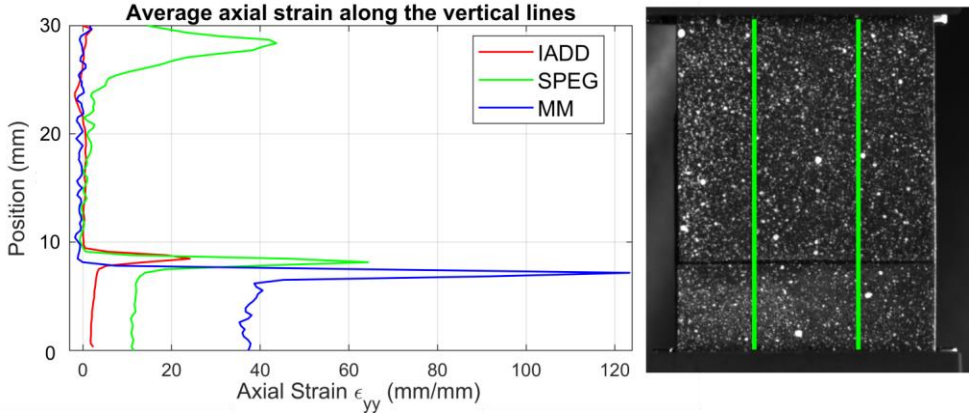

Figure 4-9: Average axial strain variation along the two vertical line plots on the front side of the samples.

4.3.1.3 Analysis of Shear strain with DIC

The shear strain distribution for all sample combinations is shown in Figure 4-10 at different loads ranging from 30 N to 900N. They were obtained from the images taken through the macro lens for the lateral sample view. It provides a better understanding of the mechanical behavior at the interface of the overlap region. The shear strains were markedly higher in SPEG and MM samples compared to IADD samples, as seen in Figure 4-10. The shear strains are more localized above and below the overlap region, and no noticeable shear strains were

observed along the lap joint interface. This indicates that there is less chance of weaker spots at the interface and the samples provide good adhesion.

The shear stress vs strain plots in Figure 4-11 and Figure 4-12 demonstrates the average shear strain in each of the strain gauges constructed on the overlap area of the lateral sample view, as shown in Figure 4-4(b). The shear strain in both the strain gauges is almost uniform in the IADD and SPEG samples due to their homogeneity. Shear strain in strain gauge 2 in the MM samples clearly reveals a higher shear strain than strain gauge 1, demonstrating the heterogeneity of the samples. Strain gauge 2 is placed on the overlap area, which consists of SPEG material, and since SPEG experiences much larger displacement due to its flexibility, the shear strain is also higher than strain gauge 1, which measures IADD material.

Figure 4-12 shows the shear stress vs strain with the axis scales changed to zoom in on to distinguish the strains in each individual strain gauge in all the samples. IADD and SPEG exhibit slightly higher strains in strain gauge 2 but are negligible. In the MM samples, shear strain in strain gauge 2 is markedly higher and reaches approximately 0.03% at 0.5 MPa shear stress, while strain gauge 1 records an average of 0.001 at 0.5 MPa. It can also be seen that the shear strains for all samples in each strain gauge in each combination are very close to each other, providing further evidence that the tests are repeatable and reproducible.

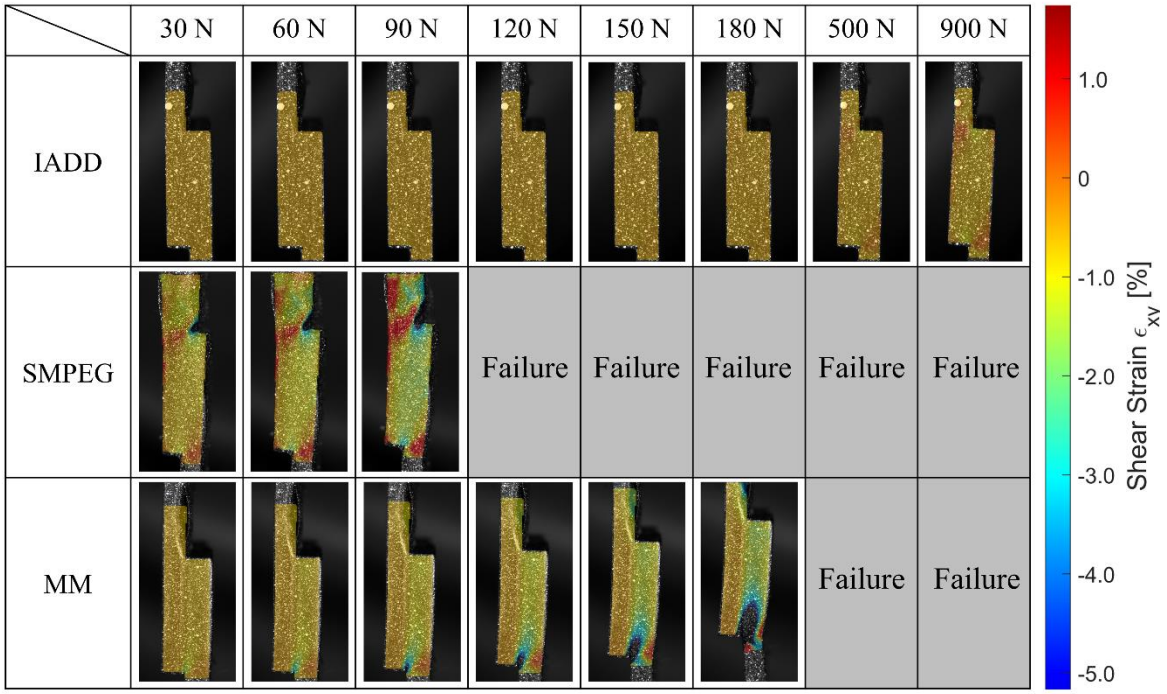

Figure 4-10: Shear strain maps of the lateral views of all three samples at different loads.

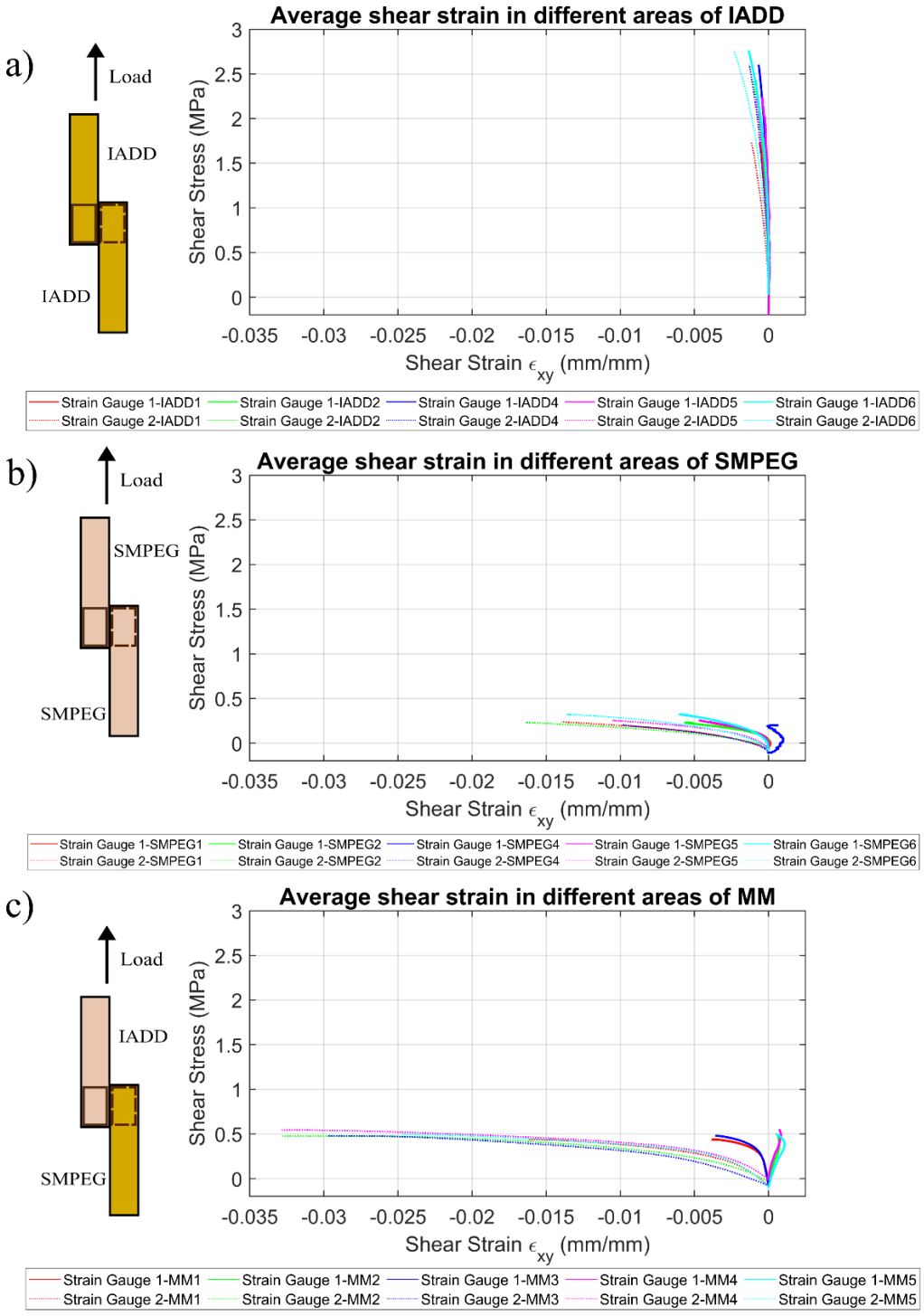

Figure 4-11: Stress vs average shear strain plots for all the samples in different areas of the samples for all sample combinations; (a) IADD; (b) SPEG; (c) MM.

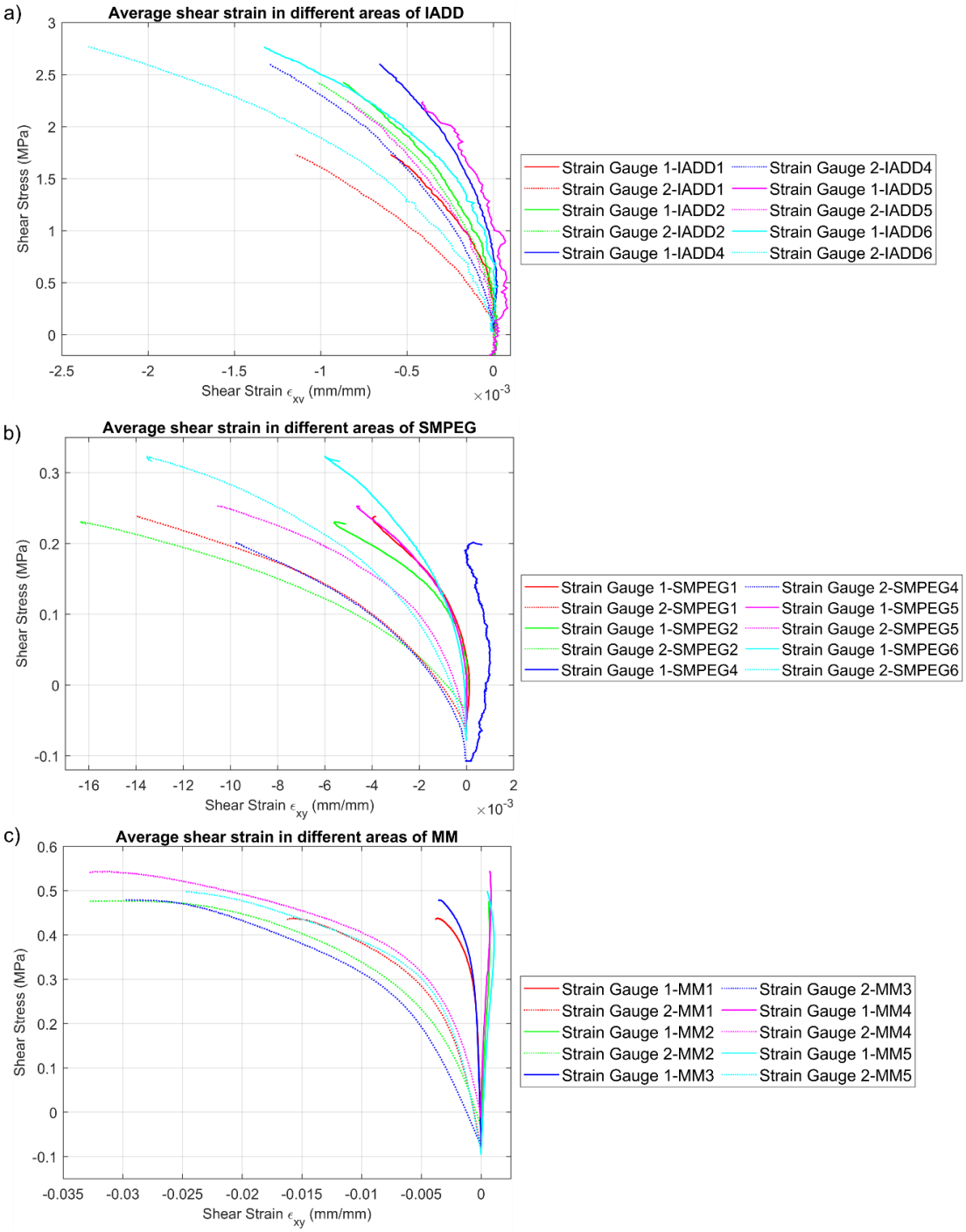

Figure 4-12: Zoomed-in shear stress vs average shear strain plots for all the samples in different areas of the samples for all the sample combinations: (a) PLA-PETG; (b) PLA-PETC; (c) PETG-PETC.

4.3.1.3.1 Horizontal line plots

Shear strains along the three horizontal line plots at three different positions of the overlap area in the lateral view, as illustrated in Figure 4-4(d) are shown in Figure 4-13. The shear strains in all three horizontal lines for IADD and SPEG are very similar. The shear strain along the horizontal line at the bottom of the overlap region (H1) in MM increases markedly from left to right. It reaches about 35% at the lap joint interface and increases to about 40% as the line enters the SPEG material part of the overlap region. It then decreases as the line moves further away from the joint interface. The large change in the shear strain at the lap joint interface can be attributed to material heterogeneity, as the SPEG part on the right side of the overlap region is displaced significantly more than the IADD material part of the lap joint, which is more rigid.

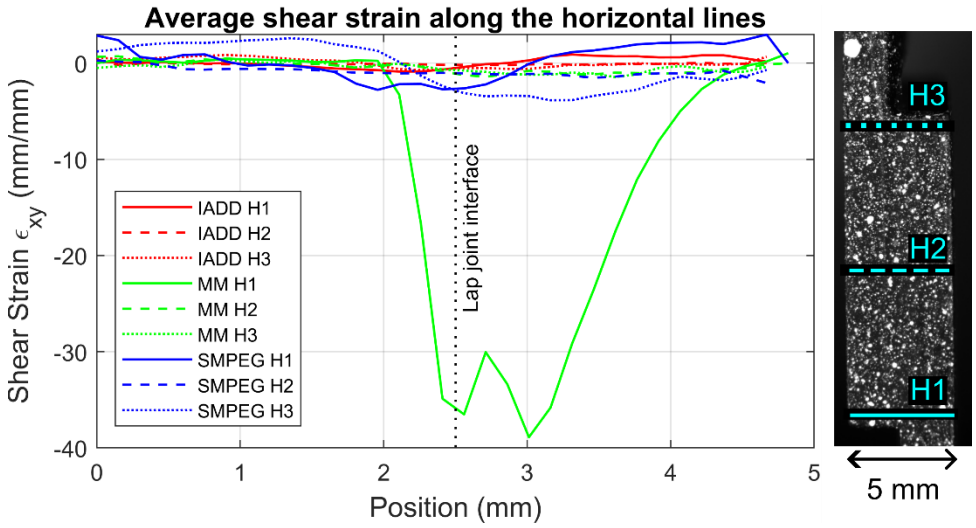

Figure 4-13: Shear strains along the three different horizontal line plots before failure on the overlap area (lateral side) for the three different material combinations.

4.3.2 Statistical analysis

The lap shear strength of the three different samples is listed in Table 4-5. IADD samples exhibit the highest strength among all the three sample combinations. The IADD samples exhibited 849.19% higher lap shear strength than the SPEG samples and 382.38% higher lap shear strength than the MM samples. The presence of IADD resin in the heterogeneous MM samples resulted in 96.78% higher lap shear strength compared to the homogenous SPEG samples, effectively doubling their strength.

One-way analysis of variance (ANOVA) was performed to find statistical differences between the different sample combinations, as listed in Table 4-6. The F statistic is very high (125.44), indicating that the variation between the group means is larger than the variation within the groups. The p-value (9.047×10^{-9}) is also much lower than 0.05, which means that the differences between the group means are statistically significant. So, the null hypothesis that all group means are equal must be rejected. Thus, there are significant differences in the lap shear strength between the groups.

Subsequently, a Tukey-Kramer post-hoc test was performed to determine the difference between the means of the different groups, and the resulting p-values are presented in Table 4-7. The p-values for the IADD-SPEG and IADD-MM pairs were lower than 0.05, indicating a significant difference between the sample combination pairs. For the SPEG and MM sample pairs, the p-value was 0.2648, which is higher than 0.05, indicating that there is no significant difference between the lap shear strength of SPEG and MM.

Table 4-5: Lap shear strength of all the sample combinations

Samples	Lap shear strength (MPa)
IADD	2.354 ± 0.39
SPEG	0.248 ± 0.04
MM	0.488 ± 0.04

Table 4-6: One way ANOVA analysis for the samples

Source	SS	df	MS	F	p-value (Prob>F)
Groups	13.2918	2	6.64592	125.44	p<0.001
Error	0.6358	12	0.05298	-	-
Total	13.9276	14	-	-	-

Table 4-7: Tukey-Kramer post-hoc analysis between all the sample types

Index	Sample 1	Sample 2	Lower Bound	Difference	Upper bound	p-value
1	IADD	SPEG	1.7176	2.1059	2.4943	p < 0.001
2	IADD	MM	1.4778	1.8662	2.2546	P<0.001
3	SPEG	MM	-0.6281	-0.2397	0.1486	0.2648

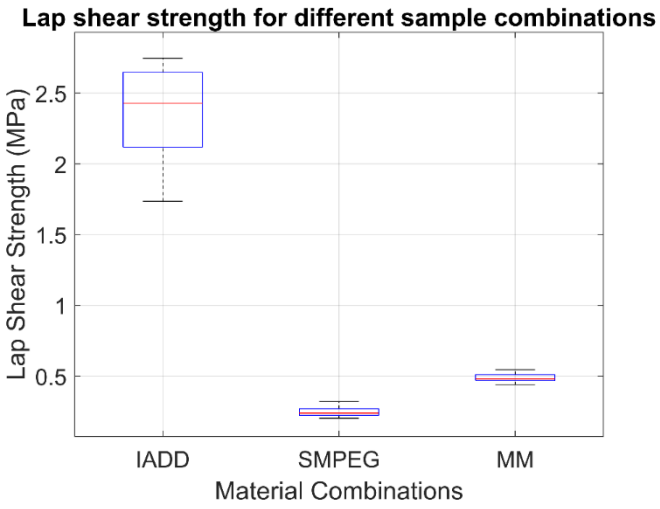

Figure 4-14: Box and whisker plot showing the lap shear strength of the different lap joint sample combinations.

4.4 Conclusion

Two different resins were formulated to fabricate a multi-material single-lap joint with DLP. They were compared to its homogenous base material lap joints using a standard lap shear test. 2D DIC was performed to evaluate the strain variations on the samples during the shear test.

The multi-material samples demonstrated improved mechanical properties compared to the soft material with an increase of 96.78% higher lap shear strength than SPEG samples, without any delamination at the overlap region. The multi-material samples exhibited the properties of both the hard and soft materials. It could withstand higher stresses before failure as well as stretch much more than the hard material, thus experiencing higher strains.

Full-field strain measurements with DIC also visualized the strain distributions on the samples from two directions, indicating the potential weak points. They also revealed a slight

bending movement in the multi-material samples due to the presence of materials with dissimilar mechanical properties.

The study demonstrates the feasibility of DLP multi-material printing, where functional multi-materials can be fabricated with high resolution and accuracy. Thus, materials with tunable mechanical properties can be printed to fabricate functional materials that may require mechanical properties that cannot be provided by conventional materials. These multi-materials can be widely used to fabricate chemically compatible microfluidic chips with soft membrane actuators and soft robotics.

Other standards such as ASTM D5379, ASTM D3528 [37] or Iosipescu shear test [38] maybe explored to further evaluate improvements in data accuracy and minimize unwanted movements in the samples.

4.5 Acknowledgements

S.P., Q.S., M.D.M., and B.E.R. acknowledge funding by the Deutsche Forschungsgemeinschaft (DFG, German Research Foundation) under Germany's Excellence Strategy – EXC 2193/1 – 390951807. The authors gratefully acknowledge the financial support from the Natural Sciences and Engineering Research Council of Canada RGPIN-2018-05899 and Mitacs - FR106568.

4.6 References

[1] X. Tian, L. Wu, D. Gu, S. Yuan, Y. Zhao, X. Li, L. Ouyang, B. Song, T. Gao, J. He, X. Lin, F. Lin, J. Zhu, D. Li, Roadmap for Additive Manufacturing: Toward

Intellectualization and Industrialization, Chinese Journal of Mechanical Engineering: Additive Manufacturing Frontiers 1 (2022) 100014. https://doi.org/10.1016/j.cjmeam.2022.100014.

[2] G. Prashar, H. Vasudev, A comprehensive review on sustainable cold spray additive manufacturing: State of the art, challenges and future challenges, Journal of Cleaner Production 310 (2021) 127606. https://doi.org/10.1016/j.jclepro.2021.127606.

[3] G. Manogharan, R. Wysk, O. Harrysson, R. Aman, AIMS – A Metal Additive-hybrid Manufacturing System: System Architecture and Attributes, Procedia Manufacturing 1 (2015) 273–286. https://doi.org/10.1016/j.promfg.2015.09.021.

[4] N. Poomathi, S. Singh, C. Prakash, A. Subramanian, R. Sahay, A. Cinappan, S. Ramakrishna, 3D printing in tissue engineering: a state of the art review of technologies and biomaterials, RPJ 26 (2020) 1313–1334. https://doi.org/10.1108/RPJ-08-2018-0217.

[5] S.C. Ligon, R. Liska, J. Stampfl, M. Gurr, R. Mülhaupt, Polymers for 3D Printing and Customized Additive Manufacturing, Chem. Rev. 117 (2017) 10212–10290. https://doi.org/10.1021/acs.chemrev.7b00074.

[6] S. Yin, A.J. Jacobsen, L. Wu, S.R. Nutt, Inertial stabilization of flexible polymer micro-lattice materials, J Mater Sci 48 (2013) 6558–6566. https://doi.org/10.1007/s10853-013-7452-0.

[7] J. Brennan-Craddock, D. Brackett, R. Wildman, R. Hague, The design of impact absorbing structures for additive manufacture, J. Phys.: Conf. Ser. 382 (2012) 012042. https://doi.org/10.1088/1742-6596/382/1/012042.

[8] C. Schwaar, NFL's Safest Helmets Absorb Impact With 3D Printing Instead Of Foam, (2023). https://www.forbes.com/sites/carolynschwaar/2023/10/01/nfls-safest-helmets-absorb-impact-with-3d-printing-instead-of-foam/ (accessed August 19, 2024).

[9] Additive Manufacturing Market Size Report, 2030, (n.d.).

[10] Landmark Technologies | GE Aerospace, (n.d.). https://www.geaerospace.com/sustainability/innovation/landmark-technologies (accessed August 18, 2024).

[11] A. Jafari, S. Vahid Niknezhad, M. Kaviani, W. Saleh, N. Wong, P.P. Van Vliet, C. Moraes, A. Ajji, L. Kadem, N. Azarpira, G. Andelfinger, H. Savoji, Formulation and Evaluation of PVA/Gelatin/Carrageenan Inks for 3D Printing and Development of Tissue-Engineered Heart Valves, Adv Funct Materials (2023) 2305188. https://doi.org/10.1002/adfm.202305188.

[12] R. Torres, P. Snoeij, D. Geudtner, D. Bibby, M. Davidson, E. Attema, P. Potin, B. Rommen, N. Floury, M. Brown, I.N. Traver, P. Deghaye, B. Duesmann, B. Rosich, N. Miranda, C. Bruno, M. L'Abbate, R. Croci, A. Pietropaolo, M. Huchler, F. Rostan, GMES Sentinel-1 mission, Remote Sensing of Environment 120 (2012) 9–24. https://doi.org/10.1016/j.rse.2011.05.028.

[13] M.A. Skylar-Scott, J. Mueller, C.W. Visser, J.A. Lewis, Voxelated soft matter via multimaterial multinozzle 3D printing, Nature 575 (2019) 330–335. https://doi.org/10.1038/s41586-019-1736-8.

[14] J.O. Hardin, T.J. Ober, A.D. Valentine, J.A. Lewis, Microfluidic Printheads for Multimaterial 3D Printing of Viscoelastic Inks, Advanced Materials 27 (2015) 3279–3284. https://doi.org/10.1002/adma.201500222.

[15] S. Zheng, M. Zlatin, P.R. Selvaganapathy, M.A. Brook, Multiple modulus silicone elastomers using 3D extrusion printing of low viscosity inks, Additive Manufacturing 24 (2018) 86–92. https://doi.org/10.1016/j.addma.2018.09.011.

[16] L.R. Lopes, A.F. Silva, O.S. Carneiro, Multi-material 3D printing: The relevance of materials affinity on the boundary interface performance, Addit Manuf 23 (2018) 45–52. https://doi.org/10.1016/j.addma.2018.06.027.

[17] M. Ribeiro, O. Sousa Carneiro, A. Ferreira Da Silva, Interface geometries in 3D multi-material prints by fused filament fabrication, Rapid Prototyp J 25 (2019) 38–46. https://doi.org/10.1108/RPJ-05-2017-0107.

[18] K.L. Sampson, B. Deore, A. Go, M.A. Nayak, A. Orth, M. Gallerneault, P.R.L. Malenfant, C. Paquet, Multimaterial Vat Polymerization Additive Manufacturing, ACS Appl. Polym. Mater. 3 (2021) 4304–4324. https://doi.org/10.1021/acsapm.1c00262.

[19] M. Regehly, Y. Garmshausen, M. Reuter, N.F. König, E. Israel, D.P. Kelly, C.-Y. Chou, K. Koch, B. Asfari, S. Hecht, Xolography for linear volumetric 3D printing, Nature 588 (2020) 620–624. https://doi.org/10.1038/s41586-020-3029-7.

[20] A. Andreu, P.-C. Su, J.-H. Kim, C.S. Ng, S. Kim, I. Kim, J. Lee, J. Noh, A.S. Subramanian, Y.-J. Yoon, 4D printing materials for vat photopolymerization, Additive Manufacturing 44 (2021) 102024. https://doi.org/10.1016/j.addma.2021.102024.

[21] D.K. Patel, A.H. Sakhaei, M. Layani, B. Zhang, Q. Ge, S. Magdassi, Highly Stretchable and UV Curable Elastomers for Digital Light Processing Based 3D Printing, Advanced Materials 29 (2017) 1606000. https://doi.org/10.1002/adma.201606000.

[22] S. Schüller-Ravoo, J. Feijen, D.W. Grijpma, Preparation of Flexible and Elastic Poly(trimethylene carbonate) Structures by Stereolithography, Macromolecular Bioscience 11 (2011) 1662–1671. https://doi.org/10.1002/mabi.201100203.

[23] Q. Song, Y. Chen, P. Hou, P. Zhu, D. Helmer, F. Kotz-Helmer, B.E. Rapp, Fabrication of Multi-Material Pneumatic Actuators and Microactuators Using Stereolithography, Micromachines 14 (2023) 244. https://doi.org/10.3390/mi14020244.

[24] E. Brancewicz-Steinmetz, R.D.V. Vergara, V.H. Buzalski, J. Sawicki, Study of the adhesion between TPU and PLA in multi-material 3D printing, Journal of Achievements in Materials and Manufacturing Engineering 115 (2022) 49–56. https://doi.org/10.5604/01.3001.0016.2672.

[25] E. Brancewicz-Steinmetz, J. Sawicki, P. Byczkowska, The Influence of 3D Printing Parameters on Adhesion between Polylactic Acid (PLA) and Thermoplastic Polyurethane (TPU), Materials 14 (2021) 6464. https://doi.org/10.3390/ma14216464.

[26] J. Mueller, D. Courty, M. Spielhofer, R. Spolenak, K. Shea, Mechanical Properties of Interfaces in Inkjet 3D Printed Single- and Multi-Material Parts, 3D Printing and Additive Manufacturing 4 (2017) 193–199. https://doi.org/10.1089/3dp.2017.0038.

[27] F. Awaja, M. Gilbert, G. Kelly, B. Fox, P.J. Pigram, Adhesion of polymers, Progress in Polymer Science 34 (2009) 948–968. https://doi.org/10.1016/j.progpolymsci.2009.04.007.

[28] F. Lagier, X. Jourdain, C.D. Sa, F. Benboudjema, J.B. Colliat, Numerical strategies for prediction of drying cracks in heterogeneous materials: Comparison upon experimental results., Eng. Struct. 33 (2011) 920–931. https://doi.org/10.1016/j.engstruct.2010.12.013.

[29] M.D. Mylo, S. Poppinga, Digital image correlation techniques for motion analysis and biomechanical characterization of plants., Front. Plant Sci. 14 (2024). https://doi.org/10.3389/fpls.2023.1335445.

[30] H. Schreier, J.-J. Orteu, M.A. Sutton, Image Correlation for Shape, Motion and Deformation Measurements: Basic Concepts,Theory and Applications, Springer US, Boston, MA, 2009. https://doi.org/10.1007/978-0-387-78747-3.

[31] C. Unlusoy, G.W. Melenka, Flexural testing of cellulose fiber braided composites using three dimensional digital image correlation, Compos. Struct 230 (2019) 111538. https://doi.org/10.1016/j.compstruct.2019.111538.

[32] J. Qiu, M.K. Idris, G. Grau, G.W. Melenka, Fabrication of electroluminescent carbon fiber composite for damage visualization, Manuf. Lett 24 (2020) 56–60. https://doi.org/10.1016/j.mfglet.2020.03.010.

[33] G.W. Melenka, C. Ayranci, Advanced measurement techniques for braided composite structures: A review of current and upcoming trends, Journal of Composite Materials 54 (2020) 3895–3917. https://doi.org/10.1177/0021998320903105.

[34] M. Jerabek, Z. Major, R.W. Lang, Strain determination of polymeric materials using digital image correlation, Polymer Testing 29 (2010) 407–416. https://doi.org/10.1016/j.polymertesting.2010.01.005.

[35] Test Method for Lap Shear Adhesion for Fiber Reinforced Plastic (FRP) Bonding, (n.d.). https://doi.org/10.1520/D5868-01R23.

[36] E. Jones, M. Iadicola, R. Bigger, B. Blaysat, C. Boo, M. Grewer, J. Hu, A. Jones, M. Klein, K. Raghavan, P. Reu, T. Schmidt, T. Siebert, M. Simenson, D. Turner, A. Vieira, T. Weikert, A Good Practices Guide for Digital Image Correlation, 1st ed., International Digital Image Correlation Society, 2018. https://doi.org/10.32720/idics/gpg.ed1.

[37] Standard test method for strength properties of double lap shear adhesive joints by tension loading, (2002).

[38] D.F. Adams, The Iosipescu shear test method as used for testing polymers and composite materials, Polymer Composites 11 (1990) 286–290. https://doi.org/10.1002/pc.750110506.

Chapter 5 Conclusions, Recommendations and Future Work

5.1 Conclusions

This thesis analyzed the interfaces of 3D-printed multi-material samples at the joint boundary under shear testing using 2D DIC. An introduction to the fundamental topics relevant to these studies is provided at the beginning of this thesis. 3D printing has evolved significantly, advancing from prototyping technology to a method for manufacturing multi-material functional parts. These parts offer several advantages, including enhanced mechanical, thermal, and optical performance, with properties that can be specifically tailored. However, MM3DP samples experience non-uniform deformations due to material heterogeneity and anisotropy. As research into MM3DP samples is still in its early stages, many gaps in the current research need to be explored.

The first study, presented in Chapter 3, evaluates the interface characteristics of FFF-printed multi-material single-lap joints. Three different filaments—PLA, PETG, and PETC (PETG with 20 % short carbon fibers)—were used to manufacture six different multi-material single-lap joints in every possible combination. The PETC filament was analyzed with TGA to investigate the carbon fiber content in the filament, which significantly influences the mechanical properties of 3D-printed multi-material parts. 2D DIC was used to analyze the full-field strain variation on the lap joint interface, with two different CMOS cameras set at 90° to each other, capturing both the front and lateral views of the samples. The lap shear strength of the multi-material heterogeneous samples was compared with the homogenous samples made of a single material. Digital strain gauges were used during post-processing to evaluate the average axial and shear strains in different

regions of the samples, highlighting the localized strain concentrations. A horizontal line plot was created on the image of the lateral view at the bottom edge of the overlap region to investigate shear strain along that line on the samples before failure. Failure modes were observed and classified according to ASTM D5573, ASTM standard for classifying failure modes in FRP joints. The samples were sectioned to observe the joint interface under a microscope at different magnifications. Finally, statistical analysis was performed to identify significant differences among sample combinations.

The TGA results showed that the PETC filament had an average carbon fiber content of 19.051% by weight, close to the manufacturer's specifications of 20%. Previous studies on FFF multi-material 3D printing indicated that multi-material samples were significantly weaker than homogenous samples. In this study, the shear test demonstrated that the lap shear strength of the multi-material PLA-PETG (0.605 MPa) and PLA-PETC (0.771 MPa) samples was significantly weaker than its homogenous base material samples – PLA -PLA (2.923 MPa), PETG-PETG (1.849 MPa), and PETC-PETC (2.201 MPa). However, the lap shear strength of multi-material PETG-PETC (2.701 MPa) samples was comparable to the homogenous PETG and PETC lap joints. Adhesive failure was observed in the multi-material PLA-PETG and PLA-PETC samples, where the lap joints delaminated at the joint interface. This exhibits weakness at the lap joint interface for those multi-material samples. In contrast, the multi-material PETG-PETC samples experienced stock break failure similar to the homogeneous samples.

The strain maps in DIC showed that the shear strain concentrations were highest below the overlap region for all the homogenous samples and multi-material PETG-PETC samples, suggesting lower chances of failure in the overlap region. For the multi-material PLA-PETG and PLA-PETC samples, the shear strain concentrations were higher at the lap joint interface. The horizontal line

plot also demonstrates higher shear strains in the last frame before failure for the PLA-PETG and PLA-PETC samples than the remaining samples at the lap joint interface, which is also where these samples delaminate during failure. The digital strain gauges showed that the average axial and shear strains for the homogeneous samples and multi-material PETG-PETC samples exhibited similar patterns, whereas the weaker PLA-PETG and PLA-PETC samples showed different patterns, demonstrating the similarity between multi-material PETG-PETC and homogeneous samples.

Samples containing PETC material exhibited higher lap shear strength compared to those with PETG material, attributed to the presence of carbon fibers at the interface. One-way ANOVA followed by Tukey-Kramer analysis was performed for detailed statistical analysis. The p-value was analyzed for all 15 pairs of sample combinations. If the p-value was higher than 0.05, there was no evidence to reject the null hypothesis, indicating no significant statistical difference at the 5% significance level. The multi-material PETG-PETC sample and the homogeneous PLA and PETC samples had p-values higher than 0.05, suggesting no significant statistical difference. The multi-material PLA-PETG and PLA-PETC samples also had p-values higher than 0.05, indicating similar weakness. Thus, statistical analysis supported that the multi-material PETG-PETC samples had similar mechanical performance to the stronger homogeneous samples.

This study demonstrated that infusing fibers in one part of the sample while maintaining the same base material without fibers in the other part provides the best mechanical performance among the multi-material samples. The mechanical performance of these multi-material samples was comparable to, and in some cases, better than, the homogeneous base material samples. The results also show the heterogeneity of the samples, where each part of the samples. The individual

materials also retain their mechanical properties in the multi-material samples and thus the multi-material exhibits both the properties of the base materials.

In the second study, multi-material single-lap joints were fabricated using the Digital Light Processing (DLP) printing method and compared to homogeneous base material samples produced by the same method using shear testing. Two different resins were formulated to produce rigid and flexible samples, both of which were used for the multi-material lap joints. DIC was used to evaluate strain variations on the front and lateral sides of the samples. Statistical analysis was also performed to identify significant differences between the sample combinations.

The results showed that the homogeneous harder (IADD) samples had the highest lap shear strength. However, the multi-material (MM) samples had 96.78% higher lap shear strength than the soft resin (SPEG) samples. DIC results indicated that localized strain concentrations were higher outside the overlap region, consistent with the observed failure in the samples. All sample combinations experienced stock break failure, demonstrating good adhesion at the lap joint interface. Axial and shear strains were much higher in the SPEG parts of the samples due to their high flexibility.

Further statistical analysis supported these findings. The Tukey-Kramer analysis after one-way ANOVA indicated that the p-value was only higher than 0.05 for the lap shear strength of SPEG and MM samples, showing no significant statistical difference at the 5% significance level. The lap shear strength of IADD samples exhibited significant statistical differences compared to the SPEG and MM samples, as evident from the box and whisker plot.

In summary, this thesis includes two studies utilizing distinct 3D printing techniques. The first study employed the FFF technique, which can alter the macrostructure at the joint interface with

fillers to enhance adhesion. The second study utilized the DLP method, which alters the microstructure at the joint interface to improve adhesion. Both methods successfully produced multi-material samples that exhibited strong adhesion at the lap joint interface without delamination. A comprehensive analysis was conducted on the strain behavior, failure modes and lap shear strength of all the samples. A methodology was developed for 2D DIC to thoroughly investigate both axial and shear strains in the samples. The DIC results highlight the heterogeneity of the multi-material 3D printed samples with minimal error as it does not exert any additional load on the samples or remain in contact with them. Moreover, the strain variations can be analyzed at discrete locations on the samples at different loads. Additionally, statistical analysis was also performed to further substantiate the findings.

5.2 Recommendations

The methodology utilized in this thesis has yielded detailed results regarding the interface characteristics of multi-material 3D-printed samples. To ensure the accuracy and repeatability of the results, recommendations are provided in two key areas: sample preparation and DIC analysis. These recommendations aim to enhance the reliability and precision of future studies.

Optimum printing parameters should be explored for the specific filaments that are being used to fabricate the samples. Higher temperatures during FFF printing may cause excess material deposition at the interface when printing with the second material, leading to manufacturing defects. A hardened steel nozzle should be used instead of a brass nozzle for FFF printers when using abrasive filaments, especially filaments containing fibers. Brass nozzles wear out quickly, potentially affecting part dimensions' accuracy. Additionally, the humidity in the room with the printer should be monitored to reduce the chances of print failure. During multi-material FFF

printing, the swipe element should also be maintained to avoid contamination in the new material layer at the interface.

For DLP printing, resins should be maintained at specific temperatures when the vats are idle outside the printer, as cold temperatures can increase viscosity, making the resin unsuitable for printing. Resins should also be stored in a dark area to avoid curing. Solvents used to wash resin from DLP samples should be tested before use, as significant swelling was observed in SPEG samples washed with ethanol.

Proper setup of the DIC equipment is crucial before capturing images during mechanical testing. A suitable camera and lens should be selected so that the sample covers at least one-third of the field of view. Speckling on the sample should match the field of view with appropriate speckle size and density, ensuring high contrast under proper lighting conditions while avoiding reflections. During DIC processing, the fit error of the reference should not exceed 0.7 for better accuracy. The correlation subset window size and step size should be chosen so that each subset window contains a minimum of 4-5 speckles. Properly setting these parameters is essential to ensure low errors in the DIC results.

5.3 Future Work

The use of 2D DIC in this thesis highlights its effectiveness for analyzing non-uniform deformations in heterogeneous structures. This methodology can be applied to explore various material combinations that may offer better mechanical performance. Investigating different thermoplastic filaments containing various fibers can lead to the fabrication of superior multi-material 3D-printed parts. Additionally, varying the fiber weight percentages in the filaments can help determine the optimal fiber content for higher mechanical performance. Functionally graded

materials could also be 3D-printed and compared to different multi-material parts to further characterize multi-material interfaces.

Due to the slight bending observed in the samples caused by high material heterogeneity, alternative standard tests such as Iosipescu and ASTM 5379 could be used for shear testing to minimize unwanted movements. The standard test method for double lap shear adhesive joints by tension loading (ASTM D 3528-96) could also be considered, as the double lap design helps minimize bending in the samples by providing support on both sides of the overlap region. An analytical model based on the mechanics of materials could be developed and validated with experimental data from DIC. As more material combinations are explored, these analytical models can be modified to fit additional experimental results. This approach can later be utilized to model complex 3D-printed multi-materials, expediting the design process and reducing costs.